NASA Technical Memorandum 78235

Space Processing Applications Rocket Project SPAR IV - Engineering Report (Final)

JANUARY 1980

NASA

NASA Technical Memorandum 78235

Space Processing Applications Rocket Project SPAR IV - Engineering Report (Final)

Compiled by Fred Reeves
George C. Marshall Space Flight Center
Marshall Space Flight Center, Alabama

National Aeronautics
and Space Administration

Scientific and Technical Information Office

1980

TABLE OF CONTENTS

CHAPTER I

SPACE PROCESSING APPLICATION ROCKET PROJECT

SPAR IV

ENGINEERING REPORT

W. Harold Johnson
Payload Integrator

Nov. 15, 1977
Date

TABLE OF CONTENTS

LIST OF FIGURES

LIST OF TABLES

1.0 Summary

The SPAR IV Black Brant VC rocket lifted off the launch pad at WSMR,Tuesday, June 21, 1977, at 1600:00:03 G.m.t. (10:00 a.m., md.t.). The launch was successful, and the payload was recovered intact.

Payload power was applied to all experiments as planned, and all experiments operated within the predicted near zero gravity. All external flight support requirements to each experiment were met as indicated by the reduced flight data, although power to the payload experiments was not removed at T+660 seconds as programmed. Also, none of the experiments operated precisely as planned. Discussion of those experimental anomalies may be found in paragraph 5 below and in the Principal Investigator's reports attached.

2.0 SPAR IV Payload Configuration

The SPAR IV payload consisted of four experiments, the improved support module, and the measurement module. The experiments are listed below:

74-15 Uniform Dispersions of Crystallization Processing
74-37 Contained Polycrystalline Solidification in Low-G
74-49 Containerless Processing of Ferromagnetic Materials
76-20 Containerless Processing Technology

The orientation of the experiments in the SPAR IV rocket is shown in Figure 1.

3.0 Rocket Performance

3.1 Flight Sequence

The SPAR IV flight profile is shown in Figure 2. The predicted and actual sequence of events are shown as a function of flight time.

3.2 Low Gravity

The predicted low-g (10^{-4} or less) time was based upon an all-up payload weight of 844.7 pounds. The science payload (MSFC furnished) weighed 541 pounds.

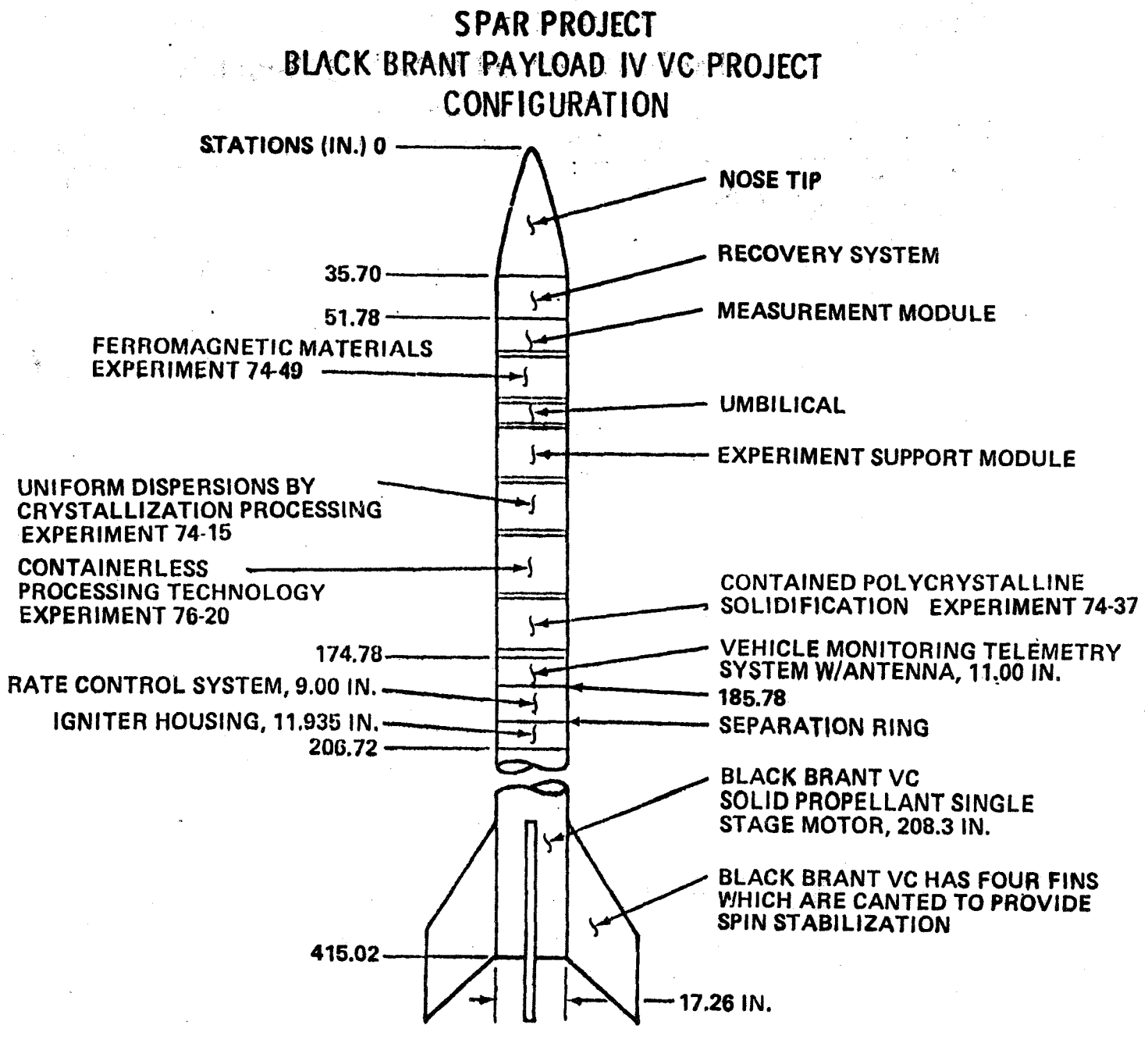

FIGURE 1. LAUNCH VEHICLE AND PAYLOAD CONFIGURATION

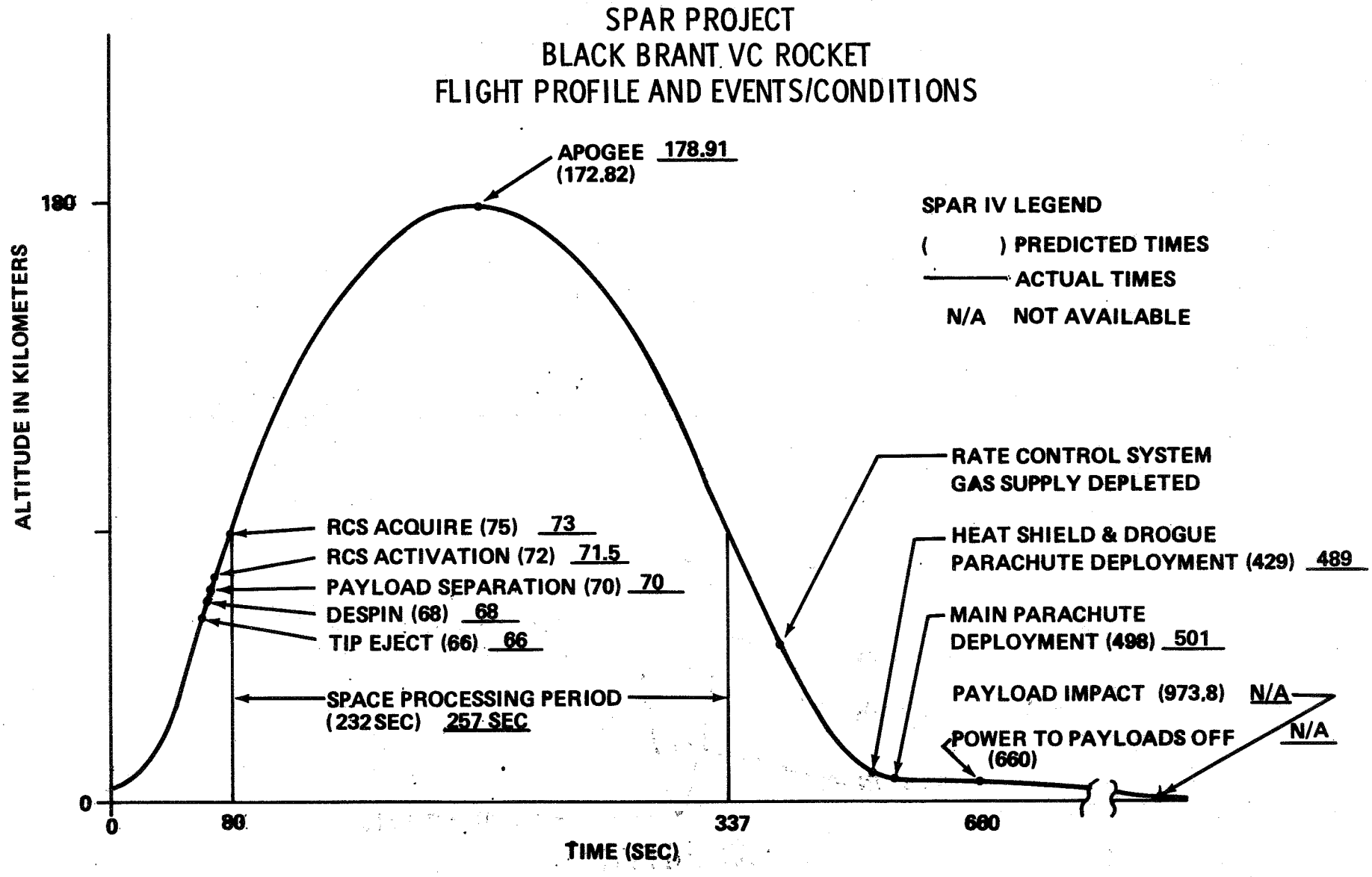

FIGURE 2. FLIGHT PROFILE AND EVENTS

The measurement module accelerometer measurements indicated that the low-g period on all three axes began at T+80 seconds and ended at T+337 seconds--giving a low-g period of 257 seconds. Minimum low-g period required by experiments was 240 seconds.

Because of the preflight analysis and the 3 sigma low-g prediction, experiment 76-20 low-g operation was set to begin no earlier than T+100 seconds.

4.0 Payload Support Operations

4.1 Payload Sequence of Events

Experiments 74-15 and 74-37 required preheat prior to launch that was supplied by ground power. At T-0, a liftoff signal was given to each experiment. Each experiment provided its own timer for control of events during the flight. The events are shown in Figure 3.

The actual timelines were well within the acceptable limits of each experiment. Experiment 76-20 had one event which did not occur because of internal electronic problems. The planned power removal to experiments at T+660 seconds did not occur. See paragraph 8.0 for discussion of this anomaly.

4.2 Payload Power

The support module supplied battery power to all experiments except experiment 74-49. This experiment provided its own battery for experiment operation.

Transfer of electrical power from ground support equipment to flight batteries was accomplished at T-3 minutes. At liftoff, power was applied to each experiment as designed. The Science Payload Battery (SPB) current was stable throughout the flight. At approximately 65 seconds, the current demand went up to 22 amps when experiment operations began. The current stabilized at 20 amps throughout the experiment operating time, then dropped to approximately 12 amps, and stabilized at 15 amps. The battery operated well within the current range required. Maximum peak current load expected was 30 amps.

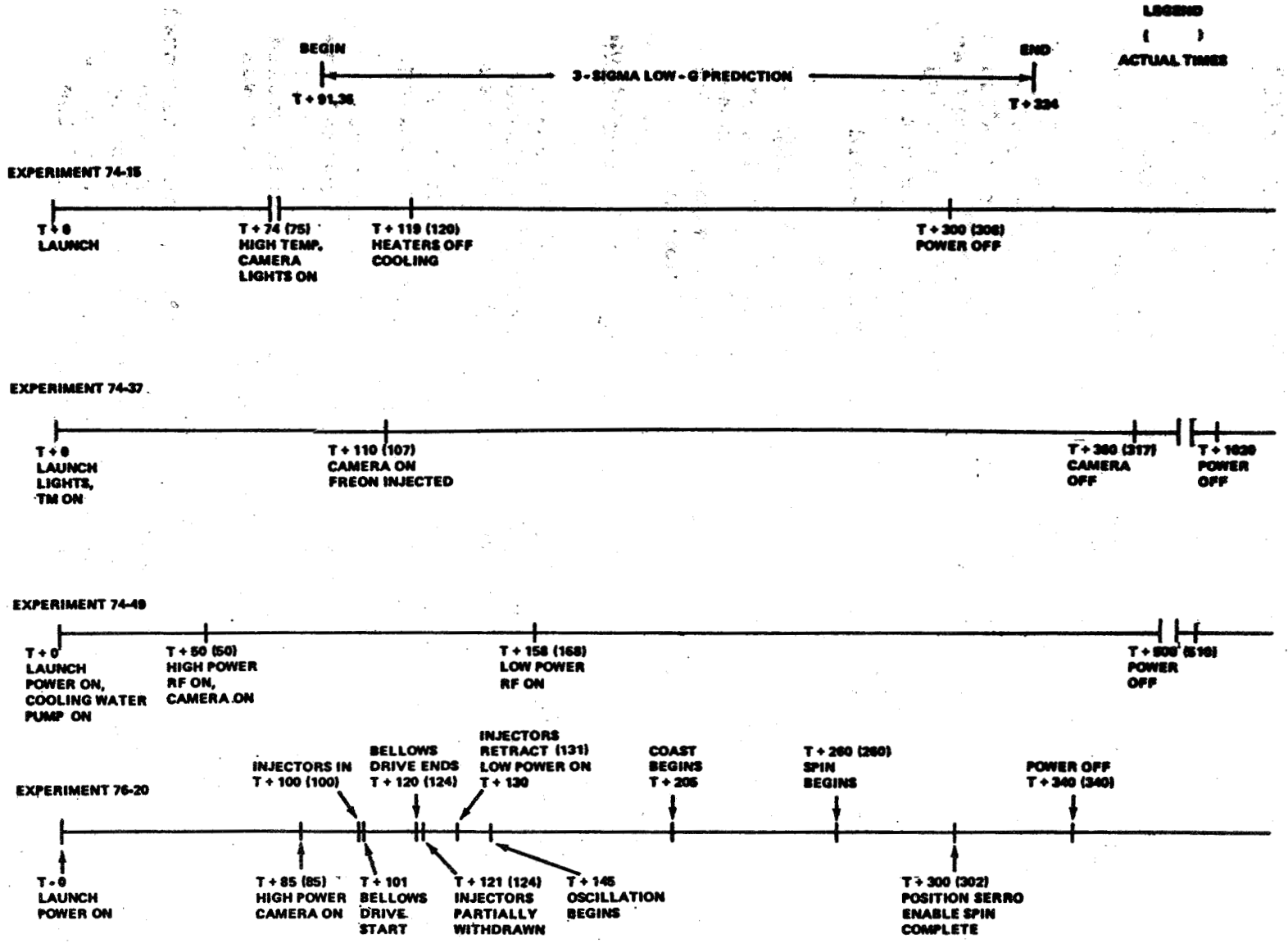

FIGURE 3. SPAR IV PAYLOAD EXPERIMENT TIMELINE

5.0 Experiment Operations

5.1 Experiment 74-15, Uniform Dispersions of Crystallization Processing

The experiment consisted of investigating interaction between second phase particles and an advancing crystal-liquid interface. The flight operation first applied heat to the specimens, then cooling was allowed while photographs were being taken. See Figure 3 for flight sequence timeline.

The flight data indicated heating began at T+74 seconds at which time camera operation also began. Heaters were turned off at T+119 seconds and cooling began. The temperatures began to decrease at T+140 seconds for most cells. Cell No. 1 temperature range is plotted in Figure 4, indicating a typical cooling rate and gradient, as planned. The power (plus 15 volts d.c.) was removed from the experiment at 308 seconds into the flight to ensure that the heaters were off and that freezing would occur during low-g condition.

After postflight inspection of the cell samples, the PI indicated that the specimens were fluid after landing and that heat had been reapplied to the cells after the flight was completed. This was probably caused by the failure of the K1 (100 amp) relay to reset, as discussed in paragraph 8.0 below.

5.2 Experiment 74-37, Contained Polycrystalline Solidification in Low-G

This experiment objective was to determine if a low-g condition affects the transition which occurs between equiaxed and columnar grain structure in metallic castings. The samples required 45 minutes of preheat prior to launch. This was accomplished by GSE power. At approximately 110 seconds into the flight, Freon was injected into the sample area for cooling.

The data show cooling occurred very slowly indicating that the Freon did not flow sufficiently to allow the crystalline structure to form as planned. The temperature in the center of the specimen is shown in Figure 5. The specimens had only cooled 13°C when the camera ran out of film at T+317 seconds. This was due to blockage in the Freon flow control valve.

A problem with the Freon flow occurred during the horizontal test prior to launch. The flowrate was increased by the PI to achieve proper cooling. For resolution of the cooling problem in later flights, grease was eliminated from the Freon system, a filter was installed downstream from the control point and the needle valve was replaced with an orifice.

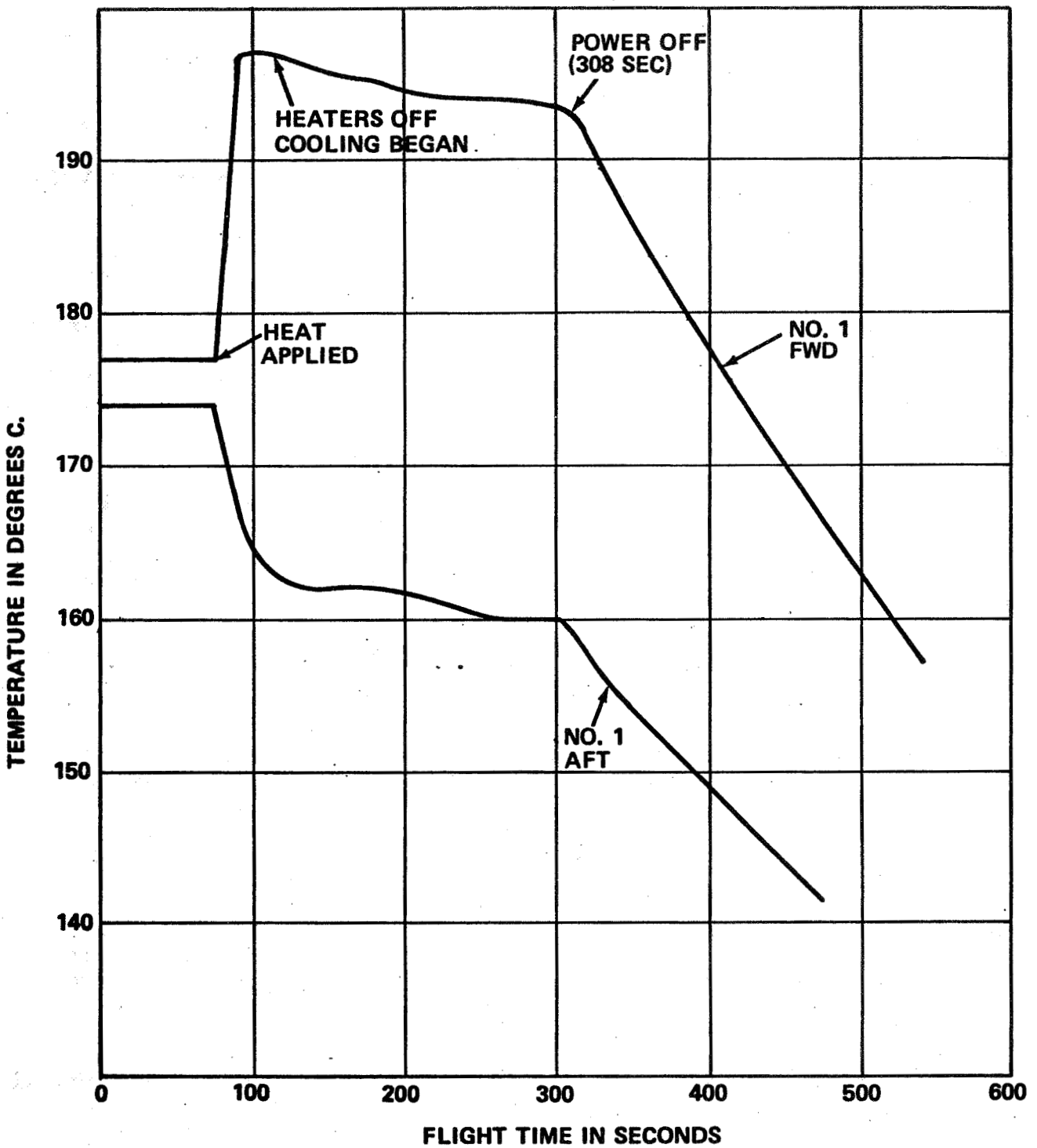

FIGURE 4. EXPERIMENT 74-15 – CELL NO. 1 FWD AND AFT TEMPERATURES

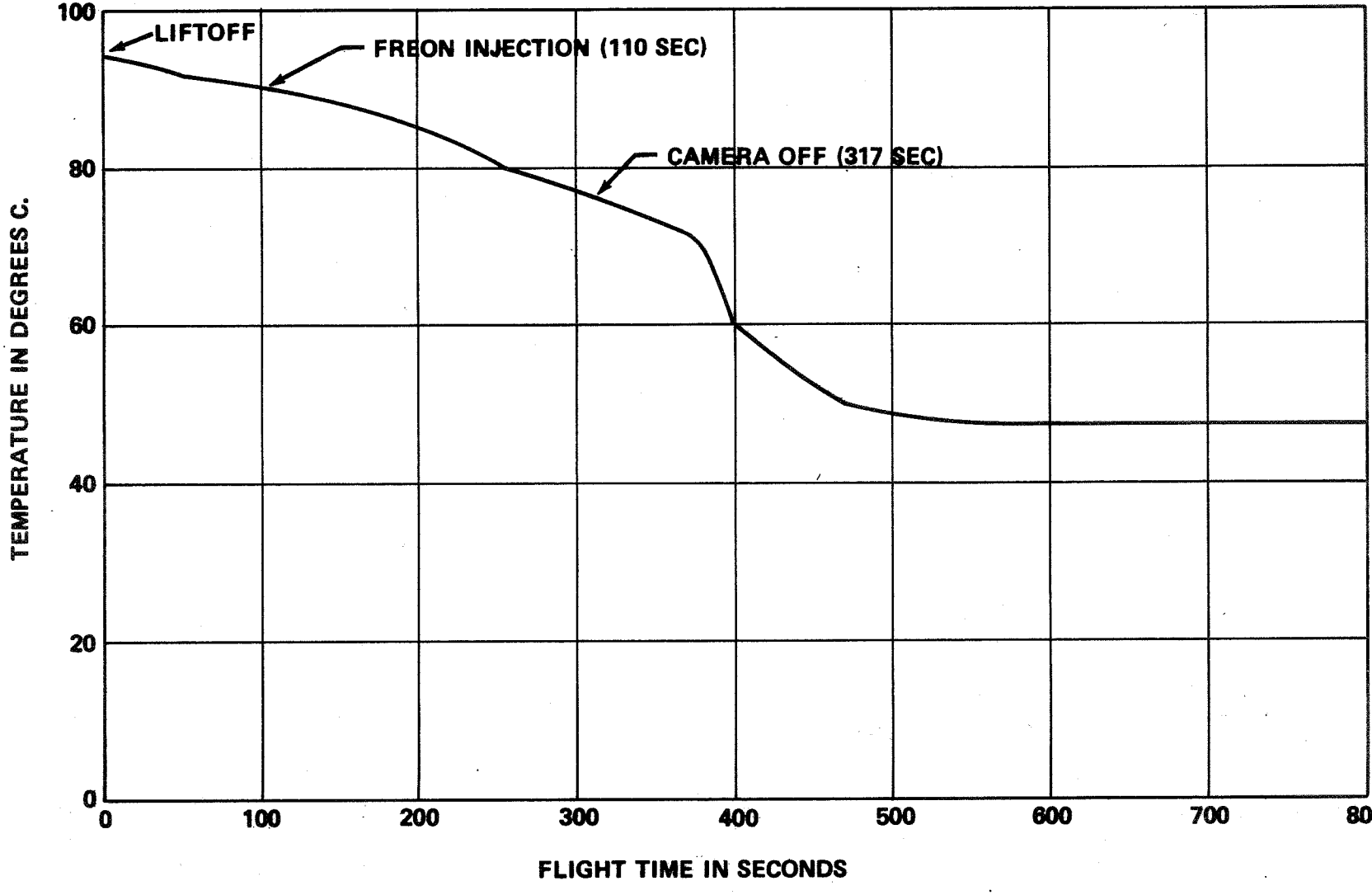

FIGURE 5. EXPERIMENT 74-37 - TEMPERATURE AT LOCATION 2

5.3 Experiment 74-49, Containerless Processing of Ferromagnetic Materials

This experiment consisted of melting and resolidification of an electromagnetically suspended magnetic alloy. The flight data show that heat was applied to the specimen at T+50 seconds, and the voltage indicated that the melting temperature was not achieved. This was caused by an incorrect setting in the power to the coil prior to flight.

The data show that the RF power amplifier was turned off at T+510 seconds into the flight. All operational parameters looked normal during the flight operational period. The voltage (temperature) profile is shown in Figure 6.

5.4 Experiment 76-20, Containerless Processing Technology

The experiment utilized an acoustic levitator to demonstrate and to study the stability and manipulability of a liquid drop in low-g.

The acoustic levitator apparatus had numerous circuit anomalies during tests and checkouts. These problems included early and unplanned initiation of the camera and premature extension of water droplet injectors due to ground termination problems. Also, when the power was switched from the main bus to the acoustic experiment apparatus, strobe lights operated prematurely and noise was detected in the acoustic generators (speakers). This involved shorted diodes in printed circuit modules to which overload projection was later provided. Each of the problems was resolved prior to launch.

The flight data show that high power and the camera were turned on at approximately T+85 seconds. The injectors extended at T+100 seconds and retracted at approximately T+131 seconds. The "bellows full" measurement indicated that fluid delivery to the chamber was complete at approximately T+107 seconds. However, the low power select function, timed for T+130 seconds (which should have occurred simultaneously with injector retraction), did not occur. This condition caused the acoustic power to be turned off until high power again was turned on at approximately T+260 seconds. The water drop that formed inside the chamber had no sound power to contain it from T+131 seconds until T+260 seconds. It drifted into the wall at 159.6 seconds. All other functions appeared to be normal. Power to the experiment was turned off as planned at T+340 seconds.

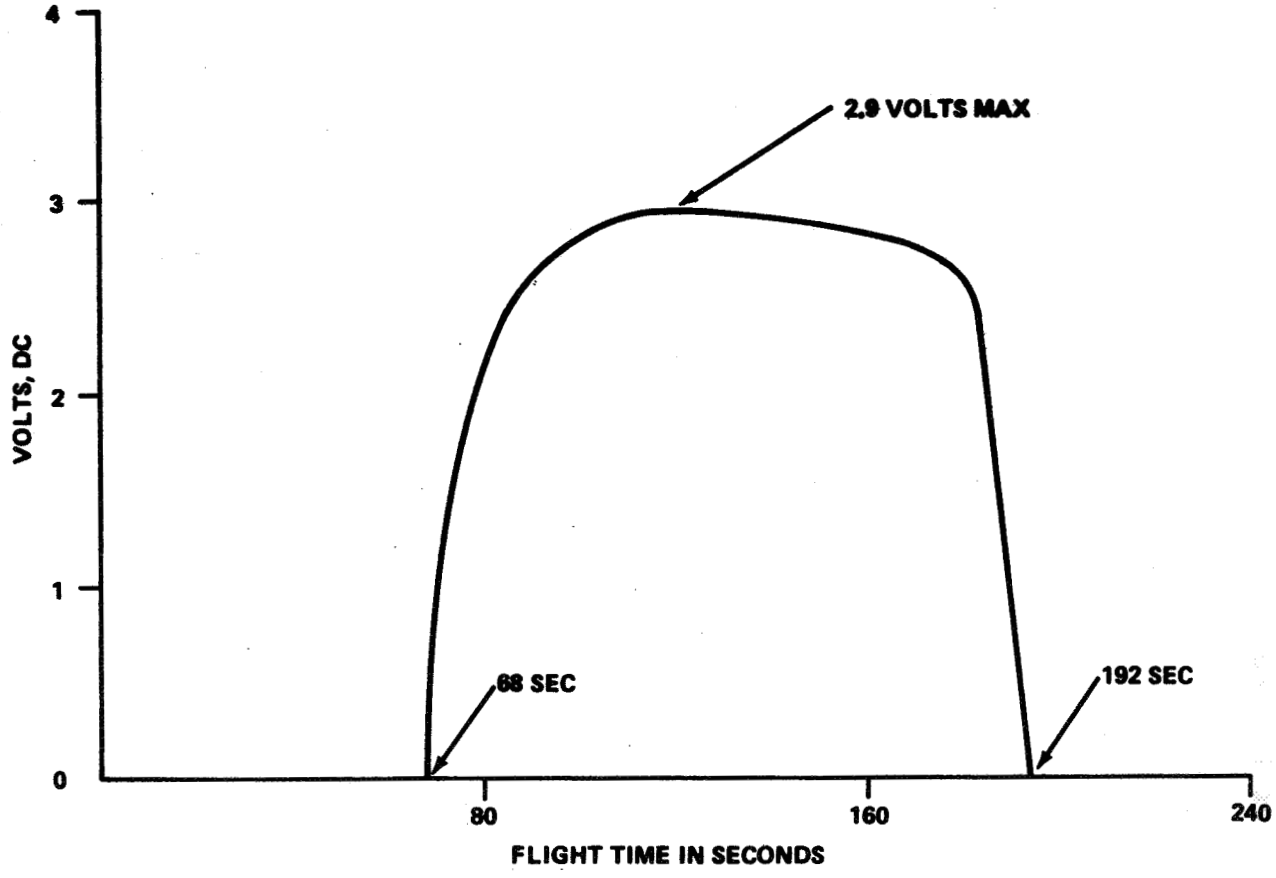

FIGURE 6. EXPERIMENT 74-49 – SPECIMEN TEMPERATURE (VOLTS DC)

For additional information of the experiment problem, the reader should consult the analysis by the PI. Figure 7 gives the injector and power events that show the low power mode did not occur. The voltage should have increased at T+130 seconds to approximately five volts. The voltage drop shown is due to electronic circuit voltage changes. The voltage scale for low power select is shown at the right hand side of Figure 7.

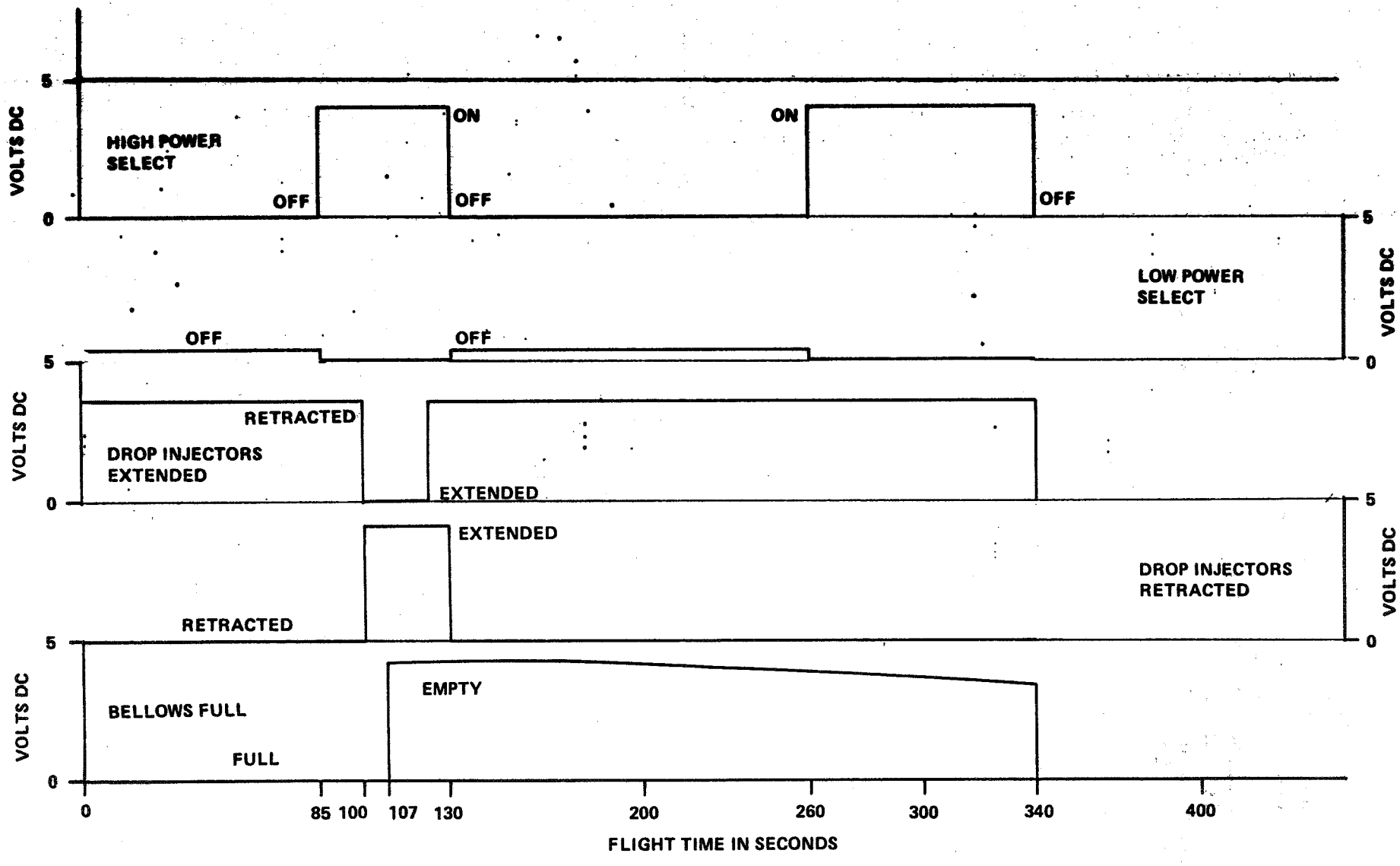

FIGURE 7. EXPERIMENT 76-20 – INJECTOR AND POWER DATA

6.0 Instrumentation Operation

6.1 Temperatures

Flight temperatures on SPAR IV were somewhat lower than SPAR III. The forward end of the payload was 30°C cooler than SPAR III at reentry. There were no thermal anomalies. Temperatures were similar to SPAR I and SPAR II. Figure 8 shows the measurement locations, and Figure 9 shows temperatures reached during the first 500 seconds of flight.

6.2 Pressures

The science payload ambient pressure dropped to 14 Torr at 85 seconds into the flight, rose slightly to 15 Torr, and stablized at 11 Torr at 260 seconds. At 390 seconds into the flight, the pressure increased rapidly at reentry into the atmosphere.

Two experiments, 76-49 and 76-20, required one atmosphere of pressure for proper experiment operation. The data show these pressures were stable throughout the flight.

6.3 Vibration and Shock

No data were available from the accelerometers to evaluate because telemetry was blocked by the mountains prior to impact. All impact-o-graphs were unset and indicated greater than 120 g's on landing. The landing shock is discussed in paragraph 7.0.

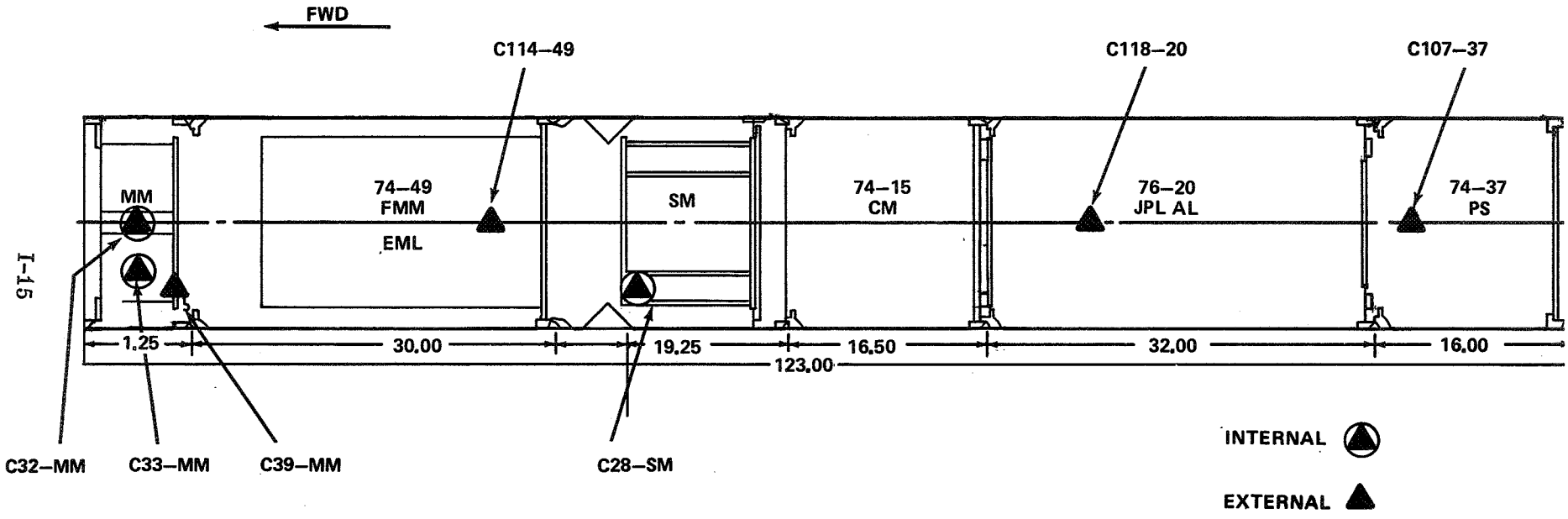

FIGURE 8. SPAR FLIGHT NO.4 ENGINEERING MEASUREMENT LOCATIONS

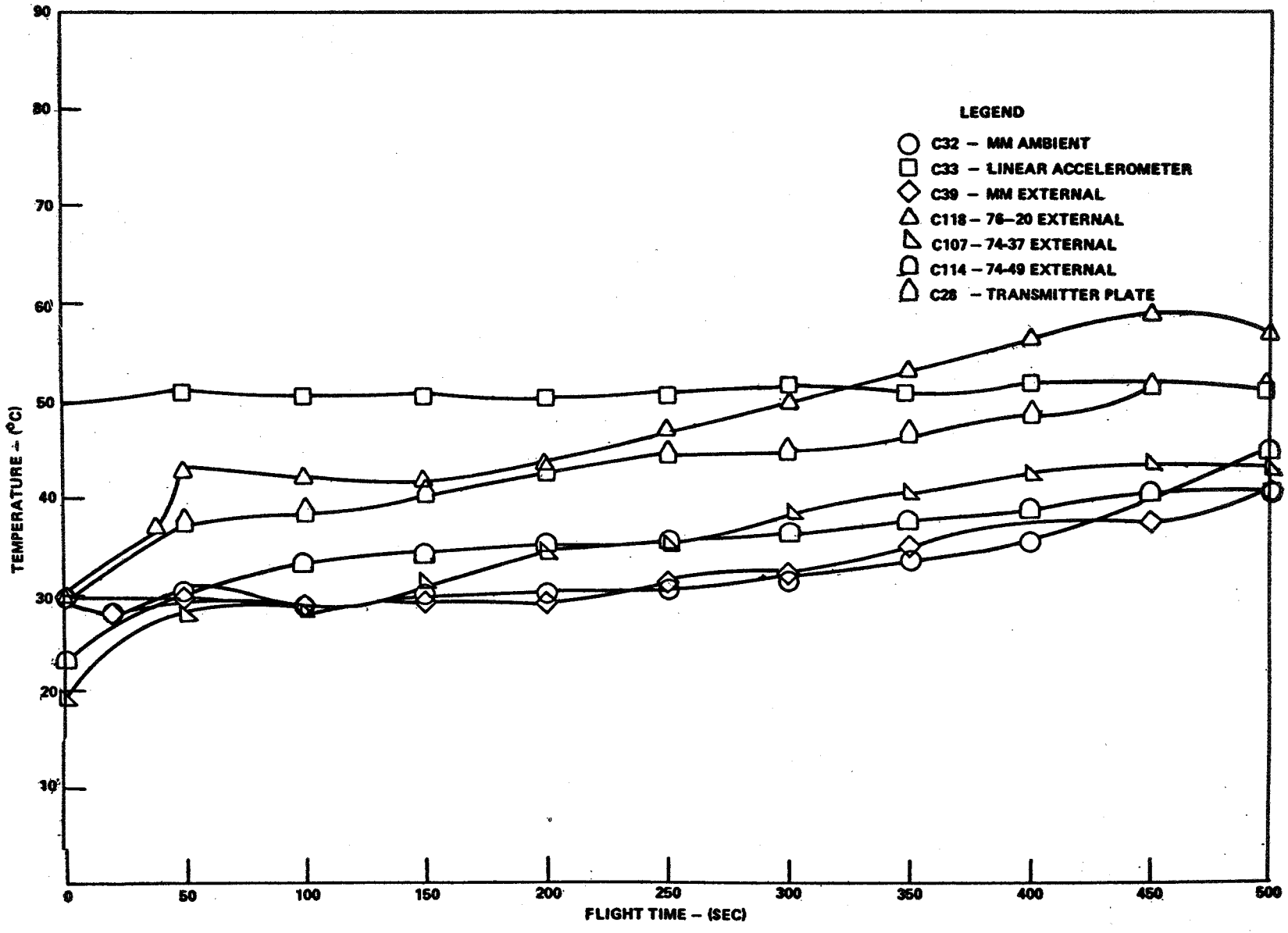

FIGURE 9. ENGINEERING MEASUREMENTS SPAR IV

7.0 Recovery

Telemetry data stopped at approximately T+700 seconds into the flight because the payload was out of telemetry range. Impact time was not available from GSFC for this report nor confirmation for the removal of power from experiment 74-37 which was planned for T+1020 seconds. The impact to ground occurred on a slope, and the payload slid some distance prior to coming to a stop.

The payload landed on the aft side of the vehicle monitoring telemetry extension end plate (see Figure 1 for location, station 185.78). The high impact and landing loads were recorded by nine impact-o-graphs located on the forward side of the telemetry extension. Each of the impact-o-graphs was found unset. These indicated that up to 120 g's were experienced by the payload. The aft plate of the GSFC telemetry extension was torn loose, and experiment 74-49 had some internal structural damage which was found during disassembly. For a tabulation of the impact-o-graphs, see Figure 10 and Table 1.

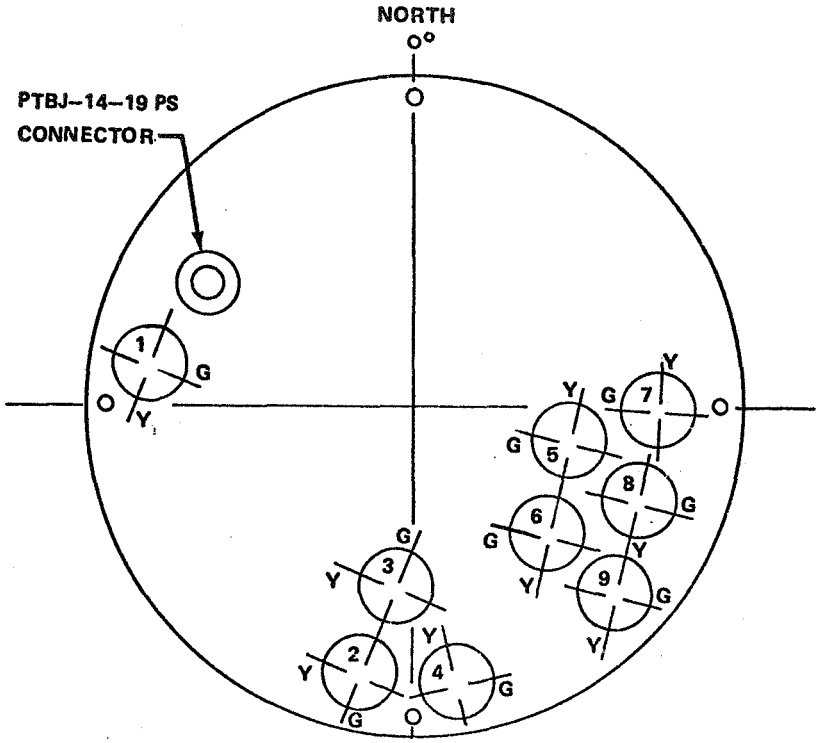

FIGURE 10 . LOCATION OF THE IMPACT–O–GRAPHS ON THE FORWARD SIDE OF GSFC'S SPAR TELEMETRY EXTENSION

IMPACT–O–GRAPH		SPRINGS AND BALLS FOUND UNSET AFTER LANDING		REMARKS [1]
NO	Gs ± 5G	G (GREEN) AXIS	Y (YELLOW) AXIS	
1	70	Yes	Yes	
2	80	Yes	Yes	
3	40	Yes	Yes	
4	90	Yes	Yes	Impact-o-graph was damaged and partially torn from its base.
5	60	Yes	Yes	
6	50	Yes	Yes	
7	120	Yes	Yes	Impact-o-graph was damaged and partially torn from its base.
8	110	Yes	Yes	
9	100	Yes	Yes	

TABLE 1 . LOCATION, NOMINAL G-LEVELS AND THE RESULTS ON SPAR

[1] The payload landed on the aft side of GSFC's SPAR telemetry extension end plate shown in Figure 1. This plate struck a large rock, knocking it loose from the extension. The impact broke an approximately 5-pound piece off one end of the large rock.

8.0 Payload Power Relay Anomaly

The telemetry data indicated the 100-amp relay (K1) did not reset as programmed at T+660 seconds into the flight. This failure is supported by temperature measurement data that should have cutoff at 660 seconds but continued until T+700 seconds when telemetry data were lost. Confirmation of power removal to experiment 74-37 at T+1020 seconds could not be made because the payload was out of telemetry range.

The K1 relay supplies power to the +29-volt bus, which in turn supplies the power to experiments 74-15 and 76-20. Experiment 74-37 received power through relay K4 for the delayed T+1020-second cutoff.

8.1 Relay Postflight Operational Test

A test program was set up at MSFC after the failure of the K1 relay was verified by flight data. The support module was set up in a flight configuration, and two test series of flight sequences were run. The first series of six sequences were run with no failure of the K1 relay, but only two resets were made by the K4 relay. A check of the timer revealed no anomalies. Another series of three sequences were run, and the K1 relay failed to reset one time. The K4 relay failed to reset all three times. The reset coils of each relay were checked and found to be good.

The conclusion reached from this test was that the relay coils in K1 and K4 had intermittent failures. Additional undocumented tests were made on the K1 relay but no failures occurred.

8.2 Relay Postflight Shock Test

The 100-amp relay (K1) was subjected to a series of shock tests to determine if a high-g load, such as an impact load, could cause the relay contacts to open long enough to reset and start the timer in experiment 74-15. These tests measured the contact open time of the relay over a range of accelerations from 120 to 1320's. The longest contact opening was 5 milliseconds which occurred at 1320 g's. The relay specification states that relay chatter will be 10 microseconds or less when subjected to a 50-g shock.

It is concluded from these shock tests that the K1 relay would not break contact long enough to restart experiment 74-15 timer. According to the experiment PI, the relay would have to break contact for at least 50 to 60 milliseconds to restart the experiment cycle.

CHAPTER II

EXPERIMENT 74/15

flown on

SPAR 4

JUNE 21, 1977

Principal Investigator:

Professor Donald R. Uhlmann
Department of Materials Science
and Engineering
Massachusetts Institure of Technology
Cambridge, Mass. 02139

October 20, 1977

I. INTRODUCTION

This report describes Experiment 74/15 which was flown on SPAR 4 on June 21, 1977. Experiment 74/15 is designed to study the behavior of second-phase particles at a solidification front. In general, a solidification interface as it approaches a second-phase particle will either engulf the particle, or reject the particle and push it ahead of the interface. Whether the solidification front pushes or entraps the particle depends on the speed at which the solidification front is advancing, the size and shape of the particles, and the characteristics of the particle-interface interactions. The objective of the experiments is to measure the critical velocity--that is, the maximum velocity at which a particle is pushed by the interface--as a function of a variety of parameters.

Our interest in the behavior of second-phase particles at a solidification front and in studying this behavior in a microgravity environment has been motivated by two principal considerations. First, such behavior seems certain to be important for the fabrication in space of many composite materials having unique microstructures. It already seems clear that uniform and unique dispersions of solid or liquid phases in matrix liquids can be obtained in the space environment. In nearly all attempts to achieve uniform dispersions by crystallization processing, the crystallization of the matrix liquid upon cooling can substantially change the initially uniform distribution of second-phase material due to rejection of the second-phase materials at the solidification front.

Second, and perhaps more important for the overall program of space applications, the understanding and insight gained in the study of particles-at-interfaces in space can be used to provide improved understanding and control of many processes and phenomena on earth. Among the applications areas of the present investigation are the behavior of inclusions in metal castings, the phenomenon of frost heave in soils, the agglomeration of small (micron and sub-micron size) powders of ceramic materials, the development of dust-repellent coatings for glasses, and even the interaction between blood cells and other materials.

In previous work (1-5, e.g.) it was found that at sufficiently small growth rates, particles of nearly all materials are rejected by a moving crystal-liquid interface; i.e., they are pushed ahead into the liquid, traveling along with the interface as it advances. Particles can thus be pushed for long distances (thousands of times the particle diameters).

It is apparent that the pushing of a particle or pile-up of particles by an interface demands both a force preventing incorporation of the particle in the crystal and feeding of fresh material to the region of the interface immediately behind the center of the particle. The interaction of the particles with the interface, which is responsible for their rejection from the growing solid, can be represented in terms of a short-range repulsion which exists between the particle and the solid. The particle becomes incorporated into the solid when liquid

cannot diffuse sufficiently rapidly to the growing solid behind the particle.

The present investigation is concerned broadly with developing improved understanding of the interaction between second-phase particles and an advancing solidification front, and with developing criteria for the solidification processing of many two-phase composite materials in space. The elimination in space of the effects of density differences between particles and matrix offers the opportunity for systematically determining the factors which are important to the phenomenon of particle rejection and incorporation.

In addition to obtaining appropriate experimental data, the investigation is also concerned with developing a satisfactory theoretical description of the behavior of second phase particles at a solidification front. In this work, the forces of interaction between particles and interfaces are being computed from the refractive indices, characteristic absorption frequencies and static dielectric constants following the approach suggested by Lifshitz (6). Also being explored is the approach suggested by Neumann (7), in which the interaction is evaluated from measurements of contact angles. Both descriptions of the interaction, particularly the former, are being combined with a description of the relevant transport phenomena to obtain theoretical predictions of the critical velocities.

With this background, let us consider the SPAR 4 experiment and the results of the ground-based studies.

II. GROUND-BASED STUDIES, CRITICAL VELOCITY

The single most important parameter used to evaluate the interaction of second-phase particles with a solidification front is the critical velocity. As indicated above, the critical velocity is the solidification rate below which the particles are rejected by the advancing interface and above which they are incorporated into the growing crystal. The critical velocity can conveniently be measured on earth by carrying out solidification in either of two geometries: (1) a horizontal geometry in which the sample is contained within a thin chamber, with the particles resting (because of gravity) on the bottom support of the chamber, and the solidification behavior observed through a microscope as the interface advances horizontally; and (2) a vertical geometry in which the particles rest on the interface (because of gravity) as the interface advances vertically upward. In this case, the behavior has usually been characterized by measuring the distribution of particles after solidification rather than by direct observation during the solidification. In both cases, the effects of gravity introduce a significant complication into the measurement.

In the majority of the work carried out to date in our laboratory, the horizontal solidification geometry has been employed. Selected particles are mixed into a molten sample contained between a glass support and a cover glass; and the sample is cooled and crystallized rapidly. The resulting sample is typically in the range of 50-200 microns in thickness, and is confined between two glass plates. The

sample is then located in a controlled temperature gradient and is traversed through the temperature gradient by a motor-driven screw to provide the desired rate of solidification. When viewed through a microscope at magnifications in the range of 100 X, particles as small as 2-5 microns in diameter can easily be seen, and their behavior can be followed individually as solidification proceeds. By varying the solidification rate, the critical velocity for each type (and size) of particle can be measured.

While this geometry has the disadvantage that the particles rest on the bottom supporting glass plate and are subjected to unknown frictional forces, the thin horizontal geometry has the advantage of simplicity and ease of viewing the sample at high magnification over a range of readily controlled growth rates.

The apparatus used for the measurements with a vertical geometry is the single cell version of the flight apparatus, which is discussed in detail in the following section. The single cell apparatus is used with a microscope to permit visual observation of the particles during the experiment. Hence the observational technique is the same as that employed with the horizontal geometry apparatus.

Previous measurements of critical velocities have been carried out for a number of particle-matrix combinations. In all cases, the matrix materials have been characterized by entropies of fusion which are large in Jackson's sense (8). Since the entropy of fusion has been demonstrated to have significant effect on the crystal-liquid interface

morphology as well as upon many characteristics of the crystallization process, it has seemed highly desirable to explore the behavior of second-phase particles in matrix materials characterized by low entropies of fusion. In addition to the intrinsic interest in such behavior, our concern in this regard has been prompted by the fact that metals are characterized by small entropies of fusion. For this reason, carbon tetrabromide (CBr_4), which has a small entropy of fusion, was chosen as the first matrix material for the SPAR 1 flight. Ground-based measurements of the critical velocity for various particles in CBr_4 were carried out. The particles which were investigated included zinc, tungsten, oxide glasses of two compositions, aluminum oxide, ferric oxide, and zinc sulfide. No particle was observed to be pushed at the lowest growth rate measurable on our equipment (0.1 micron sec^{-1}). CBr_4 could therefore not be used in subsequent experiments.

For this reason, a survey of the critical velocities of low entropy of fusion organic materials was undertaken. Some of the results are given in Table I along with a few of the high entropy of fusion organic materials which were also studied. The other low entropy of fusion materials identified by Jackson (9) were not available in sufficient purity to be usable.

As seen in Table I, d-camphor is the only low entropy of fusion material which exhibits particle pushing at reasonable solidification rates. The critical velocities for particle pushing were measured for camphor with a variety of second-phase particles. Some of the results

TABLE I

Critical Velocities of Zinc and Glass Particles in Various Organic Matrix Materials

Name and Formula		$\Delta S_F/R$	T_M °C	V_C in μm sec^{-1} ∿5μm particles Zn	Glass
Low Entropy of Fusion					
Carbon Tetrabromine		1.2	90.1	<0.1	<0.1
Succinonitrile	$CN-CH_2-CH_2-CN$	1.4	57.1	<0.1	<0.1
d-Camphor	$C_{10}H_{16}O$	1.4	179.0	6	1.5
High Entropy of Fusion					
Phenantherene	$C_{14}H_{10}$	6.0	101	1	<0.2
Thymol	$C_{10}H_{14}O$	6.4	49.6	4	1.5
Naphtalene	$C_{10}H_8$	6.7	80.1	45	
Durene	$C_{10}H_{14}$	7.2	70.2	7	
Pyrochatechol	$C_6H_6O_2$	7.3	105	4	1-2
Eicosane	$CH_3-(CH_2)_{18}-CH_3$	18.2	36.6	18	

are summarized in Table II.

These results are being analyzed using the model of Lifshitz to describe the particle-interface interaction in terms of their bulk dielectric properties. In order to apply this theoretical framework, it is necessary to measure the dielectric constants of the materials over a broad range of frequency. We are presently measuring the static (radio frequency), the infrared, and the ultraviolet dielectric properties of camphor and naphthalene. We plan to report on this phase of the investigation in the near future.

Besides the interaction between the particle and the solidification interface, the drag force on the particle is also important in determining the critical velocity. The drag force arises from the difficulty of feeding fluid behind the particle to the growing interface. The drag force can be approximately calculated if the shape of the interface near the particle is known. The shape of the interface behind the particle may be strongly affected by the relative thermal properties of matrix and particle. If the particle is much more conductive than the matrix, as is most often the case for organic matrix materials, the front will curve behind the particle; and the drag force will be considerably increased. To study this problem in more detail, we are presently analyzing the shape of the interface in the vicinity of the particle using finite element methods.

In summary, we have made extensive ground based measurements of the critical velocities of particles of different thermal conductivities,

TABLE II

Critical Velocities in Camphor

Material	Diameter in μm	Critical velocity in μm sec^{-1}
Nickel	3.0	8.0
	5.3	4.0
	8.8	2.1-3.8
	10.6	1.5
	pile-up	1.5-4.2
Glass	5.5	1.8
	11.	1.4
	28.	0.4

size, roughness, etc. in a variety of organic matrix materials. We are seeking to understand the results of these measurements by formulating a new treatment of the phenomenon based on the Lifshitz treatment of the particle-interface interaction coupled with a more accurate description of the drag force based on a knowledge of the shape of the solidification front.

III. FLIGHT EXPERIMENT

It was necessary to design a scientifically valuable experiment which would meet the design requirements of the sounding rocket environment: (1) high acceleration and vibration levels; (2) only a short microgravity experiment period; and (3) power, size, and weight limitations. As detailed above, d-camphor was chosen as the organic matrix material. Unfortunately camphor is a difficult material with which to work; it has a melting point of 178°C, a narrow liquid temperature range, and a high vapor pressure.

The ground based experimentation coupled with the results of the SPAR 1 experiment detailed the following design considerations:

(1) It is necessary to control carefully the shape and speed of the solidification front to achieve a useful experiment. Since the telemetry is not sufficiently accurate to measure the position and speed of the front, it is necessary to build an apparatus which will precisely repeat the same cycle for each experiment. The telemetry will be used to detect malfunctions in the apparatus.

(2) The solidification process should at least in some cases be photographed at sufficiently high magnification such that individual particles can be seen at the interface.

(3) The sample chamber must be transparent with flat walls to permit effective photographic recording. Extensive finite element thermal calculations indicated that control of the solidification conditions and the interface shape can be best achieved with a thin sample (but thick relative to the diameter of the largest particles being studied). This choice is also required to obtain short thermal time constants for melting and solidification.

(4) The sample must only be melted in the microgravity environment to avoid the particles settling out of their initial dispersion.

Based on the above design criteria, fused silica (quartz) was chosen as the sample cell material. It might be noted that plastics could not be used because of the temperature at which camphor melts, 178°C, and its corrosive character.

The sample cell assembly is shown schematically in Figure 1. The quartz sample cell is 3.4 cm high with a 5 mm long fill tube extending from it. The sample thickness is 0.008 inch (200μm). The wall thickness of the quartz cell is 1.5 mm. The cell is 1.3 cm wide. Separately controlled aluminum heater blocks at each end of the cell control the temperature profile in the cell. An expansion reservoir with a Teflon diaphragm compensates for volume changes in the camphor

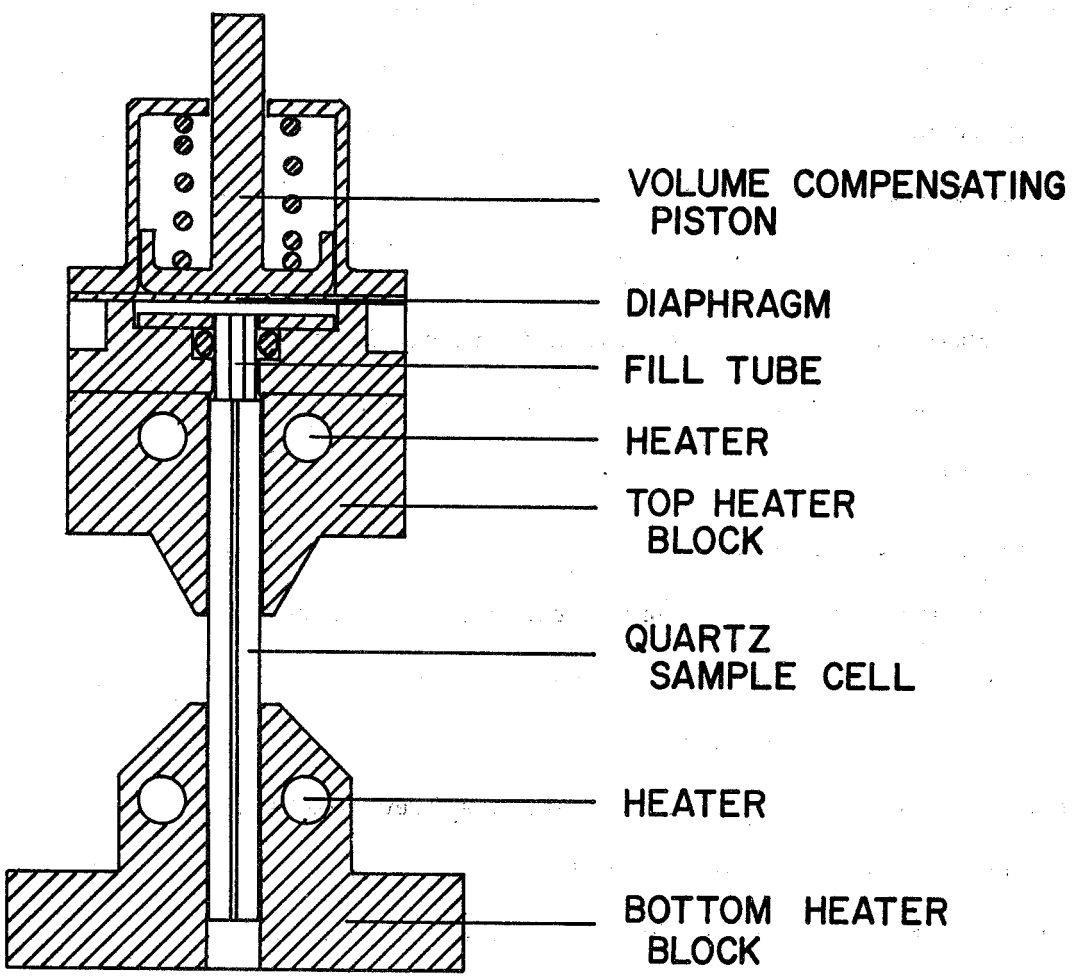

Figure 1 - Sample cell assembly

upon solidification or melting. The sample cell is sealed to the volume compensating chamber with a Teflon o-ring. The entire sample cell assembly is enclosed in a gold plated copper can which reaches the temperature of the bottom heater block. The gold plated can reduces the radiational cooling of the exposed quartz cell and isolates each sample cell from its surroundings.

A sample cell assembly as shown in Figure 1 was used in the "single cell apparatus" for the ground based testing and measurement of the critical velocities.

The approximate experiment cycle for each cell is shown in Figure 2. At four minutes before launch, the heaters are turned on to bring the cells to their preheat temperature of 176°C at the top heater block and 173°C at the bottom heater block. At 74 seconds after launch when the microgravity portion of the flight has been reached, the sample is melted by raising the temperature of the top heater block to 197°C and lowering the temperature of the bottom heater block to 164°C. Thus a stable solidification interface is created in a temperature gradient of about 60°C cm^{-1}. At 119 seconds, the slow controlled solidification of the sample begins by changing the set point of both the top and bottom temperature controllers at a constant rate. This rate is, of course, set by the desired growth rate of the solid but is about 1°C min^{-1}. At 310 seconds, the experiment is over and the heaters are turned off to start freezing rapidly the solid before reentry occurs.

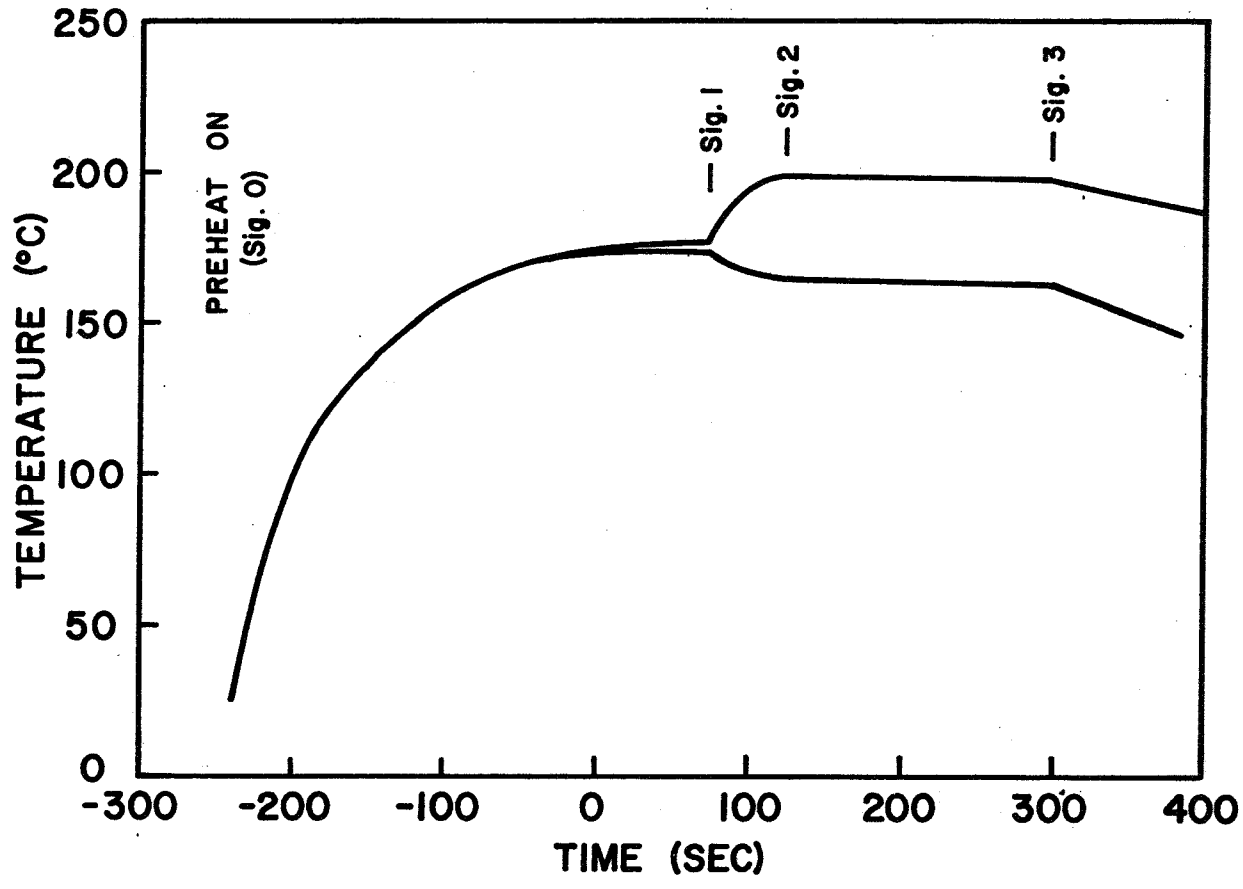

Figure 2 - Approximate temperature cycle of both top and bottom heaters of the sample cell assembly.

The flight apparatus consists of seven sample cell assemblies, a temperature controller for both top and bottom of each of the seven cells, the necessary control electronics, and a camera and lens assembly to photograph one of the seven cells. A Nikon camera with a 250 exposure back is used to photograph one cell at approximately 17X using a 19 mm Nikkor lens at approximately 50 frames minute $^{-1}$

IV. SPAR 4 EXPERIMENT AND RESULTS

The experiments flown on SPAR 4 are shown in Table III. Each experiment was chosen with a solidification rate and a range of particle diameters such that the largest particles are not pushed in the ground based experiments but the smaller particles are easily pushed. The final distribution of particles is then measured after recovery of the apparatus and analyzed to measure the critical velocity.

The telemetry indicates that the apparatus functioned correctly during flight.

One sample, cell # 7, was photographed during flight. Photographs 1-5 are taken from the flight photographs. For clarity, only one corner of the original negative is shown. From these photographs, we note the following information:

(1) The samples were not melted before launch. Hence the samples retain their initial particle dispersions.

(2) The sample melted back to approximately the correct location, leaving the particles dispersed in the liquid.

TABLE III

Experiment Set-up (SPAR 4)

Cell No.	Particles	Growth rate in 10^{-6} m/s
1	glass (0-20μm)	2.2-2.6
2	glass (10-30μm)	1.2
3	glass (0-10μm)	5.0
4	Ni (3-10μm) + glass (0-10μm)	7.6
5	" "	5.0
6	glass (0-20μm)	2.1
7	glass (0-20μm)	1.4

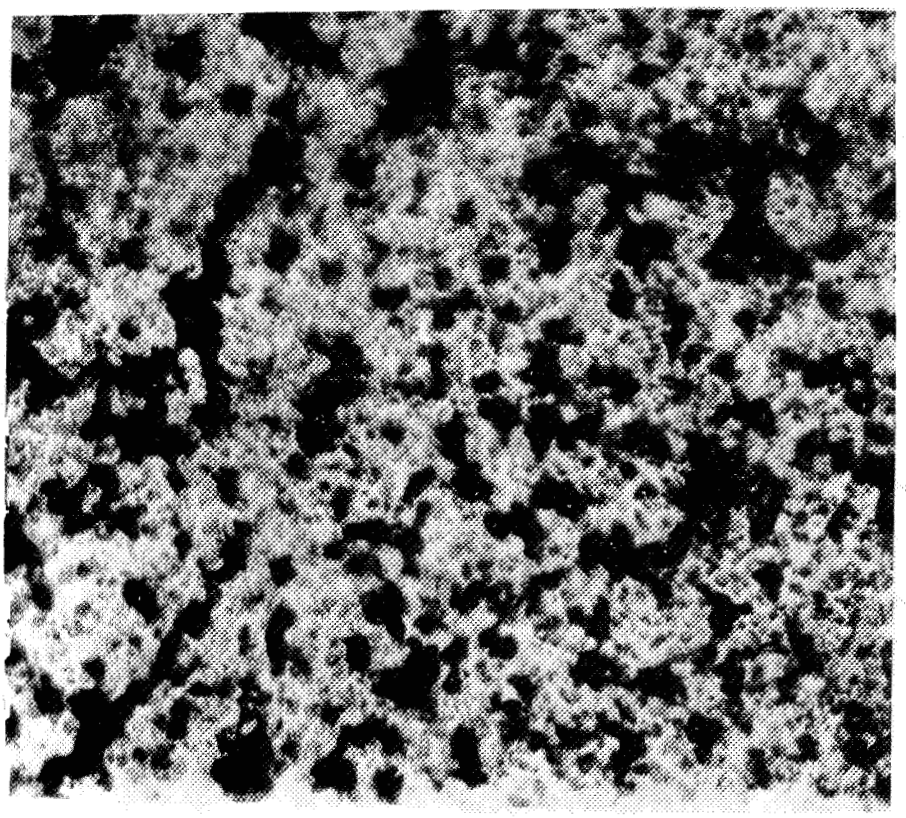

Photograph 1 - Frame 1 from SPAR 4 flight sequence. Taken before launch, this photograph shows that the sample was not melted prior to launch.

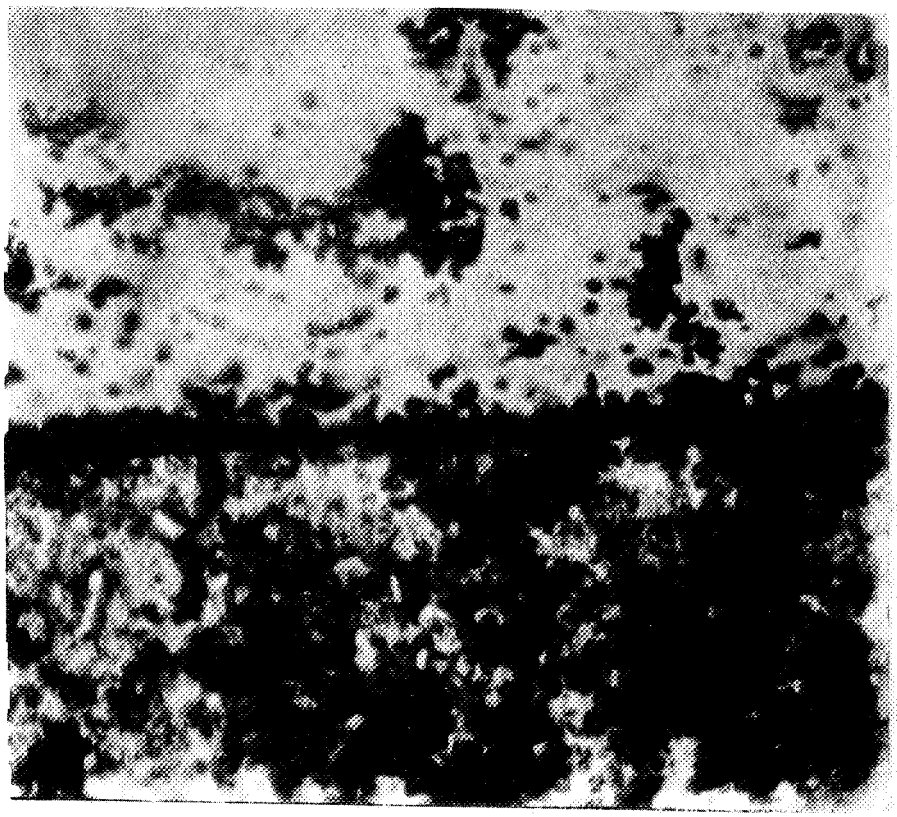

Photograph 2 - Frame 43 from SPAR 4 flight sequence. The sample has melted to create a solid-liquid interface with the solid at the bottom of the photograph and the liquid at the top.

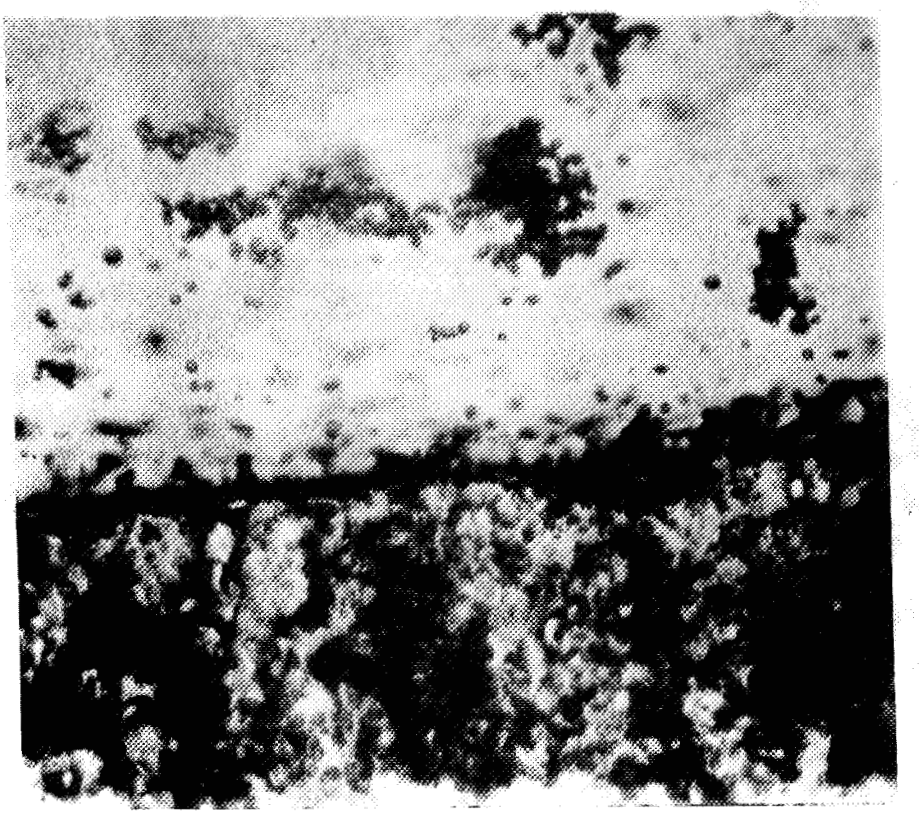

Photograph 3 - Frame 48 from SPAR 4 flight sequence. The number of particles visible in the photograph has decreased.

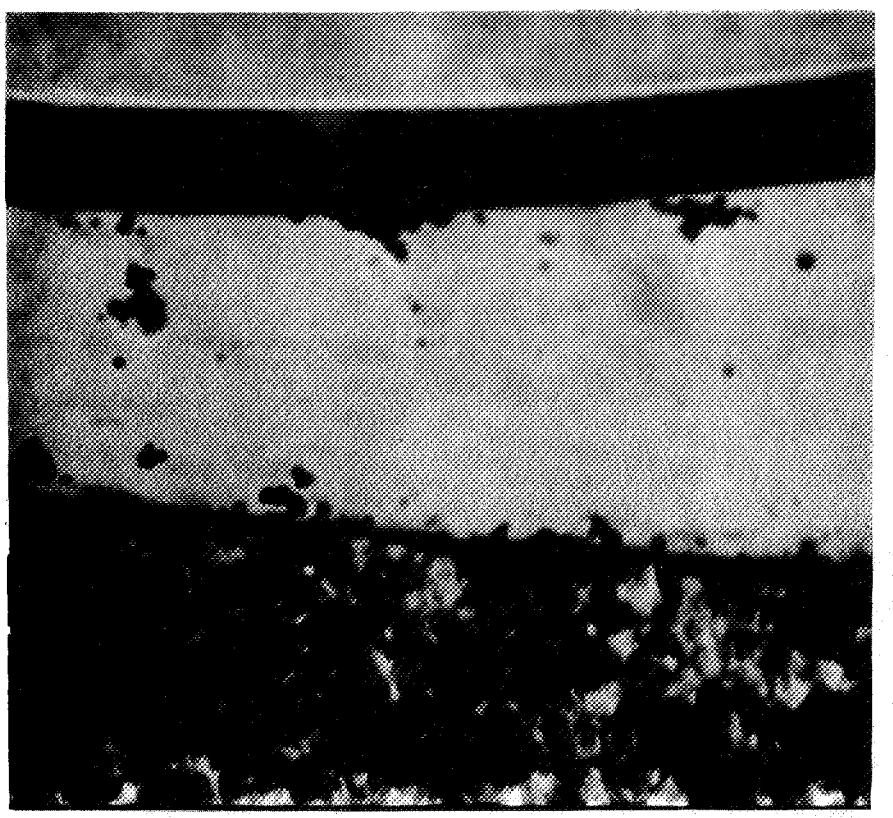

Photograph 4 - Frame 54 from SPAR 4 flight sequence. The dark band at the top of the photograph is the liquid-vapor interface which was observed because the sample cell cracked, allowing camphor vapor to escape.

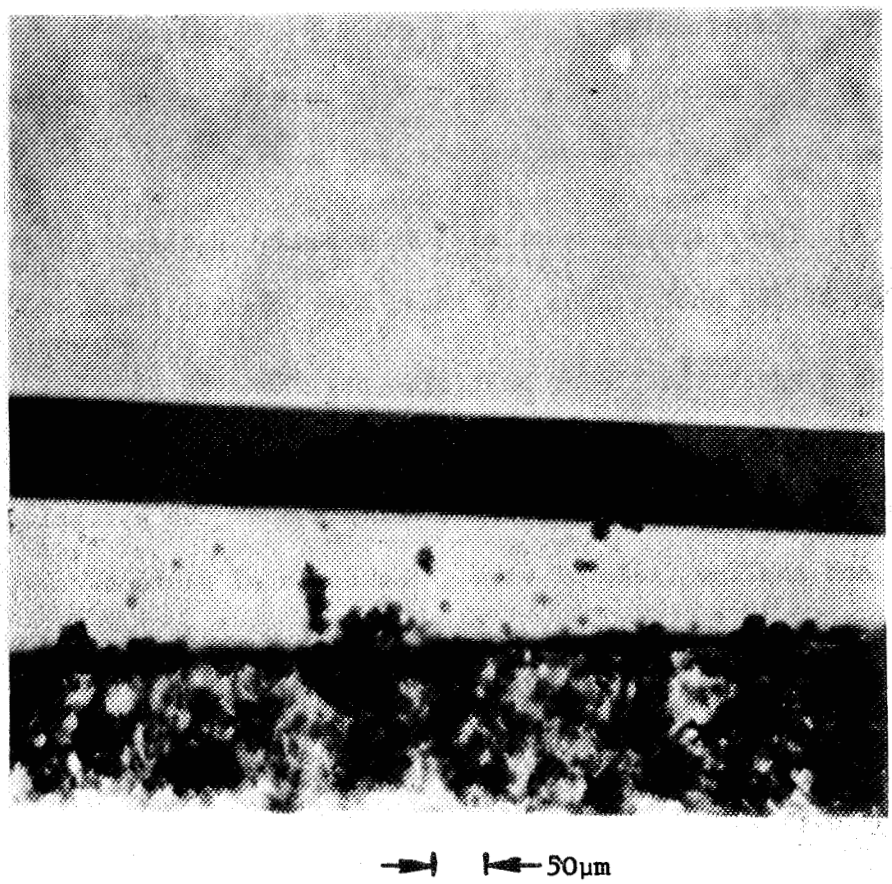

Photograph 5 - Frame 81 from SPAR 4 flight sequence. The liquid-vapor interface continues to advance as the cell leaks by vapor loss. The presence of the vapor changes the temperature gradient in the cell so more solid has melted.

(3) Unfortunately, when the camphor was melted, the camphor evaporated from the sample cell through a small crack in the side of the cell.

(4) The dispersed particles in the liquid disappear from the field of view of the photographs, as noted by comparing frames 43 and 48.

We suggest that fewer particles are observed dispersed in the liquid camphor as the liquid-vapor interface approaches because of a surface tension driven convection which sweeps the particles out of the small and shallow field of view. The depth of field of the camera system is only about 50μm. The particles are sufficiently small that an out-of-focus particle will not be visible.

The likelihood of surface tension induced convection currents can be estimated using the Marangoni number. In our case, the Marangoni number is approximately 10^3 - 10^4, indicating that surface tension driven convection is quite probable when a liquid-vapor interface is present. It must be noted, however, that a quantitative description of the Marangoni flow in our geometry and temperature profile is not feasible since most of the previous work has been directed toward a fluid layer in which the temperature gradient is normal to the fluid layer. Despite the lack of a quantitative analysis, the disappearance of the particles from the field of view seems reasonably explained by a surface tension driven convection.

While the sample cell which was being photographed developed a crack, the other six cells survived without problems. To ensure the

quality of the cells flown on SPAR 4, each cell after it was assembled into its sample cell assembly was pressure tested to one atmosphere both at room temperature and at its operating temperature. The cell assembly was also vibration tested on three axes to the following levels: 10-24 Hz 0.7 inches D.A., 24-100 Hz 20g, and 100-500 Hz 5.3 g at a sweep rate of 2 oct min^{-1}. These vibration levels were based on the results of an instrumented test of the 74/15 apparatus when it was vibrated at the design qualification levels given in Environmental Design and Qualification Test Criteria for Black Brant VC Space Processing Sounding Rocket Science Payload. The vibration tests of each sample cell were chosen to exceed the vibration levels measured on the shock mounted base plate to which the cells are mounted.

The cell failures which occurred during the testing program could not be directly attributed to the vibration testing; instead, the cracks in the cells appear to result from crack initiation and growth from a flaw such as a scratch. In the case of the # 7 cell from the SPAR 4 flight, the fracture originated from a flaw where the two flat plates of the cell were joined together. We plan to tighten our screening and testing procedure and change the technique of cell fabrication to reduce and hopefully eliminate the possibility of the recurrence of such a failure.

The other six samples were carefully photographed and examined after recovery. The critical velocity with these samples is determined by carefully examining the distribution of the particles as a

function of particle size in the region of controlled solidification.

Photograph 6 shows cell # 1 at a low magnification in which the entire sample region of (5.5 mm) high and about 13 mm wide is visible. The edges of the cell are not transparent because of the grinding necessary to fit the cell into its aluminum heater block sample assembly. The bottom half of the photograph is the virgin region of the sample which maintains the original dispersion of the particles. In approximately the middle of the photograph (top to bottom) there is a clear band. This clear band is the camphor which was slowly and carefully grown during the controlled solidification period. It is in this region of controlled growth that the particle pushing and/or rejection will occur and be analyzed. Above this clear region, there is a region of rapid solidification of the samphor, denoted by the presence of small bubble-like voids, which formed after the period of controlled growth.

The particles, glass spheres of diameter less than 20μm, are visible at this magnification as a dark band at the bottom of the region of controlled growth. The distribution of particles is more clearly shown at higher magnification in Photographs 7 and 8. Photograph 7 shows the sample cell from the same side as in Photograph 6. The controlled growth region is in the center of the photographs, with the virgin region seen at the bottom and the rapid growth region at the top of the photograph. The particles (visible as clear circles with a dark boundary)

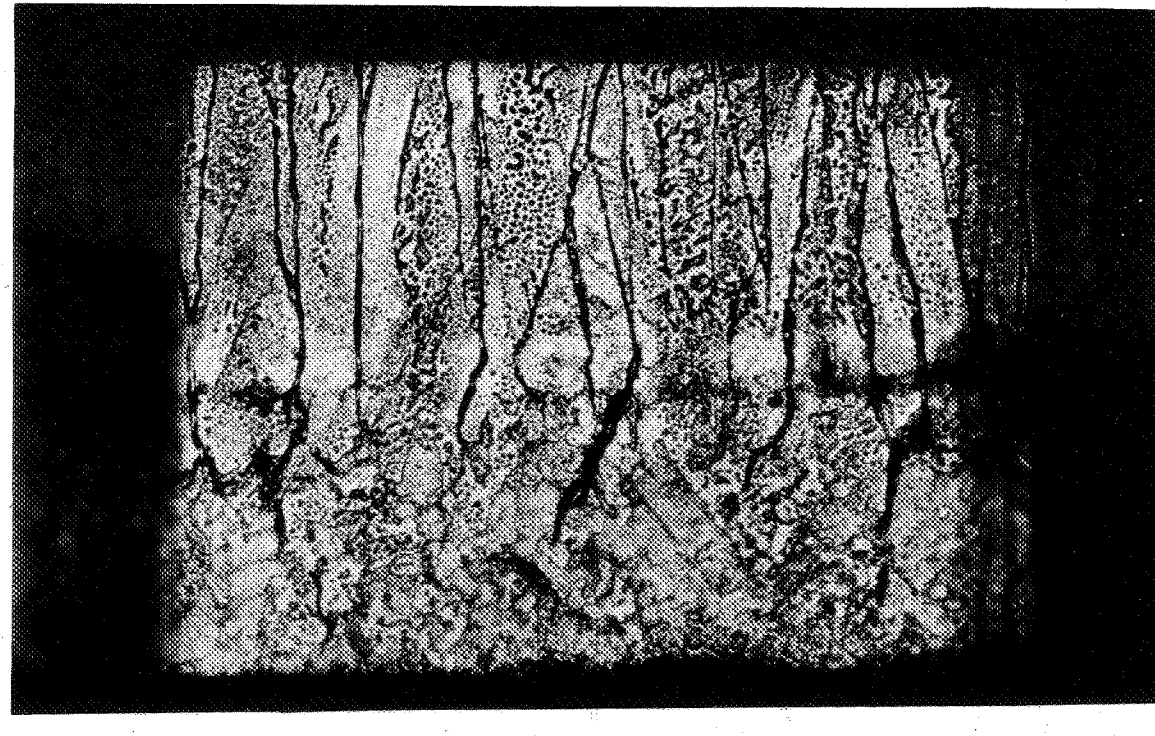

Photograph 6 - Cell # 1 at low magnification.

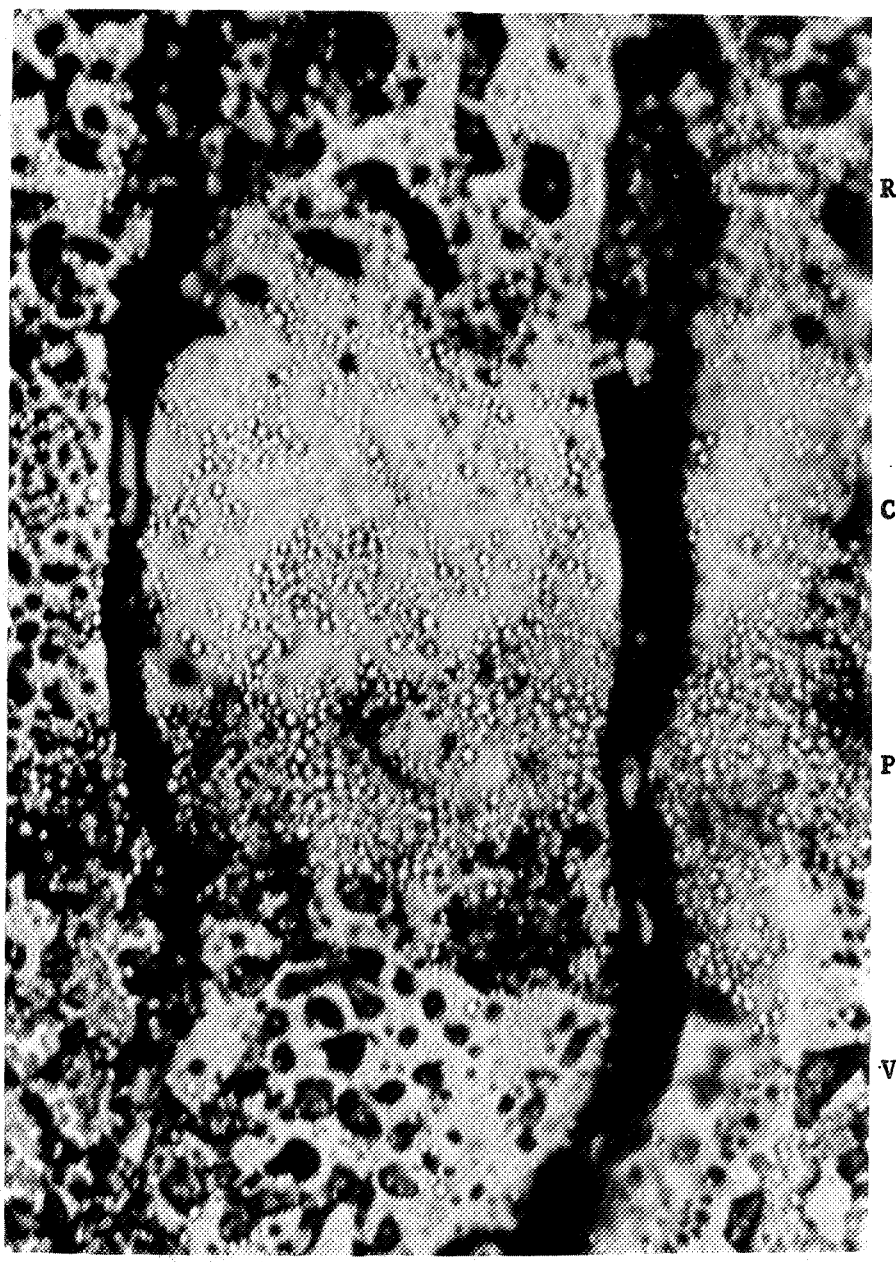

Photograph 7 - Cell # 1 photographed from the same side of the cell as in Photograph 6. The particles are at the cell wall closest to the camera.

Photograph 8 - Cell # 1 photographed from the other side of the sample cell from Photographs 6 and 7. The particles are at the other side of the cell and hence are out of focus.

are predominantly located in a large pile at the bottom of the controlled growth region. For this pile to occur, there must have been a force exerted on the particles to cause them to fall out of their dispersion when the sample was melted back to its furthest extent. Particles are visible in the virgin region of the sample; and some particles are seen above the large pile-up of particles. Examination of both Photographs 7 and 8 demonstrates that the particles above the pile-up are at the cell wall on one side of the cell. It is not unusual for a few particles to adhere to the wall of the cell in even ground-based experiments. The fact that these particles are in the controlled growth region cannot be considered evidence that particle pushing occurred. Particles which are at the cell wall must be disregarded in analyzing the particle distribution for particle pushing. Hence, one must conclude that no particle pushing is evident in this sample.

The distribution of particles in Cell # 1 after the SPAR 4 flight is illustrated in Figure 3 with both horizontal and vertical sections in the region of controlled growth. The horizontal section shows that the pile-up of particles is predominantly toward one wall of the cell. The vertical section shows the same distribution in relation to the distribution of particles in the virgin sample. The significance of the positions of the particles will be discussed following a presentation of the results from the other sample cells.

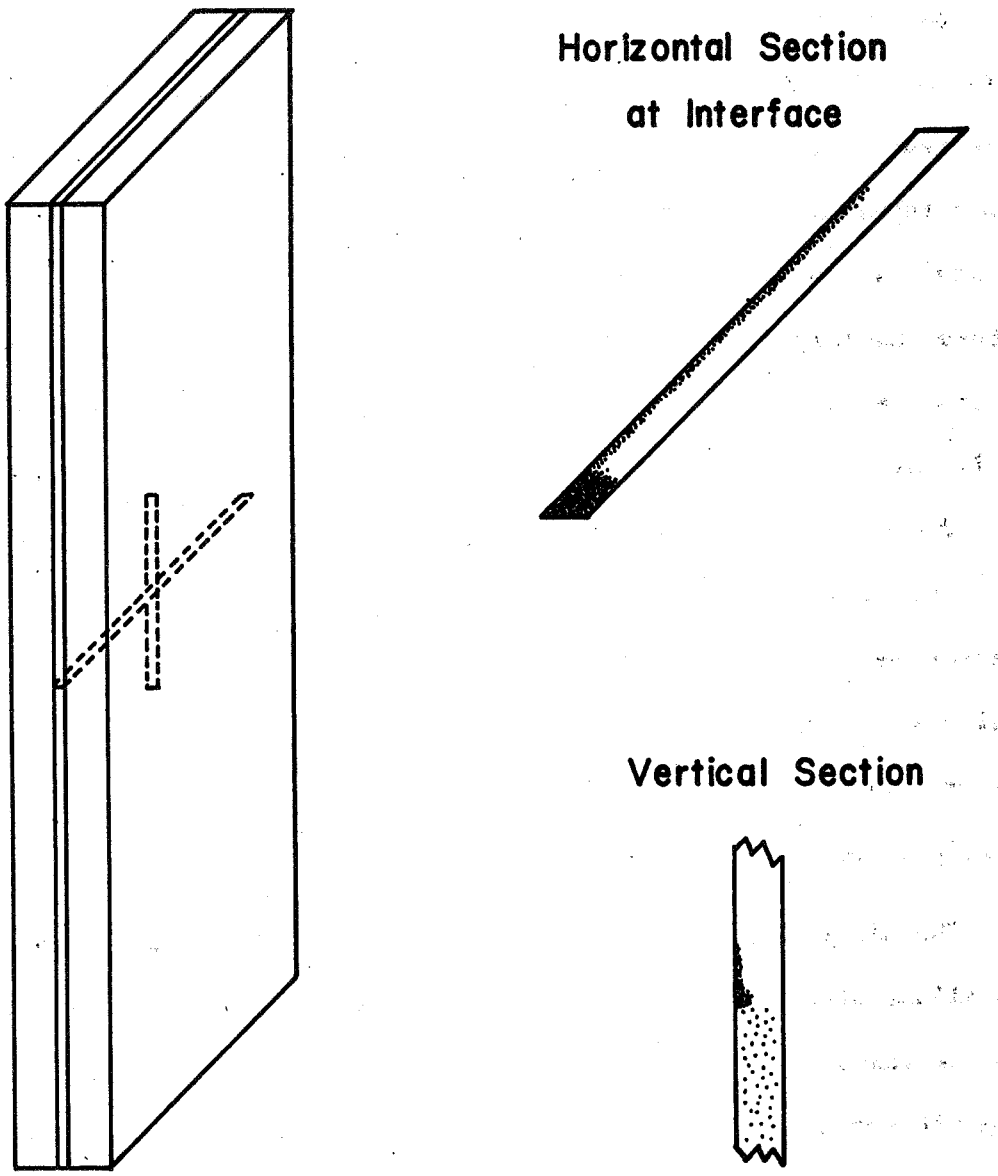

Figure 3 - The distribution of particles in Cell # 1 after the SPAR 4 flight. Note the difference in the distribution of particles in the vertical section between the initial dispersion retained in the virgin sample at the bottom of the cell and the pile-up of particles in the melted sample above.

Cell # 2, which also contained glass spheres is shown in Photographs 9 and 10. The distribution of particles in this cell is similar to that in Cell # 1. Again, there is a large pile-up of particles along the interface between the virgin sample and the controlled growth region.

Cell # 3, which also contained glass spheres, is shown in Photograph 11. Again, there is a pile-up of particles along the interface between the virgin and controlled growth regions of the sample.

Cell # 4 contained both nickel particles (3-10μm) and glass spheres (less than 10μm); this cell is shown at low magnification in Photograph 12. Again the particles in this cell have fallen out of their initial dispersion and are observed in a pile up. Unlike the other cells, however, the pile-up of particles lies predominantly on a plane tilted approximately 60° from the normal interface plane. Photographs 13 and 14 at higher magnification show the pile-up of particles at the front and back wall respectively with only the closer particles in each photograph in focus.

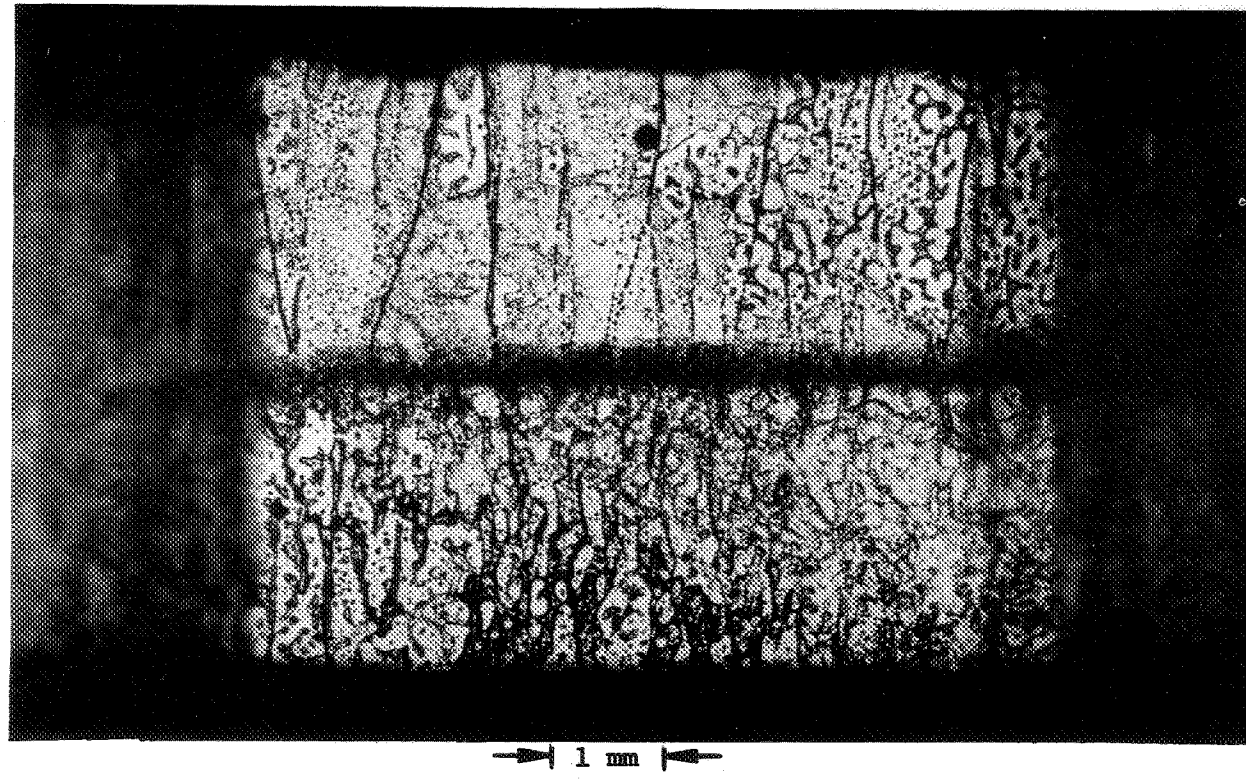

Photograph 9 - Cell # 2 at low magnification.

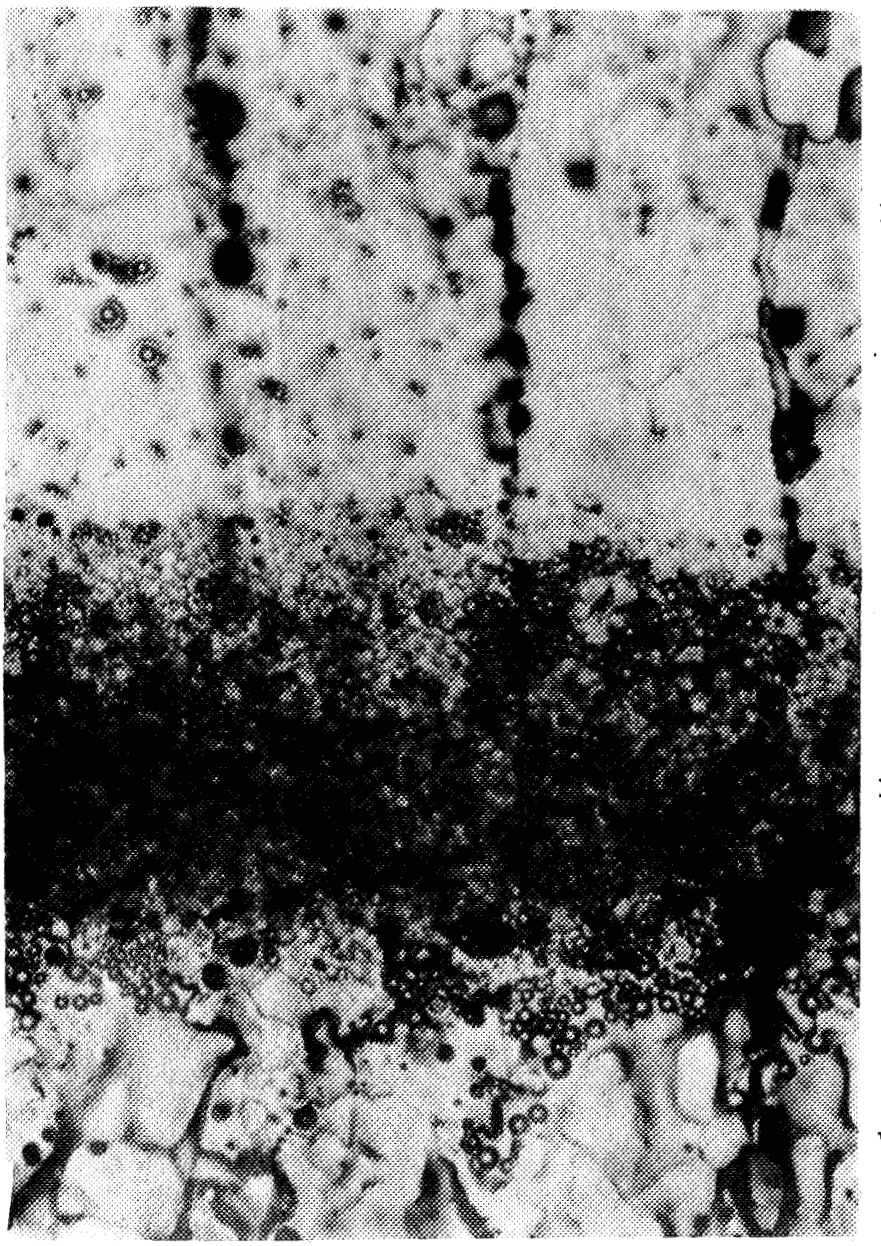

Photograph 10 - Cell # 2 showing particle Pile-Up.

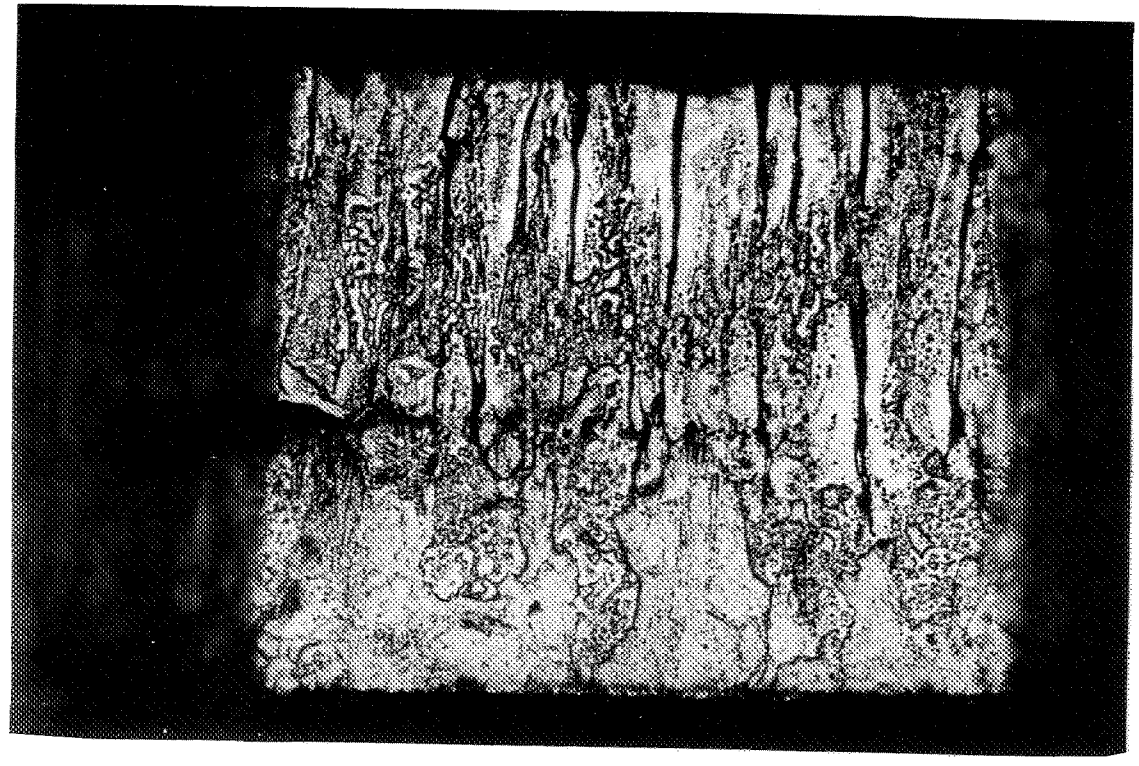

Photograph 11 - Cell # 3 at low magnification

Photograph 12 - Cell # 4 at low magnification

Photograph 13 - Cell # 4 photographed from same direction as in Photograph 12.

Photograph 14 - Cell # 4 photographed from other side of cell than Photographs 12 and 13. The particle pile-up is tilted with only the particles at the near wall in focus.

There is some evidence that particle pushing occurred in Cell # 4, as can be seen in Photograph 12. The smaller particles should have been pushed at the solidification rate of the experiment, so pushing of a small pile of particles could easily have occurred. In any case, this experiment will be repeated in the next rocket flight to confirm the result.

Cell # 5, which is shown in Photograph 15, also contained nickel (3-10μm) and glass (less than 10μm) spheres. Again, the particles are found in a pile-up at the interface between the virgin region and the controlled growth region. Unlike Cell # 4, there is no evidence of the particle pushing. The concentration of glass spheres in Cell # 5 were larger than in Cell # 4, however; and the larger concentration of particles (with the concomitant larger pile-up and larger drag force) could well explain the difference in pushing behavior.

Cell # 6 contained glass spheres less than 20μm in diameter. Photograph 16 shows a low magnification view of the cell. Again, the particles are deposited in a plane at the interface between the virgin region and the region of controlled growth. The cause of the unusual slanted region in the bottom half of the photograph has not been established. It may well represent a second melt-back process (as will be discussed below), but the characteristics of this process remain to be clarified.

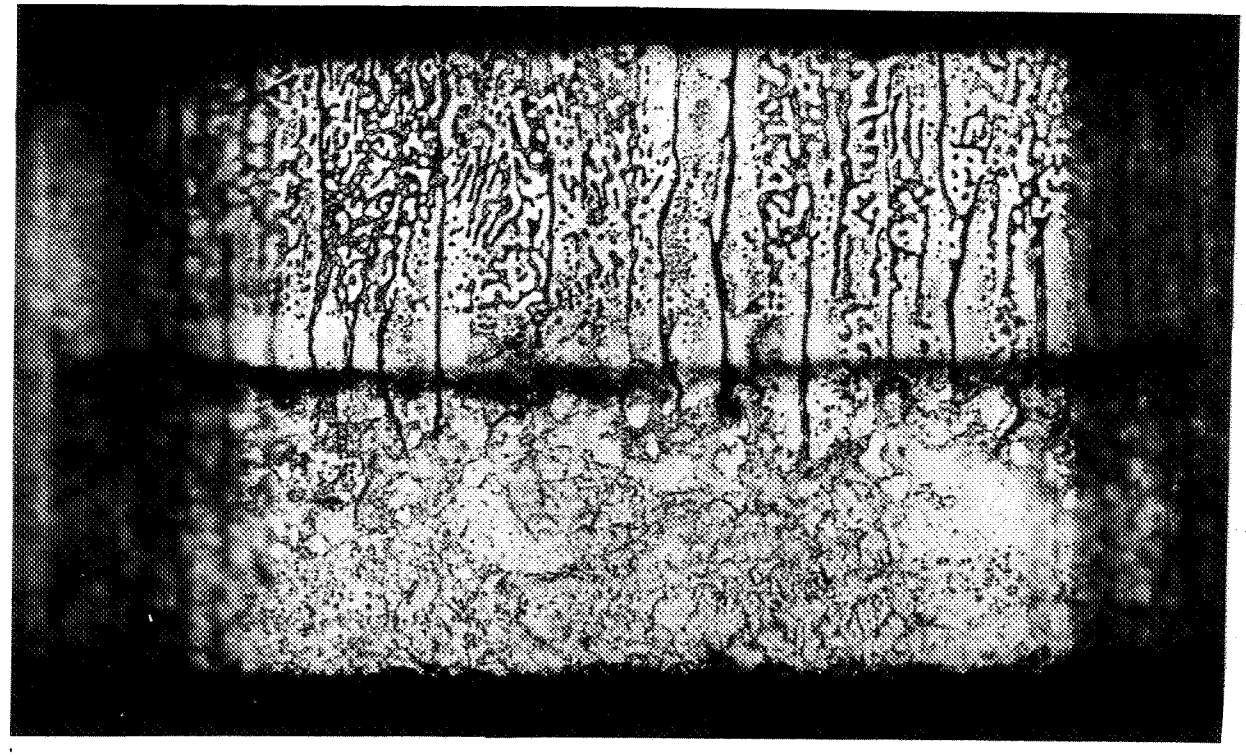

Photograph 15 - Cell # 5

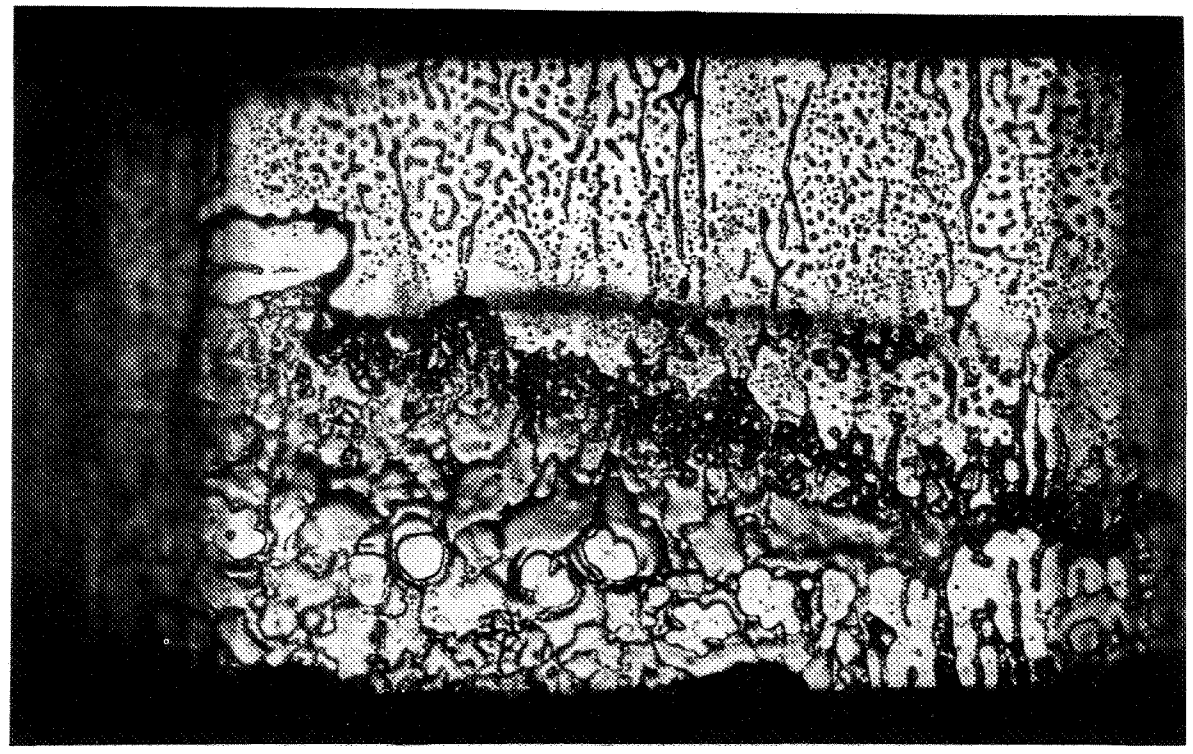

Photograph 16 - Cell # 6

The overall distribution of particles in the six cells is illustrated in Figure 4 where the black dots represent the approximate location of the particles. Cell # 7 is the cell which was photographed. It was oriented parallel to the base plate of the apparatus; the others were oriented perpendicular to the base plate. The particles are mostly on the "left" face of the cell in the illustration; the only exception is Cell # 4 whose interface was tilted at 60° with the "left" side higher than the "right".

In summary, six sample cells survived the launch and re-entry, and functioned properly according to the telemetry. Cell # 7, which was photographed during the flight, cracked prior to the initiation of the photograph allowing the camphor to escape by vaporization and producing a vapor-liquid interface with its associated Marangoni convection. The six good cells were photographed and closely examined after recovery. The particles were no longer dispersed through the upper halves of the sample cells (which had been melted). Rather, the particles had fallen into pile-ups at the boundaries between the virgin samples and the portions which had been melted.

In attempting to understand the post-flight distributions of particles seen in the six good cells, the first question to be answered is whether the conditions of microgravity which existed on the flight could exert sufficient force on the particles to cause them to fall out of their initial state of dispersion. The terminal velocity, V_t, at which a particle falls can be calculated from Stoke's Law:

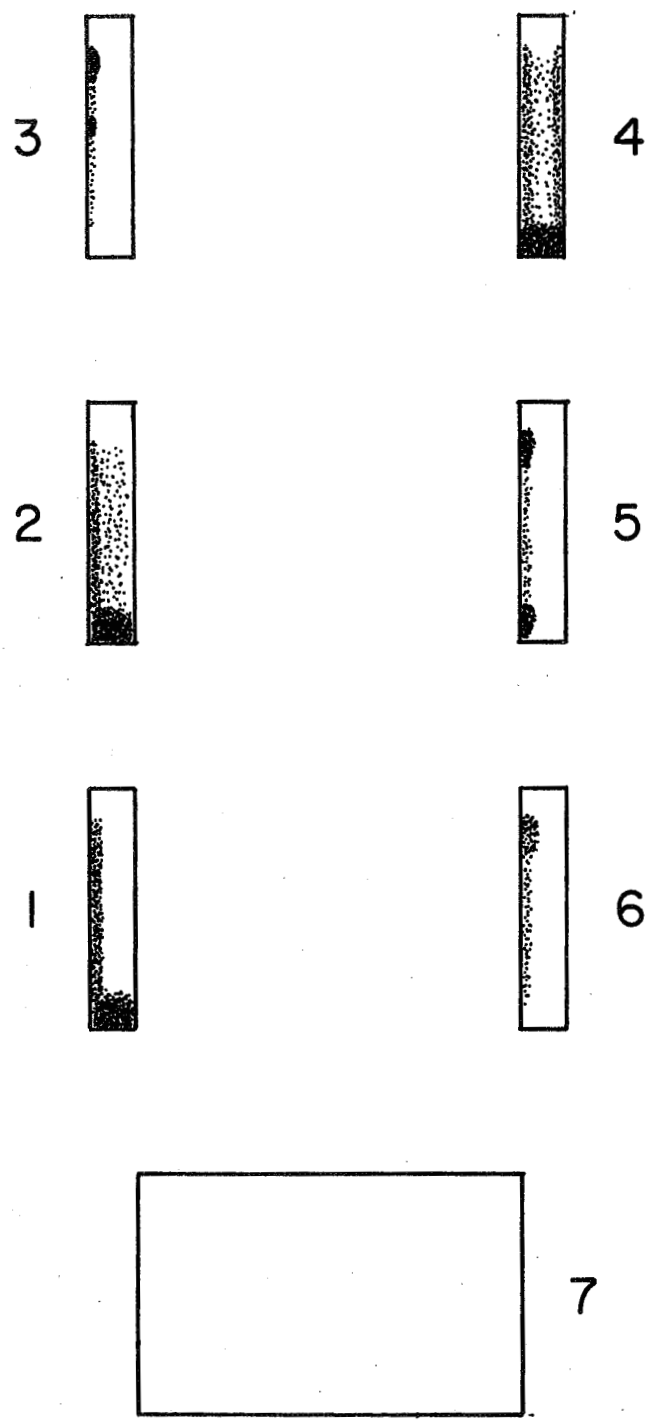

Figure 4 - Particle distribution in the cells flown on SPAR 4 as viewed from the top of the experiment package.

$$V_t = \frac{1}{18} \frac{\Delta\rho \; g \; d^2}{\eta}$$

where $\Delta\rho$ is the density difference between the particle and the liquid, g is the acceleration of gravity, d is the particle diameter, and η is the viscosity. For a 10μm diameter nickel particle in camphor, the calculated terminal velocity at 1g would be 8.6×10^{-2} cm sec^{-1}; at 10^{-2} g, the terminal velocity would be 8.6×10^{-4} cm sec^{-1}; and at 10^{-4} g, a terminal velocity of 8.6×10^{-6} cm sec^{-1} is expected. The telemetry from the flight indicates that a 10^{-4} g level was reached within a few seconds of the time that the sample started to melt (within 10 seconds after the melt sequence was started). Hence during the entire 240 seconds of the experiment, the nickel spheres should fall some 10-50μm, not one or two millimeters as indicated by the observations. The smaller nickel spheres and the glass spheres would fall even less. Therefore the residual microgravity levels could not have caused the distribution of particles observed in the recovered samples.

If the observed distribution of particles did not occur before launch or during the flight, the question naturally arises whether the apparatus could have been recycled on the ground after the flight, and whether the distribution of particles is consistent with remelting and resolidification having taken place on the ground.

First, let us compare the distribution of particles in the cells with the orientation of the rocket when it was resting on the ground

after impact. The recovery team stated that the rocket was resting on a slope at an angle of about 30° to 45° to the horizontal, with the front of the rocket higher than the rear. The zero degree (i.e., north) designation on the 74/15 experiment package was pointing about 140° from a vertical plane through the payload rotated counter clockwise as viewed from the rear of the rocket looking foreward. Stated another way, the zero degree mark was pointing about 30°-45° clockwise from directly downward.

If the experiment recycled while the payload was resting at this angle, how would the particles in the molten samples be distributed? Referring back to Figure 4, the particles would be expected to fall out of their dispersion to land on the lower (left) face of the cell. In addition, the number of particles at the edge of the cell closest to Cell # 7 would be greater than the number at the other edge. However, all the particles would not fall to that edge, because most of the particles after falling a short distance would come to rest against the face of the cell and slide or roll down the face of the cell. The particles would not be able to slide or roll all the way to the lowest edge. Instead one would expect to find a pile-up of particles across nearly the whole width of the cell clustered against the lower (left) face of the cell. On this basis, it is concluded that the actual distribution of particles in the recovered samples from SPAR 4, shown in Figure 4 , matches the distribution of particles expected if the apparatus was recycled while resting on the ground after impact.

Telemetry data is not available to confirm whether the apparatus recycled after impact. Because of a failure of the power relay on SPAR 4, power to 74/15 apparatus was available following impact on the ground. However, the on-board timer in 74/15 would have had to reset itself to initiate the recycle of the experiment. As yet, we have been unable to identify the mechanism by which the timer was reset. It was originally thought that the timer reset occurred because of chatter in the power relays upon impact. To explore this possibility, Vaugh Yost at MSFC had the relays tested to shock levels at 1300 g's. Under those conditions, the relays chattered for only 5-10 milliseconds. For comparison, the 74/15 timer would require that relay chattered for about 100 milliseconds to reset the timer. Another possibility to explain the resetting of the timer is that an intermittent failure in the timer itself occurred on landing because of the very high shock levels encountered. Without a record of the shock spectrum encountered, and in light of the fact that failure of the main power relay did not occur on previous SPAR flights and is not expected to occur on future flights, it has not seemed worthwhile to attempt to reproduce a possible timer failure.

In brief, it is concluded that experiment 74/15 was repeated on the ground after the SPAR 4 flight, and that the distributions of particles seen in the recovered cells reflect solidification under conditions of the earth's gravity.

V. CONCLUSIONS FROM THE SPAR 4 EXPERIMENT

On the basis of the results of the SPAR 4 experiment, we conclude that the experiment should be reflown without change in concept or payload apparatus. The method of fabrication, quality control and preflight testing of the quartz cells must, however, be modified to reduce the risk of a cell failure on the next flight. An increased proof testing pressure coupled with more stringent vibration testing should identify any weak cells which might not survive the flight; and a change in the fabrication procedure to enlarge the fused area of sealing of the cells should decrease the likelihood of adventitious stress concentrators which can produce fracture of the cells.

We are confident that another flight of the 74/15 experiment will yield the desired data on the rejection and incorporation of second-phase particles at a solidification front without the complicating effects of gravity.

REFERENCES

1. A. E. Corte: J. Geophys. Res. 67 (1962) 1085.
2. D. R. Uhlmann, B. Chalmers and K. A. Jackson: J. Appl. Phys. 35 (1964) 2896.
3. G. F. Bolling and J. Cisse: J. Crystal Growth 10 (1971) 56, 67.
4. A. W. Neumann, C. J. Van Oss and J. Szekely: Kolloid Z.u.Z. Polym. 251 (1973) 415.
5. V. H. S. Kuo and W. R. Wilcox: I & EC Process Design and Develop. 12 (1973) 376.
6. E. M. Lifshitz: Soviet Phys. - Theoretical Physics (JETP) 2 (1956) 73.
7. A. W. Neumann: Adv. Colloid and Interface Sci. 4 (1974) 105.
8. K. A. Jackson: in H. Reiss, ed., Progress in Solid State Chemistry, Vol. 4 (Pergamon Press, New York, 1967).
9. J. D. Hunt and K. A. Jackson: Acta Met. 13 (1965) 1212.

CHAPTER III

Grumman Research Department Memorandum RM-645

FLIGHT IV TECHNICAL REPORT FOR EXPERIMENT 74-37 CONTAINED POLYCRYSTALLINE SOLIDIFICATION IN LOW-G

by

John M. Papazian

Materials and Structural Mechanics

Martin Kesselman

Research Technical Support and Operations

and

Theodoulos Z. Kattamis*

Postflight Technical Report, Contract NAS 8-31530

December 1977

*Institute of Materials Science, University of Connecticut, Storrs, Connecticut

Approved by: Richard A. Scheuing
Director of Research

ABSTRACT

Experiments were performed to study the effect of a low-gravity environment on the columnar-to-equiaxed transition (CET) during polycrystalline solidification. Solutions of H_2O-30 wt % NH_4Cl and H_2O-37 wt % NH_4Cl were solidified in semicylindrical molds with radial heat extraction. In the ground base tests the general heat flow direction was parallel or anti-parallel to gravity. Both solutions were quenched from the same soak temperature (90°C); the respective superheat temperatures were, therefore, approximately 57 and 23°C. The lower superheat resulted in a completely columnar structure, and the higher superheat resulted in a 1/3 columnar - 2/3 equiaxed microstructure; these results were independent of the relationship between heat flow direction and gravity. Grain multiplication mechanisms observed were showering, thermal inversion driven convection cells, and compositionally induced density inversion driven convection cells.

Results obtained during the SPAR IV flight established the viability of the novel freon quenching system designed for this apparatus, but a partial blockage in the needle valve of the quenching system prevented solidification of the samples. Thus no data on the effect of gravity on the CET were obtained. Incomplete preflight melting of the NH_4Cl was also observed. It was established that slow solidification, a long waiting time at room temperature, and the presence of agitation during this time coarsened the room temperature structure of the solid and lengthened the time required for remelting. These observations have led to apparatus modification and revision of prelaunch procedures to prevent a future occurrence of the same problem.

TABLE OF CONTENTS

LIST OF ILLUSTRATIONS

1. INTRODUCTION

The primary objective of experiment 74-37 is to study the effect of reduced gravity on the columnar-to-equiaxed transition (CET) in small castings (Ref. 1). The results obtained to date from SPAR I show the occurrence of an equiaxed microstructure in low gravity, instead of the expected columnar microstructure (Ref. 2). Similary, fine grained equiaxed, rather than columnar, microstructures were observed in the Skylab metals melting experiment (Ref. 3). On the other hand, Johnston and Griner (Refs. 4 and 5) were able to show that no dendrite arm break-off occurred during low gravity solidification of NH_4Cl and obtained a completely columnar structure. These two results are not necessarily contradictory because CET is a complex phenomenon and gravity driven convection leading to dendrite arm breakoff is only one of the mechanisms that is responsible for the formation of the equiaxed zone. Crystal nuclei may already pre-exist in the liquid, especially following inoculation (Ref. 6) or "big bang" nucleation (Ref. 7). Also, other gravity driven mechanisms may be responsible for transport of small crystals toward the central region of a casting (Ref. 8). A gravity independent mechanism for nucleation of the equiaxed zone has also been proposed (Ref. 9). Regardless of nucleation, it has been recently emphasized (Refs. 10 and 11) that the presence of nuclei is a necessary but not sufficient condition for the occurrence of CET. The growth of equiaxed grains must halt the advance of the columnar interface. This has been suggested to occur by attachment of equiaxed crystals to the columnar growth front (Ref. 10) or by the existence of thermal conditions favoring the growth of equiaxed rather than columnar grains (Ref. 12). This last suggestion, which has received some experimental

confirmation (Ref. 11), may be particularly germane to the low gravity environment since rough estimates indicate that the predominant effect of reduced gravity on dendritic growth may be through modification of the thermal rather than solute boundary layer (Ref. 13).

It has been recently emphasized (Refs. 11 and 14) and it also follows from the above discussion that CET is not well understood. It depends on the geometry and thermal characteristics of the mold, heat transfer in the liquid and solid, superheat of the liquid, constitutional supercooling parameter, the presence of nucleation centers, and gravity driven fluid flow.

The SPAR IV flight of experiment 74-37 was performed in a simple apparatus using semicylindrical copper molds with transparent sides. Solutions of NH_4Cl in H_2O were selected as sample materials, because this system has been used successfully by others in previous experiments. The mold geometry was chosen to simulate weld bead solidification and to provide the simplification of radial heat extraction. Four separate cells were available, but all of the cells shared the same thermal environment, i.e., soak temperature and cooling rate. The adjustable parameters were solute concentration, inoculant concentration, soak temperature, and cooling rate. Values of these parameters selected for SPAR IV were such that the CET occurred at different locations in two of the cells, while the other two cells were redundant, i.e., identical to the first two. Thus, this flight experiment was expected to provide data on the effect of gravity on the CET for two conditions.

2. APPARATUS AND EXPERIMENTAL PROCEDURE

A dedicated apparatus was designed and constructed for this experiment. Figure 1 shows an overall view. The apparatus consists of five major components: 1) sample chamber, 2) electronics box that automatically operates the experiment and conditions the telemetry signals, 3) a 250 exposure motor-driven camera, 4) a freon reservoir designed to deliver liquid freon, and 5) is the supporting structure. A more detailed description of the apparatus is given in Ref. 15. Figure 2 shows a close-up view of the sample chamber assembly. Four independent, semi-cylindrical pockets are contained between plexiglass faces. All of these chambers share the same thermal environment; that is, soak temperature and cooling rate. The cylindrical walls of the pockets and the central portion of the metallic block are machined from one piece of copper. The flat "top" walls of the sample pockets are made of stainless steel that is brazed to the copper. This is done in order to provide a slower cooling rate on the "top" of the sample which would better simulate weld bead solidification. Lighting for photographic purposes is provided by small lamps at the top of each cell, and slots are machined in the stainless steel to admit the light. One of the sample pockets is instrumented with four thermistors (numbered 1-4) placed at equal intervals along the radius, and another pocket has a thermistor (no. 5) at the apex. Two additional thermistors (no. 6 and 7) are attached to the copper block on the "outside" of the cylindrical chill wall. Two heaters are attached to the copper block and two small pieces of stainless steel tubing direct liquid freon onto the web of the copper block at central locations. Not shown in Fig. 2 are fine ruled grids which were placed on the inside rear

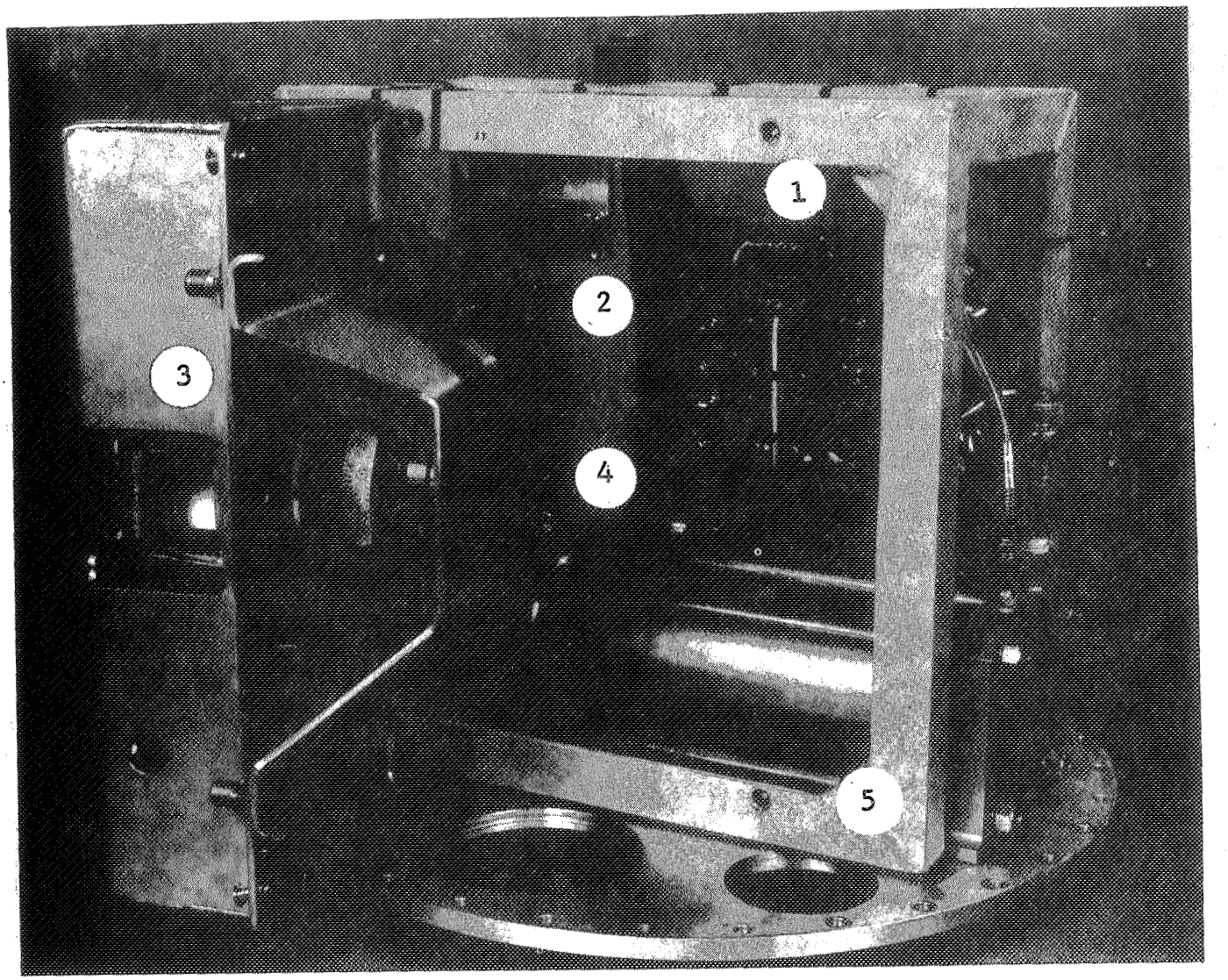

Fig. 1 Overall View of Apparatus 1) sample chamber, 2) electronics box, 3) motor-driven camera, 4) freon reservoir, 5) supporting structure

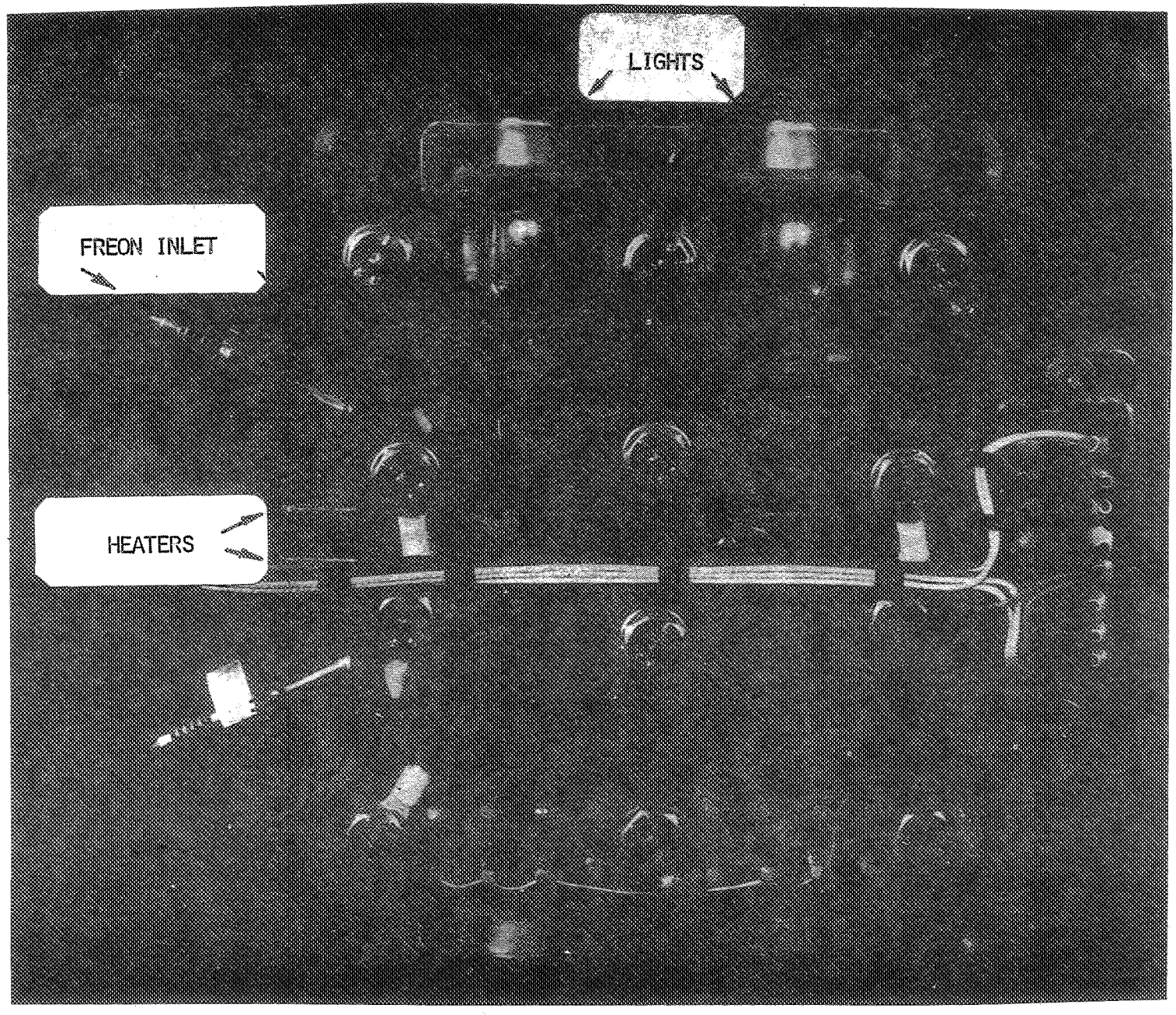

Fig. 2 Close-up View of Sample Chamber

wall of each pocket to allow simple Schlieren observation of convection.

In operation, the heaters were activated 45 minutes before lift-off and the entire sample chamber assembly was heated and controlled at 90°C. Upon lift-off the heater connection was severed. Approximately 30 seconds after attainment of low-g the freon quench was initiated and the camera started. The freon delivery rate was adjusted to give complete solidification of all four samples before the end of the film (220 exposures at approximately 1 frame/sec).

The samples were solutions of NH_4Cl in water. Compositions of 30 wt% and 37 wt% NH_4Cl - H_2O were chosen; their liquidus temperatures were 33 and 67°C, respectively. The solutions were made from laboratory purity NH_4Cl and filtered before use.

Laboratory simulations of the flight experiment were performed to generate one-gravity baseline data. The apparatus was installed in a vacuum bell jar which was equipped with electrical and fluid feed throughs, and the prelaunch and flight sequence was followed. The telemetered data were recorded on strip-chart recorders and the flight camera was allowed to operate automatically. Some tests were also performed using a 16 mm motion picture camera to record the progress of solidification.

3. GROUND BASE RESULTS AND DISCUSSION

The major results of the ground base experiments are included in a 16 mm motion picture film that has been submitted to the SPAR Program Office at NASA/MSFC. A copy of the film is available from the authors for loan to interested parties. The film illustrates visually the important effects of solute concentration and heat flow direction on cast microstructure. Figures 3, 4, 5, and 6 show selected frames taken during a typical ground base simulation; they show the progress of solidification in this experiment. The main results arranged in a chronological sequence from the beginning to end of the experiment, are summarized as follows:

1. Before nucleation occurs, thermal inversion, i.e., cold liquid above hot liquid, causes vigorous convection in the lower cells, Fig. 3, cell IV. This is due to a decrease in density of the solution with increasing temperature. This convection is damped soon after the solid starts growing along the chill, presumably because the release of latent heat of fusion decreases substantially the temperature difference between cell top and bottom.

2. Thermal inversion-induced convection is responsible for some grain multiplication, as illustrated in Fig. 4, cell III.

3. Grain "showering" is illustrated in Fig. 4, cells III and IV and in Fig. 5, cells I and III.

4. Convection cell formation and grain multiplication through compositionally induced density inversion is observed in Fig. 4, cell I. During columnar solidification there is rejection of water between the dendrites, making the interdendritic

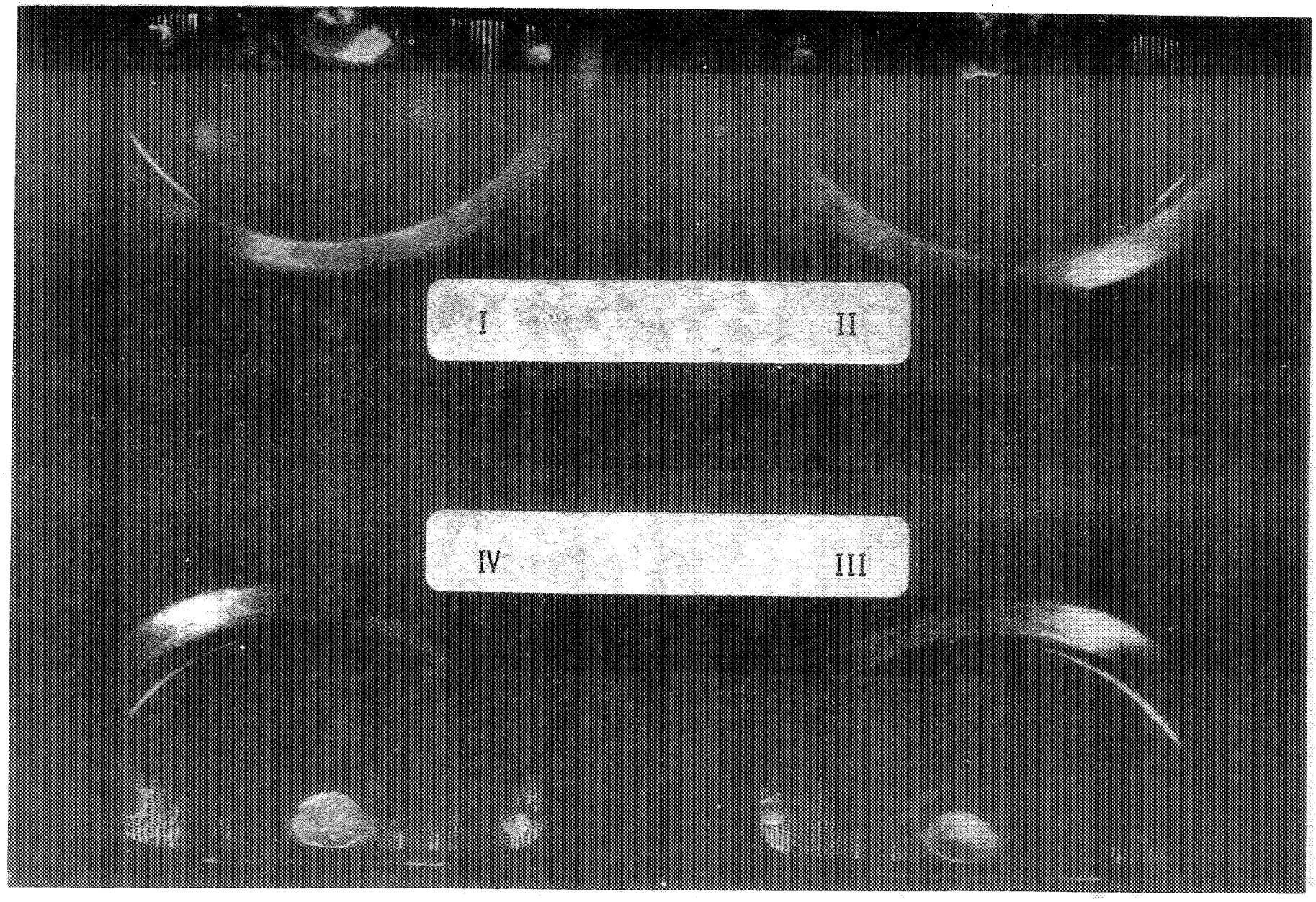

Fig. 3 Ground Base Simulation, 150s After Lift-Off

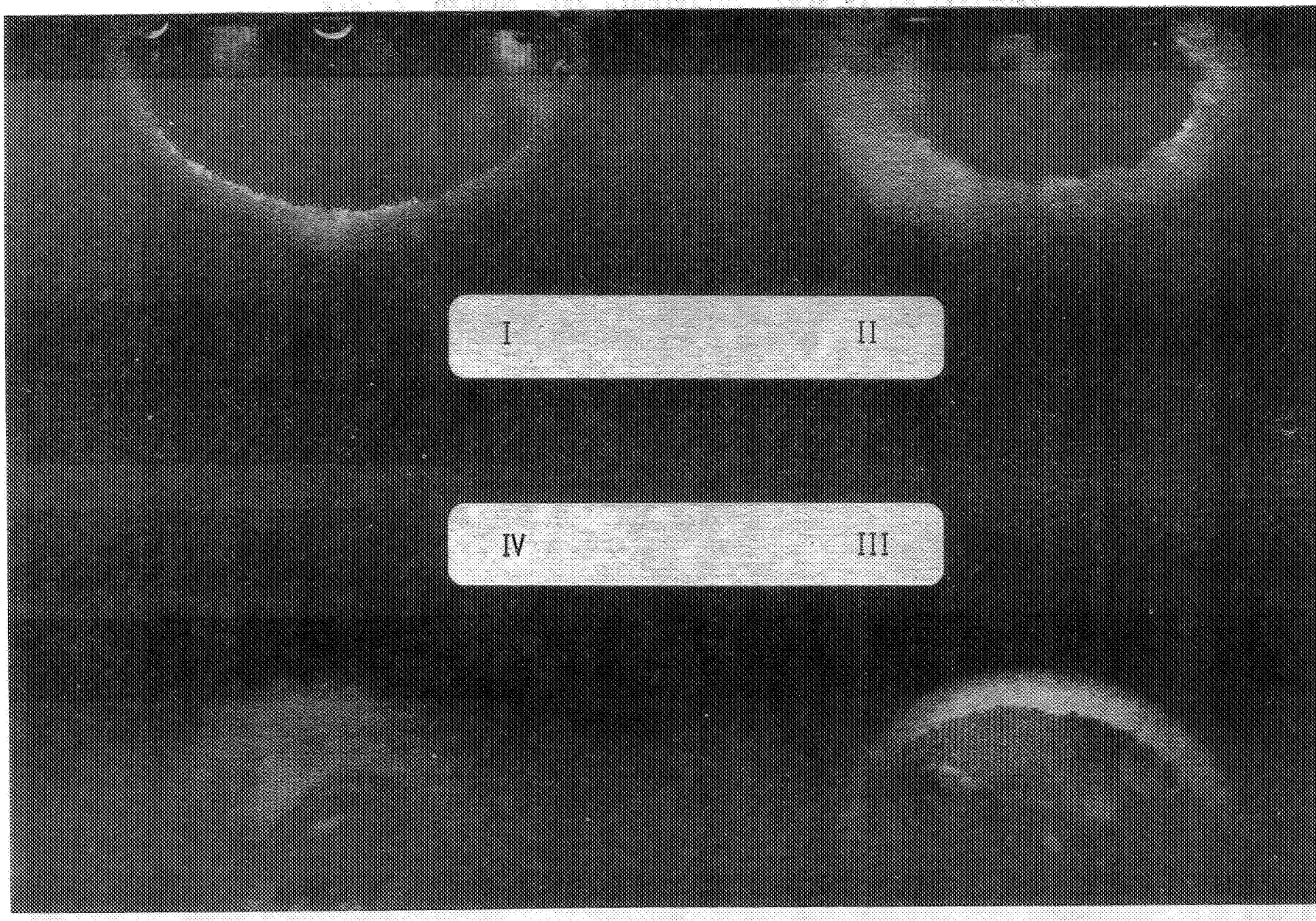

Fig. 4 Ground Base Simulation, 243s After Lift-Off

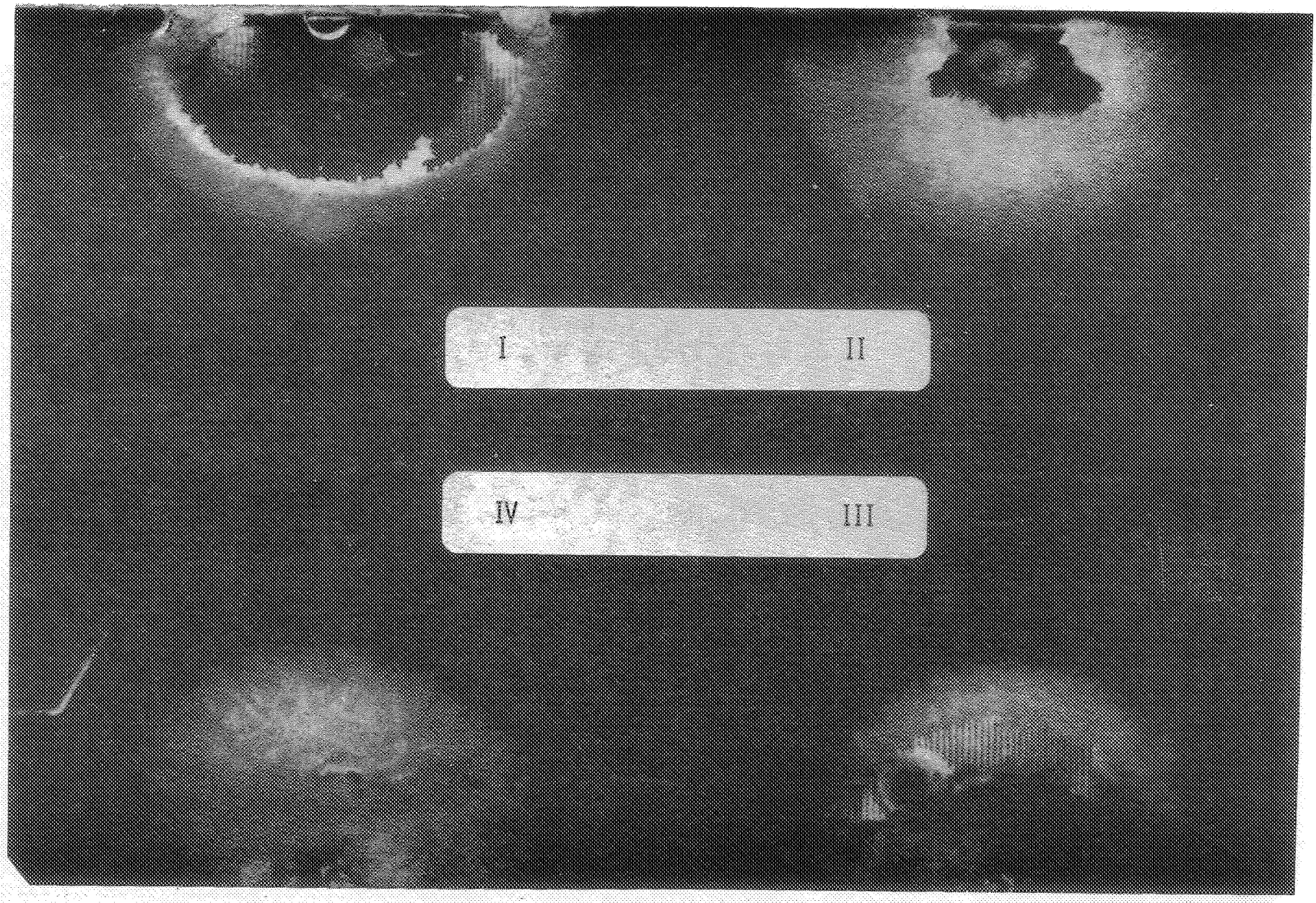

Fig. 5 Ground Base Simulation, 283s After Lift-Off

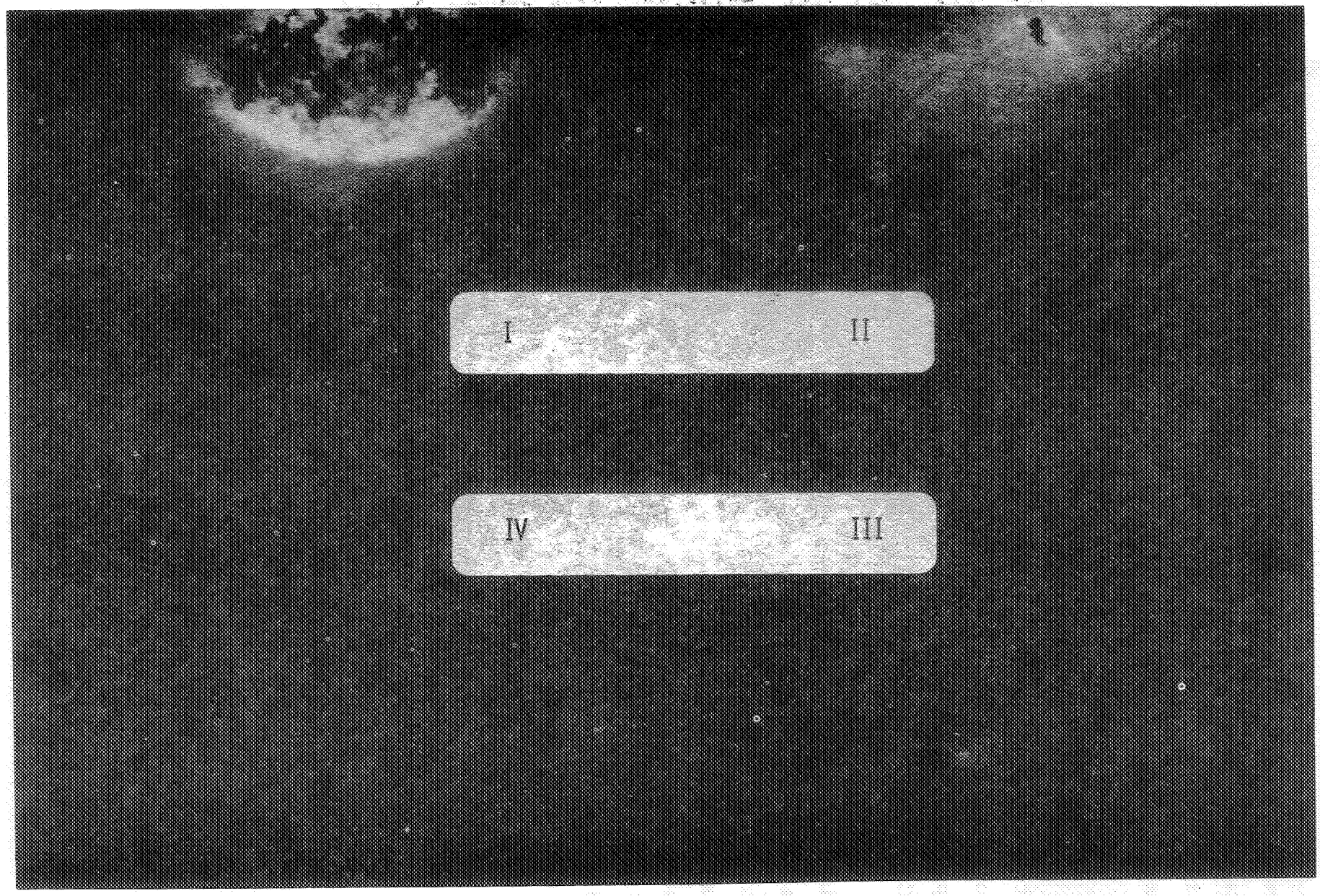

Fig. 6 Ground Base Simulation, 314s After Lift-Off

liquid less dense than the original solution. The rising interdendritic liquid accelerates dendrite arm remelting and coarsening and generates solid fragments which grow into a new generation of grains (Ref. 16).

5. The amount of liquid superheat prior to solidification has a significant effect on ingot microstructure. At a superheat of 23°C, which corresponds to a H_2O - 37% NH_4Cl alloy, a columnar structure was obtained regardless of chill location (top or bottom), Fig. 6, cells II and IV. At a superheat of 57°C, which corresponds to a H_2O - 30% NH_4Cl alloy, the structure was columnar along the first 1/3 of the mold cavity radius and equiaxed along the remaining 2/3, again regardless of chill location, Fig. 6, cells I and III. These results are consistent with observations of CET transitions in large ingots, in which columnar microstructures are observed during the initial stages of solidification in the high temperature gradient zones and equiaxed microstructures are observed later in lower temperature gradient zones. Different results can be obtained when nucleation rather than growth is the controlling step.

4. FLIGHT RESULTS AND DISCUSSION

The experiment was performed on SPAR IV. Inspection of the telemetered thermal data showed that the chill block failed to cool adequately (Fig. 7). Examination of the flight film showed that no solidification occurred during the entire length of the film, and that unmelted solid was present throughout the experiment (Fig. 8). These two problems are discussed below.

ABSENCE OF SOLIDIFICATION

The telemetered data were carefully analyzed. We find that for an interval of approximately twenty seconds between 300 and 320s the sample holder was cooled at a rate of about $0.9^{o}C/s$, which is the same cooling rate as our preflight ground base simulation (see Fig. 7). Thus, the freon system was capable of cooling at the desired rate even in the absence of gravity. Unfortunately, this cooling rate occurred only for a short interval, rather than for the full 200s. The fact that the proper cooling rate is achievable in zero gravity is, therefore, established and the cause of lack of cooling must be related to freon delivery, not low gravity effects.

A ground based test was performed on the apparatus as received immediately after the flight. The freon supply cylinder was removed from the system, and a supply of freon 12 connected in its place. The complete warm-up and launch sequence was followed and the major temperatures monitored. The test revealed that the system was still blocked. The sample holder was then removed to eliminate it as the source of blockage. The test was performed again and the blockage remained. This procedure isolated the blockage in the solenoid valve-needle valve combination.

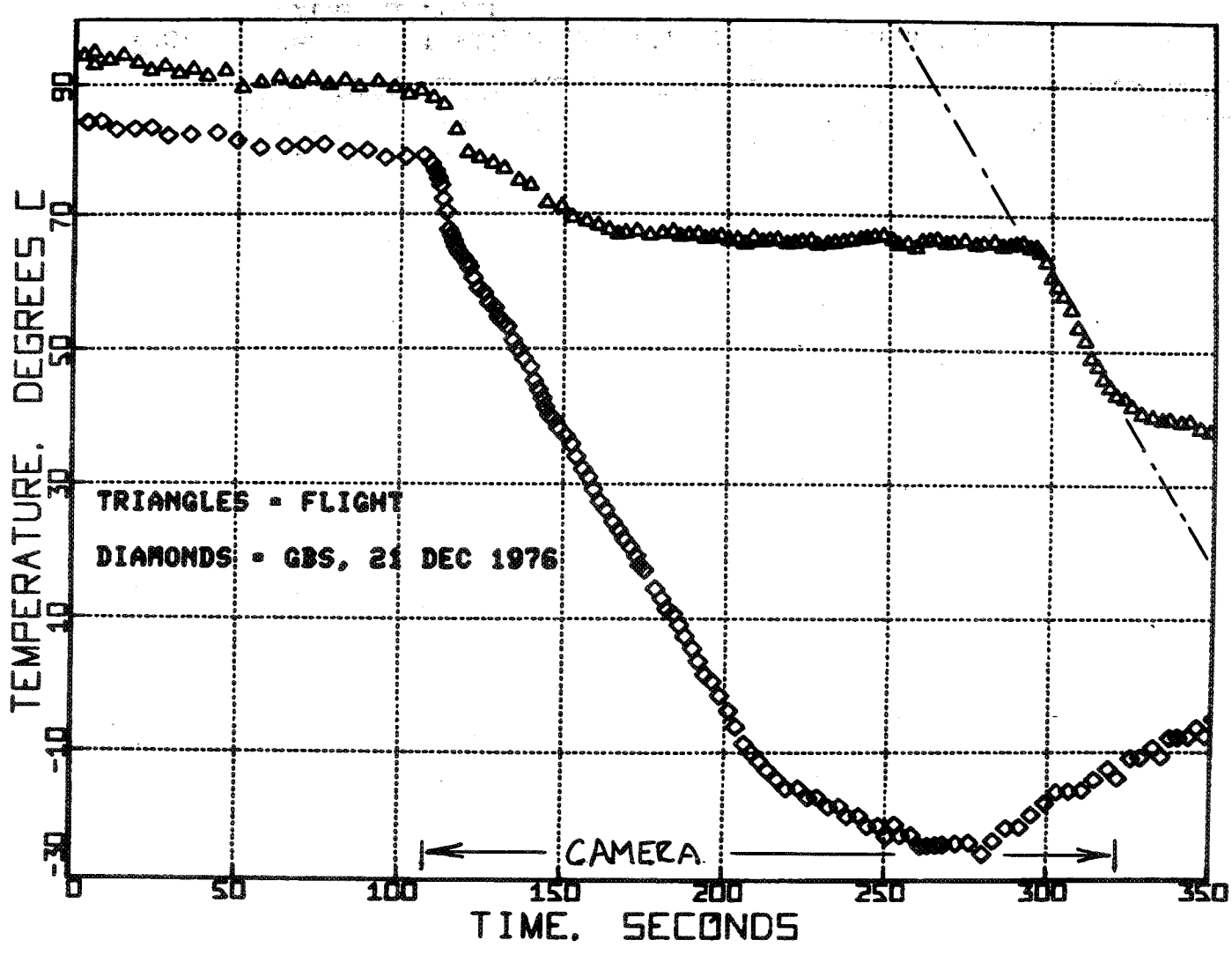

Fig. 7 Thermal History of Flight Experiment and Ground Base Simulation

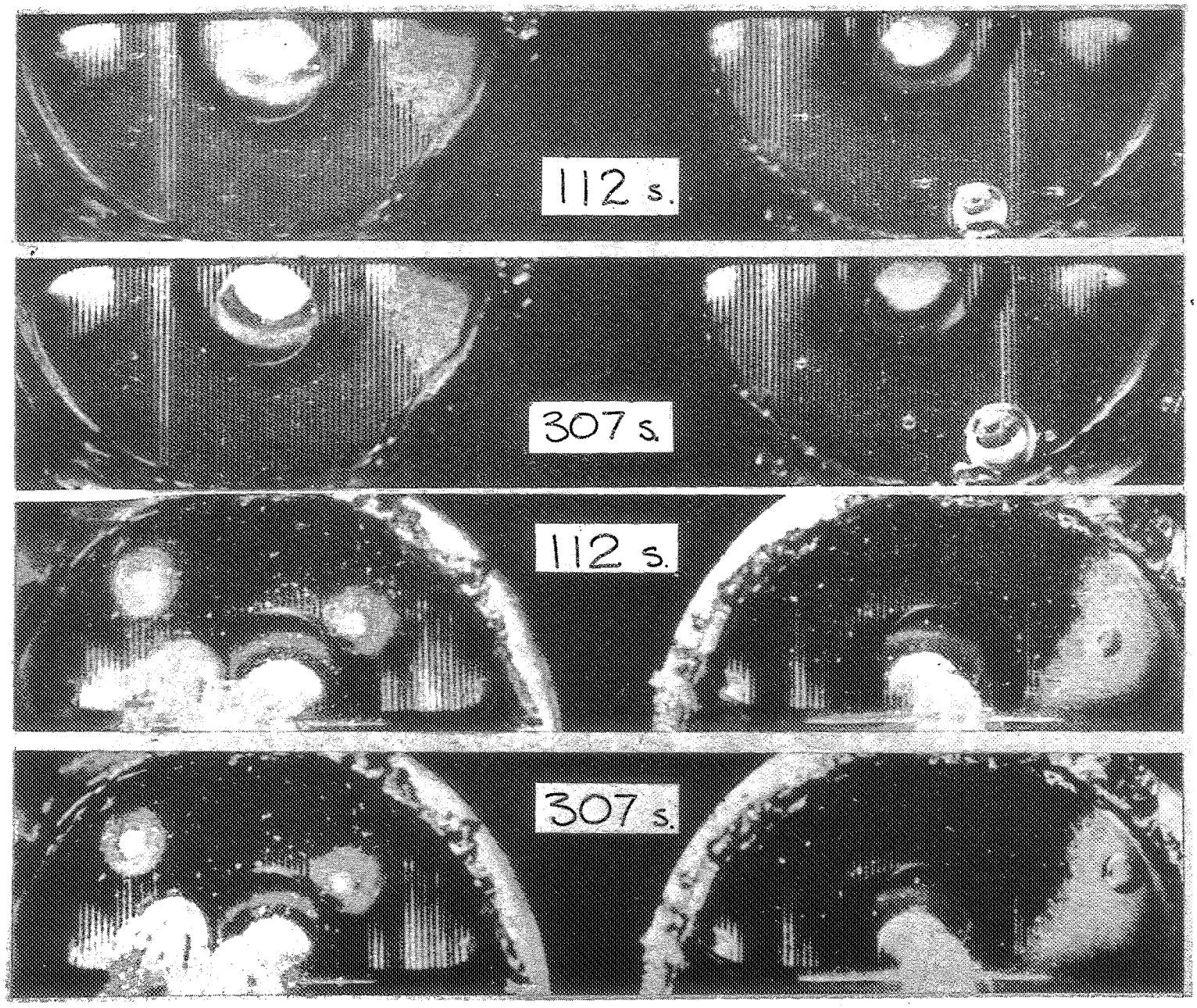

Fig. 8 Results of Flight Experiment at 112s and 307s After Lift-Off

Careful disassembly of each of these valves resulted in the following observations and conclusions:

There were no foreign objects in the solenoid valve, therefore, this unit did not clog

The following foreign objects were found in the needle valve:

- A small black particle about 2 mils in diameter, from the O-ring in the freon bottle
- Shredded material, thread-like, either teflon sealing tape or from the Kel-F seat seal
- A grease, completely surrounding the tip of the needle, suspected to be silicone O-ring lubricant used in the freon bottle

Either the grease or the thread-like material could have clogged the needle valve and reduced the flow rate to an inadequate level, but the combination of the two is thought to provide a potent source of blockage.

Based on these findings, it is concluded that the absence of solidification during the flight experiment was due to a blockage in the freon delivery system. Subsequently, modifications have been made to the apparatus to prevent a future occurrence of this problem.

INCOMPLETE MELTING

To elucidate the reasons for incomplete melting (dissolution) a series of experiments were conducted using the flight apparatus specimen holder. These experiments and the results obtained are summarized in the table on the following page. The three process variables investigated were: original solidification rate, waiting time at room temperature prior to remelting, and

agitation during this time. All experiments were performed in the absence of agitation during the remelting stage.

Experiment Number	Solidification Rate	Waiting Time (days)	Agitation	Time Required for Complete Melting (min)
3	Quench	0	No	11
7	Quench	0	Yes	35
1	Quench	3	Yes	>90
10	Quench	1	No	>90
5	Slow Cool	1	No	>90
11	Slow Cool	0	No	22

From these results it appears that slow solidification, a long waiting time, and the presence of agitation contribute to a longer time being required for complete remelting. Comparison of experiments nos. 3 and 11 shows that a low solidification rate can double the remelting time. Comparison of experiments nos. 3 and 7 shows that the presence of simple agitation at room temperature has an even greater effect on remelt time. Furthermore, comparison of experiments nos. 3, 7, 11, and 1, 10, 5 shows that the effect of waiting time at room temperature is the most important of the three process variables.

To explain these results it is necessary to observe that at room temperature the system is above the eutectic temperature and is part liquid, part solid. It consists of primary dendrites of pure NH_4Cl surrounded by a liquid containing about 27 wt% NH_4Cl. During reheating, a dissolution of NH_4Cl occurs at the surface of dendrite arms or solid particles, enriching the surrounding liquid in NH_4Cl. The dissolution process depends on the surface to volume ratio of the solid, therefore, the time required for

complete dissolution depends on the dendrite arm or solid particle radius. A rapid initial solidification rate would refine the primary NH_4Cl dendrites and hence would reduce the time required for complete dissolution or remelting. Also, because solid is in contact with liquid at room temperature, Ostwald ripening or diffusional coarsening of the solid would occur during long waiting times. Thus, dendrite arms or solid particles would become coarser, hence a longer time would be required for their remelting. Finally, agitation of a solid-liquid mixture at room temperature accelerates diffusional coarsening by enhancing transport of NH_4Cl through the liquid and causes collisional coalescence of various dendritic or nondendritic particles. Again, this would contribute to coarsening dendrite arms or solid particles and would, therefore, lengthen the time required for complete remelting. As a result of this analysis a revised prelaunch procedure can be developed to assure complete dissolution of NH_4Cl particles before lift-off.

5. REFERENCES

1. Papazian, J.M. and Kattamis, T.A., "Technical Proposal for contained Polycrystalline Solidification in Low Gravity," Grumman Research Department RP-546, File No. 74-128 NAS, February 1975.

2. Papazian, J.M., and Kattamis, T.Z., "Contained Polycrystalline Solidification in Low Gravity," Flight I Technical Report NASA TM X-3458, p. VIII-1, (1976).

3. McKannan, E.C., "M551 Metals Melting," Proceedings Third Space Processing Symposium, Skylab Results, p. 85, M-74-5 Marshall Space Flight Center, Alabama, June 1974.

4. Johnston, M.H. and Griner, C.S., " The Direct Observation of Solidification as a Function of Gravity Level," NASA TM X-3458, p. V-1, (1976).

5. Johnston, M.H. and Griner, C.S., "The Direct Observation of Solidification as a Function of Gravity Level," Met. Trans. 8A, 77 (1977).

6. Cole, G.S., Casey, K.W., and Bolling, G.F., "A Practical Method for Identifying Inoculants," Met. Trans. 5, 407, (1974).

7. Jackson, K.A., Hunt, J.D., Uhlman, D.R., and Seward, T.P., "On the Origin of the Equiaxed Zone in Castings," Trans. TMS-AIME 236, 149 (1966).

8. Southin, R.T., "Nucleation of the Equiaxed Zone in Cast Metals," Trans. TMS-AIME 239, 220 (1967).

9. Winegard, W.C. and Chalmers, B., "Supercooling and Dendritic Freezing in Alloys," Trans. ASM 46, 214 (1954).

10. Fredriksson, H. and Hillert, M., "On the Formation of the Central Equiaxed Zone in Ingots," Met. Trans. 3, 565 (1972).

11. Doherty, R.D., Cooper, P.D., Bradbury, M.H., and Honey, F. J., "On the Columnar to Equiaxed Transition in Small Ignots," Met. Trans. 8A, 397 (1977).

12. Burden, M.H. and Hunt, J.D., "A Mechanism for the Columnar to Equiaxed Transition in Castings or Ingots," Met. Trans. 6A, 240 (1975).

13. Fredriksson, H., "Possible Dendrite Growth and Segregation Phenomena During Solidification of Alloys in Space," ESA Special Publication No. 114.

14. Weinberg, F., "The Casting of Steel", Met. Trans. 6A, 1971 (1975).

15. Kesselman, M. and Papazian, J.M., "Experiment Implementation and Requirements Plan for Sounding Rocket Experiment 74-37-2," Grumman Aerospace Corporation, Bethpage, N.Y. 11714. Submitted to NASA, Marshall Space Flight Center, Alabama 35812.

16. Strangman, T.E. and Kattamis, T.Z., "Crystal Multiplication in Undercooled NH_4Cl-H_2O Solutions," J. Crystal Growth 18, 209 (1973).

CHAPTER IV

PREPARATION OF AMORPHOUS FERROMAGNETIC MATERIALS THROUGH CONTAINERLESS SOLIDIFICATION

Contract No. NAS8-31972

January 27, 1978

Prepared for

National Aeronautics and Space Administration
George C. Marshall Space Flight Center
Huntsville, Alabama 35812

Prepared by

Dr. A. E. Lord, Jr.
Principal Investigator
Drexel University

Mr. Gerald Wouch
Associate Investigator
General Electric Company

Dr. R. T. Frost
Program Manager
General Electric Company

GENERAL ELECTRIC COMPANY
Space Sciences Laboratory
P.O. Box 8555
Philadelphia, Pa. 19101

Abstract

Reported herein is the ground based research, the work in preparation for the flight experiment, the results of the flight experiment, and the failure analysis for Experiment 74-49, "Preparation of Amorphous Ferromagnetic Materials through Containerless Solidification."

The experiment was flown on the NASA SPAR IV sounding rocket in the Electromagnetic Containerless Processing Payload. Due to a failure to melt, the experiment hypothesis was not tested on this flight.

1.0 INTRODUCTION AND SUMMARY

The first strongly ferromagnetic metallic glass was reported in 1967[1]. It was the alloy $Fe_{83}P_{10}C_7$. The preparation and characterization of many other ferromagnetic metallic glasses has since been described[2, 3, 4]. These generally have a chemical composition of the form $(T'_{1-x}T''_x)_{80}(M'_{1-x}M''_x)_{20}$, where T' and T'' are metals such as Ni, Co, Fe, Pd, Cu and M' and M'' are metalloids such as Si, C, P or B. Typical of this form is the ferromagnetic metallic glass having the composition $Fe_{40}Ni_{40}P_{14}B_6$ (Allied Chemical's METGLAS 2826). The amorphous metallic alloys (metallic glasses) were first prepared by SPLAT cooling[5], then by roller quenching[6], and finally (for a few selected compositions) by quenching in water[7]. The first two methods require very high quenching rates (10^4 to 10^6 °C/sec). The last method utilizes modest quenching rates (10^2 to 10^3 °C/sec).

In light of the above considerations, it was hypothesized that it might be possible to prepare ferromagnetic metallic glasses by containerless cooling at slower cooling rates yet ($< 10^2$ °C/sec), due to elimination of nucleation sites present with container walls. Experiment 78-49 was to test this hypothesis by melting a specimen of METGLAS 2826 composition in the NASA Electromagnetic Containerless Processing Payload (ECPP) during the NASA SPAR IV sounding rocket flight and allowing it to cool while levitated. Due to a failure to melt the specimens, for reasons discussed below, the experiment was not performed and the hypothesis was not tested on this flight.

Ferromagnetic metallic glasses (amorphous ferromagnetic alloys) are "soft" magnetically. They can be magnetized very easily due to low coercive force and high permeability. They also share with other non-ferromagnetic metallic glasses the properties of high strength and hardness. These desired

properties arise from the lack of gross crystallinity and homogeneous structure, both effects, for example, allowing domain walls to move easily. These materials are, hence, interesting from both a scientific and technological viewpoint.

The objectives of the sounding rocket experiment were: (1) to obtain a large amount of supercooling of a containerless melt of composition $Fe_{40}Ni_{40}P_{14}B_6$ (in atomic percent); (2) to prepare a bulk specimen of the ferromagnetic glass of this composition by supercooling to the glass temperature, Tg, thus bypassing crystallization. An alternative objective, in case (1) was achieved but not (2) was: (3) to examine the crystallization of a (possibly) highly supercooled, containerless melt of this composition.

The choice of the METGLAS 2826 composition was made for the following reasons: (1) examination of the many candidate compositions indicated that the prospects for success were good, because of the high reduced glass temperature (ratio of glass transition temperature to melting temperature); (2) the ferromagnetic metallic glass produced by roller quenching in the form of a "tape" has been well characterized; it has not yet been prepared in bulk form, either by water quenching or any other technique.

As reported, the experiment was not performed due to a failure to melt the specimen. The work reported herein, then, consists of: (1) the ground based experiments; (2) the analysis of the ground based specimens; (3) the flight experiment; (4) failure to melt analysis; (5) recommendations and conclusions. The ground based experimental work yielded new results in terms of understanding the visco-elastic properties of these glasses and the variation of viscosity through the glass transition temperature from metallic glass to crystalline solid[6]. This last result is of importance in predicting what glasses can be produced at lower quench rates ($\sim 10^2$ °C/sec) and hence will be discussed further below in greater detail.

2.0 GROUND BASED EXPERIMENTS

2.1 SPECIMEN SELECTION

A survey was made of the known metallic glasses. The results of the survey are shown in Appendix A. Compositions selected for further investigation in our laboratory are shown in Table I. A very important parameter for successful production of a metallic glass is the reduced glass temperature. A reduced glass temperature above 0.5 was recommended (by Dr. David Turnbull of Harvard University, who consulted on this experiment with the Principal and Co-Investigators). METGLAS 2826 with a melting temperature of 1223°K (approximately) and a glass transition temperature of 693°K (approximately) has a reduced glass temperature of 0.57, satisfying the above criterion. Hence, along with the fact that it was the most studied ferromagnetic metallic glass, it was selected, for the above reason, as the flight composition.

2.2 SPECIMEN PREPARATION

Techniques for preparing specimens of selected compositions for ground based experiments were examined. These included: (1) melting the elemental powders; (2) vacuum hot pressing; (3) vacuum melting and casting using glass tapes as the starting material. This last technique was adopted for the preparation of ground based and flight specimens. Pieces of METGLAS 2826 glass tape were compacted in a crucible and vacuum melted to produce specimens approximagely 0.922 centimeters in diameter. The specimens produced were crystalline in nature. The objective was to melt these and by containerless cooling produce a bulk ferromagnetic glass specimen.

2.3 BREADBOARD EXPERIMENTS

Experiments were conducted in the Breadboard Facility with the following objectives: (1) to quantify the performance of the Breadboard and the Flight Unit; (2) to determine the specimen preparation procedures to be used in fabricating

Table I. Compositions Selected for Laboratory Investigations with Melting Points

Composition	T_ℓ (°C) ±20°	T_g
$Fe_{32}Ni_{36}Cr_{14}P_{12}B_6$ (2826A)	940*	paramagnetic at R. T.
$Fe_{78}Mo_2B_{20}$ (2605A)	885	420
$Fe_{29}Ni_{49}P_{14}B_6Si_2$ (2826B)	940*	
$Fe_{40}Ni_{40}P_{14}B_6$ (2826)	955	410
$Co_{72}Fe_3P_{16}B_6Al_3$	950	
$Ni_{60}Fe_{20}B_{20}$	940*	
$Fe_{70}Co_{10}B_{20}$	940*	
$Fe_{83}B_{17}$	1050*	

The starred values listed for melting points T_ℓ and glass temperature T_g were measured by the authors.

the flight specimen; (3) to specify the chamber preparation, specimen insertion, gas purification, and filling procedures for the flight experiment; (4) to conduct specimen melting studies. It was recognized at the outset that, whereas the Breadboard Facility was designed only for the purposes of testing the conceptual design of the ECPP, its performance would be different from that of the ECPP. The functional operation of the experiment could be tested in the Breadboard Facility, and, with the proper scaling ratios, estimates of the melting time of the specimens in the selected gaseous environments could be predicted for the flight experiment in the ECPP.

Breadboard calibration tests were performed in Argon, using the same #316 stainless steel as used in the flight unit (ECPP) tests, discussed below. A calibration factor between the performance of the breadboard and the ECPP with regard to heating was determined. This is discussed below in the failure analysis, where the experiment log summary is given.

Breadboard tests were conducted with specimens of the METGLAS 2826 composition, having an average diameter of 0.922 centimeter diameter. Heating and melting tests were conducted in 1 atmosphere Argon, 10 torr Argon, 1 atmosphere Helium, 10 torr helium, 800 torr of 50% He and 50% A mixture, 100 torr Helium.

Analysis of the data from these tests showed: (1) that the specimen would not cool in vacuo to 400^{o}C within the 200 seconds allotted for the experiment; (2) that the specimen would not melt in pure helium in the flight unit (using the calibration factor); (3) that the specimen would melt and cool within 200 seconds in a helium-argon mixture having the molar ratio 0.65 He to 0.35 argon. Accordingly this mixture was adopted for the flight experiment.

2.4 GROUND BASED EXPERIMENTS AT DREXEL UNIVERSITY

The research program at Drexel University, conducted by the Principal Investigator,* had these objectives: (1) the preparation of metallic glasses; (2) the characterization of their properties; (3) devising testing techniques to characterize the ground based and flight specimens (which are not tapes but bulk specimens, spheroidal in shape). Research was conducted in the following areas: (1) the effects of hydrostatic pressure on the magnetic properties of metallic glasses such as METGLAS 2826[5]; (2) the glass-crystalline phase transition and properties at the transition of such metallic glasses[6]; (3) acoustic emission generated during viscous flow of metallic glasses[7]. This work has great relevance in predicting what magnetic glasses can be produced in bulk form as proposed. In particular it was found[6] that the viscosity at the glass transition temperature (Tg) of METGLAS 2826 is about 10^8 poise, which is an order of magnitude lower than observed at the Tg for non-ferromagnetic metallic glasses[8, 9] such as $Pd_{77.5}Si_{16.5}Cu_{6.7}$. This indicates that an important factor is this viscosity as well as the reduced glass temperature. This finding came late in the research work and is new and unexpected. It may well be that both a high reduced glass temperature and a high transition viscosity are required to prepare a bulk specimen of ferromagnetic glass by the technique proposed. This will be considered before the following flights. During this work, the Pd Si Cu metallic glass mentioned above was routinely prepared in bulk form in the laboratory.

The following characterization techniques were established to investigate the properties of the ground based and flight specimens: (1) Magnetic Measurements. A vibrating reed magnetometer was constructed to characterize the magnetic properties of the specimens produced. It was tested with nickel and crystalline alloy prepared by crystallizing METGLAS 2826 tape. B-H curves through a closed magnetic loop were also obtained and the technique perfected for the

ground based and flight specimen geometries, also an induction method was developed for use with the long thin tapes and also for use in certain measurements of the bulk samples; (2) X-Ray Characterization. Back reflection and diffractometry were performed both at Drexel University and GE on METGLAS 2826 tape, crystalline tape, and the ground based specimens. This would have served as the comparison between the flight specimen produced and the glass tape produced terrestrially; (3) Differential Scanning Calorimetry. Phase transitions in METGLAS 2826 were investigated using differential scanning calorimetry. This technique again would have served as a comparison between the terrestrially produced tape and the flight specimen produced; (4) metallographic work was performed on the terrestrially produced tape, the ground based specimen, and the unmelted flight specimen (discussed below). This included electron probe microanalysis.

Preparation for examination of the flight specimen was completed prior to launch. The post flight analysis showed that the specimen had not melted, but was near the melting point. Hence the post flight examination could have no bearing on the experiment hypothesis.

2.5 FLIGHT EXPERIMENT

Analysis of the flight experiment data indicated that the specimen was not melted during the flight. The input power to the specimen was too low (see failure analysis below) and the specimen load was not matched properly to the r.f. tank circuit. Metallographic analysis confirmed this failure to melt. The specimen had reached a temperature near melting and incipient melting had begun on the surface but had not progressed inward during the experiment.

3.0 FAILURE TO MELT

A memo, appended to this report, was issued August 30, 1977, explaining the failure to melt the specimen during flight. Appended also to this report is a memo on the Ground Based Preparations for Experiment 74-49, which constitutes a summary of the log book records in preparation for the flight. There has been no change in the conclusions reached in the failure analysis presented since that time.

CONCLUSIONS

The testing of the hypothesis that bulk specimens of ferromagnetic metallic glasses may be produced by containerless cooling was not performed on the flight experiment 74-49. Further flights should utilize a quench gas (helium) introduced after melting to rapidly cool the levitated specimen. The test documentation should be improved to insure that the procedural error committed in final adjustment of the flight equipment is not repeated. Careful attention should be paid to the fabrication of the flight specimen as discussed in Appendix A. Testing of the performance of the flight unit (ECPP) should be conducted with a flight specimen rather than #316 stainless steel specimens.

References

1. P. Duwez and S. C. H. Lin, "Amorphous Ferromagnetic Phase in Ion-Carbon-Phosphorous Alloys," J. Appl. Phys. 38, 4096 (1967).

2. Chen, H.S., "Glass Temperature, Formation, and Stability of Fe, Co, Ni, Pd, and Pt Based Glasses," Mat. Sci. and Eng., 23, 151, (1976)

3. Gilman, J. J., "Metallic Glasses," Physics Today, May 1975.

4. P. Chaudhari and D. Turnbull, "Structure and Properties of Metallic Glasses," Science, 199, 4324, 6 Jan. 1978, pp. 11.

5. Lin, S. C. H. and Duwez, P., Phys. Status Solidi., 34, 469 (1969).

6. Liebermann, H. H. and Grahm, C. D., Jr., IEEE Trans. Magn., 12, 921 (1976).

7. Chen, H. S., "Thermodynamic Considerations on the Formation and Stability of Metallic Glasses," Acta. Met. 22, 1505 (1974).

8. A. E. Lord, Jr. and P. M. Anderson, III, "Acoustic Emissions Generated During Viscous Flow of Metallic Glasses," Letters in Appl. and Eng. Sci., Vol. 5, No. 5, pp. 335-339 (1977).

9. Anderson, P. M. III and Lord, A. E. Jr., "Demonstration of Phase Transition and Properties of Metallic Glasses for Undergraduates," Am. J. Phys., 45, 12, (1977), pp. 260.

APPENDIX A

RESULTS OF LITERATURE SEARCH ON GLASS FORMING COMPOSITIONS

Alloy	Tg (°C)	Ref.	Tx	Ref.	T_{ℓ}	Ref.
$Fe_{39.8}Ni_{40.6}P_{14}B_6$	404	1	412	1		
$Fe_{41.3}Ni_{40.4}P_{13.7}B_6$	408	1	418	1		
$Fe_{40.1}Ni_{39.1}P_{12.2}B_6$	404	1	417	1		
$Fe_{38.8}Ni_{38.1}P_{12.1}B_6$	408	1	418	1		
$Fe_{40.2}Ni_{38.2}P_{.5}B_{20}$	442	1	451	1		
$Fe_{51.8}Ni_{30.5}P_{14.7}B_6$	418	1	423	1		
$Fe_{50}Ni_{30}B_{20}$	444	1	455	1		
$Fe_{73}P_{18}B_6Al_3$	---	2	415	2		
$Fe_{75}P_{16}B_6Al_3$	---	2	427	2		
$Fe_{77}P_{14}B_6Al_3$	---		445	2		
$Fe_{79}P_{12}B_6Al_3$	450	2	445	2		
$Co_{73}P_{18}B_6Al_3$	---	2	479	2		
$Co_{75}P_{16}B_6Al_3$	---	2	399	2		
$Co_{77}P_{14}B_6Al_3$	---	2	381	2		
$Co_{79}P_{12}B_6Al_3$	---	2	392	2		
$(Co_{80}Fe_{20})_{75}P_{16}B_6Al_3$	470	2	477	2		
$(Co_{60}Fe_{40})_{75}$ " "	457	2	479	2		
$(Co_{40}Fe_{60})_{75}$ " "	456	2	472	2		
$(Co_{20}Fe_{80})_{75}$ " "	462	2	452	2		
$Fe_{75}P_{16}B_5Al_3$ " "	---		427	2		

Alloy	Tg	Ref.	Tx	Ref.	Tℓ	Ref.
$(Fe_{80}Ni_{20})_{75}P_{16}B_6Al_3$	---		427	2		
$(Fe_{60}Ni_{40})_{75}$ " "	439	2	437	2		
$(Fe_{40}Ni_{60})_{75}$ " "	420	2	437	2		
$(Fe_{20}Ni_{80})_{75}$ " "	414	2	435	2		
$Ni_{75}P_{16}B_6Al_3$	417	2	427	2		
$(Ni_{80}Co_{20})_{75}P_{16}B_6Al_3$	427	2	447	2		
$(Ni_{60}Co_{40})_{75}$ " "	---		425	2		
$(Ni_{40}Co_{60})_{75}$ " "	---		371	2		
$(Ni_{20}Co_{80})_{75}$ " "	---		394	2		
$Co_{75}P_{16}B_6Al_3$	---		387	2		
$(Fe_{60}Co_{40})_{79}P_{12}B_6Al_3$	437	3				
$(Fe_{60}Co_{40})_{77}P_{14}B_6Al_3$	447	3				
$(Fe_{60}Co_{40})_{75}P_{16}B_6Al_3$	457	3				
$(Fe_{60}Co_{40})_{73}P_{18}B_6Al_3$	467	3				
$(Pd_{80}Ni_{20})_{83}P_{17}$	319	3	329	3		
$(Pd_{80}Ni_{20})_{82}P_{18}$	317	3	330	3		
$(\quad)_{81}P_{19}$	314	3	351	3		
$(\quad)_{80}P_{20}$	317	3	354	3		
$(\quad)_{79}P_{21}$	325	3	356	3		
$(\quad)_{78}P_{22}$	334	3	355	3		
$(\quad)_{77}P_{23}$	339	3	349	3		
$(Pd_{50}Ni_{50})_{83}P_{17}$	311	3	323	3		
$(\quad)_{82}P_{18}$	311	3	323	3		
$(\quad)_{81}P_{19}$	310	3	323	3		

Alloy	Tg	Ref.	Tx	Ref.	Tℓ	Ref.
$(Pd_{50}Ni_{50})_{80}P_{20}$	310	3	377	3		
$(\quad)_{79}P_{21}$	315	3	377	3		
$(\quad)_{78}P_{22}$	320	3	377	3		
$(\quad)_{77}P_{23}$	331	3	377	3		
$(\quad)_{76}P_{24}$	342	3	377	3		
$(\quad)_{75}P_{25}$	353	3	372	3		
$(Pd_{20}Ni_{80})_{84}P_{16}$	---		332	3		
$(\quad)_{83}P_{17}$	327	3	357	3		
$(\quad)_{82}P_{18}$	321	3	344	3		
$(\quad)_{81}P_{19}$	327	3	352	3		
$(\quad)_{80}P_{20}$	329	3	365	3		
$(\quad)_{79}P_{21}$	335	3	372	3		
$(\quad)_{78}P_{22}$	348	3	367	3		
$(\quad)_{77}P_{23}$	349	3	360	3		
$(Pt_{80}Ni_{20})_{80}P_{20}$	207	3				
$(\quad)_{77.7}P_{22.3}$	207	3				
$(\quad)_{75}P_{25}$	207	3				
$(Pt_{75}Ni_{25})_{80}P_{20}$	207	3				
$(Pt_{60}Ni_{40})_{80}P_{20}$	222	3				
$(Pt_{50}Ni_{50})_{80}P_{20}$	247	3				
$(Pt_{40}Ni_{60})_{80}P_{20}$	267	3				
$(Pt_{30}Ni_{70})_{80}P_{20}$	277	3				
$(Pt_{20}Ni_{80})_{80}P_{20}$	297	3				

Alloy	Tg	Ref.	Tx	Ref.	Tℓ	Ref.
$(Pd)_{80}P_{20}$	334	4				
$(Pd_{80}Ni_{20})_{80}P_{20}$	317	4				
$(Pd_{60}N_{40})_{80}P_{20}$	312	4				
$(Pd_{40}N_{60})_{80}P_{20}$	315	4				
$(Pd_{20}N_{80})_{80}P_{20}$	329	4				
$Ni_{80}P_{20}$	345	4				
$(Pd_{85}Fe_{15})_{80}P_{20}$	370	4				
$(Pd_{80}F_{20})_{80}P_{20}$	357	4				
$(Pd_{75}Fe_{25})_{80}P_{20}$	344	4				
$(Pd_{70}Fe_{30})_{80}P_{20}$	339	4				
$(Pt_{80}Ni_{20})_{75}P_{25}$	212	4				
$(Pt_{70}Ni_{30})_{75}P_{25}$	---	4				
$(Pt_{60}Ni_{40})_{75}P_{25}$	229	4				
$(Pt_{50}Ni_{50})_{75}P_{25}$	247	4				
$Pd_{79.5}Cu_6Si_{16.5}$	363	4				
$Fe_{80}P_{13}B_7$			410	5		
$Pd_{82}Si_{18}$	362	6	367	6		
$Pd_{79.5}Au_4Si_{16.5}$	372	6	402	6		
$Pd_{77.5}Cu_6Si_{16.5}$	373	6	413	6		
$Pd_{79.5}Ag_4Si_{16.5}$	367	7		7		
$Pd_{81}Si_{19}$	377	8				

Alloy	Tg	Ref.	Tx	Ref.	Tℓ	Ref.
$Au_{81}Si_{19}$	17	9	5	9	363** 1127*	9
$Au_{77}Ge_{14}Si_9$	12	9	24	9	352** 1077*	9
$Fe_{75}P_{15}C_{10}$	---		347	9	937** 1567*	9
$Pt_{66}Sb_{34}$	---		212	9	612** 1657*	9
$Pd_{80}Si_{20}$	382	9	394	9	827 1527*	9
$Nb_{40}Ni_{60}$	---		697	9	1147** 1837	9
Pd (pure)	277	9	---		1557*	9
$Ni_{72}P_{14}B_6Si_3Al_5$	437	10	442	10		
$Ni_{72}P_{14}B_7C_2Al_5$	---		432	10		
$Fe_{72}P_{16}C_5Si_2Al_5$	457	10	467	10		
$Fe_{75}P_{15}C_6Al_4$	440	11	454	11		
$Fe_{76.6}P_{14.2}C_{1.2}Al_{3.2}B_{4.8}$	447	11	457	11		
$Fe_{77}P_{17}C_4Al_4$	441	11	451	11		
$Fe_{38.5}Ni_{38.5}P_{18}B_2Al_3$	409	11	426	11		
$Fe_{38.5}Ni_{38.5}P_{14}B_6Al_3$	415	11	434	11		
$Fe_{38.5}Ni_{38.5}P_{14}B_6Si_3$	435	11	449	11		
$Fe_{40}Ni_{40}P_{14}B_6$	390	11	400	11		
$Fe_{37.5}Ni_{37.5}P_{16}B_6Al_3$	428	11	441	11		
$Ni_{75.3}P_{16}B_{5.7}Al_3$	420	11	437	11		
$Fe_{29}Ni_{49}P_{14}B_6Al_2$	403	11	431	11		

* Avg. melting temperature of components
** Eutectic

Alloy	Tg	Ref.	Tx	Ref.	Tℓ	Ref.
$Fe_{38.5}Ni_{38.5}P_{20}Al_3$	405	11				
$Fe_{38.5}Ni_{38.5}P_{16}B_4Al_3$	412	11				
$Fe_{38.5}Ni_{38.5}P_{15}B_5Al_3$	413	11				
$Fe_{38.5}Ni_{38.5}P_{13}B_7Al_3$	415	11				
$Fe_{38.5}Ni_{38.5}P_{12}B_8Al_3$	416	11				
$Fe_{38.5}Ni_{38.5}P_{10}B_{10}Al_3$	418	11				
$Au_{77}Ge_{13.6}Si_{9.4}$					352	12
$Au_{81.4}Si_{18.6}$					363	12
$Ni_{72}P_{18}B_7Al_3$	442	13	434	13		
$Ni_{49}Fe_{29}P_{14}B_6Al_2$	403	13	431	13		
$Fe_{76}P_{16}C_4Si_2Al_2$	457	13	461	13		
$Fe_{80}P_{16}B_1C_3$	100	14				
$Fe_{78}Mo_2B_{20}$	440				(2605A)	
$Co_{72}Fe_3P_{16}B_6Al_3$	390					
$Fe_{40}Ni_{40}P_{14}B_6$	400				(2826)	

1. Luborsky & Walter - J. of Applied Phys., V47 #8, Aug. 76.

2. Coleman - Materials Science & Engineering, 23 (1976).

3. Chen - Materials Science & Engineering, 23 (1976).

4. Chen - J. of Non Crystalline Solids, 18 (1975).

5. Yamauchi & Nakagawa - Jap. J. of Appl. Phys 10 (1971).

6. Leamy, Chen, Wang - Metallurgical Transactions 3 (1972).

7. Chen & Goldstein - J. Appl. Phys. 43 #4 (1972).

8. Barmatz & Chen - Phys. Rev. B, V9 #10 (1974).

9. Giessen & Wagner -

10. Chen & Polk - J. Non-Crystalline Solids 15 (1974) 174.

11. Chen & Polk - J. Non-Crystalline Solids 15 (1974) 165).

12. Chen & Turnbull - J. Chem. Phys. 48 #6 (1968) 2560.

13. Pampillo & Polk - Acta Metallurgica 22 (1974) 241.

14. Egami, Flanders, Graham - Proceeding Mag. & Mag. Mat. 1974.

APPENDIX B

FAILURE TO MELT ANALYSIS OF EXPERIMENT 74-49

AUGUST 30, 1977

TO: FRED A. REEVES/FA21
NASA-MARSHALL SPACE FLIGHT CENTER
HUNTSVILLE, ALABAMA 35812

SUBJECT: FAILURE TO MELT ANALYSIS OF EXP 74-49

SUMMARY: Evidence of incipient melting on the surface of the flight specimen indicates that the melting temperature of the specimen was attained, but that the net power, above radiation and conduction losses, available to furnish the latent heat of fusion was too small to appreciably melt the specimen during the 118 second period of high power. This was due to a procedural error committed during the performance of the ground based reference experiments. This led the Principal and Co-Investigators to incorrectly conclude before the flight that sufficient net power would be available to heat and melt the flight specimen with the experiment package configuration used.

The procedural error committed was the performance of these experiments utilizing a matching transformer having a different turns ratio than that of the matching transformer used in the flight apparatus. This caused an increase of the heating efficiency of the breadboard apparatus above its nominal reference power level. Had this error not been committed, it would have been realized that not enough power was available to heat and melt the specimen during the time available in the flight unit with the particular chamber gas mixture and transformer turns ratio employed. As it was, the specimen was melted in one atmosphere of helium in the breadboard apparatus in the available time for melting. Applying the calibrated power scale factor between the breadboard apparatus and the flight apparatus, then led to the incorrect conclusion that the specimen would heat and melt with the mixture of helium and argon used.

The heating efficiency depends very sensitively upon the specimen radius, and to a lesser extent upon its electrical resistivity. The flight specimen is 3.58% smaller than the stainless steel (#316) calibration specimen used in testing the flight package. This was due to the lack of provision in grinding the specimen resulting in flats. The maximum radius is 0.465 cm, the minimum is 0.433 cm, and the average is 0.4445 cm (determined by 10 micrometer readings). The stainless steel ball is precision ground with a radius of 0.461 cm. This reduction in size led to an estimated 16% reduction in absorbed power.

The resistivity and temperature coefficient of resistivity of the stainless steel material matches that of the flight specimen material to within $\sim$ 10% over the required temperature range. Further there is a void structure on the equator plane with a string of voids running from the surface to the center. These effects together led to an estimated 8% reduction in power, so that the total reduction in net power to the flight specimen was 24%. This corresponds to a calculated 45 watts absorbed power instead of the 59 watts expected.

The measured absorbed power in the flight specimen, from the flight pyrometer data is 46 watts. Due to uncertainties in reading temperatures accurately from the flight pyrometer data (because of uncertainties in specimen emissivity), the absorbed power is uncertain to $\pm$ 20%, so that the corresponding absorbed power may be 46 ± 9.2 watts. For a sphere of radius 0.4445 cm, the estimated loss due to radiation and conduction through the chamber gas mixture at 950°C is 38 watts, for an emissivity of 0.8 (estimated from the appearance of the specimen). Due to the irregular shape of the specimen this could be as much as 10% high so that the loss may be 38 + 3.8, -0 watts.

In light of the above information, failure to melt in the allotted time may be explained. The absorbed power at 950°C was nearly equal to the radiation losses, leaving a negligible amount of available power for melting. The melting time was greatly extended and, in the time allotted, only incipient melting on the surface was observed. This is in contrast to the situation planned for the experiment, where 59 watts was estimated to be the absorbed power and the loss due to conduction and radiation was 40.5 watts, leaving 18.5 watts available for melting. Under those circumstances, melting would have occurred in 43 seconds. A margin of 22 seconds was allowed to account for a 10% difference in absorbed power. In the actual experiment the additional losses due to the undersize specimen, the slight difference in resistivity, and the presence of voids, coupled with the uncertainty in actual absorbed power added up to cause a failure to melt in the time allotted.

The recommendations to correct this situation so that failure to melt shall not occur again are:

(1) Introduction of a quench gas to cool the specimen after melting instead of allowing this gas to be present from the outset, which greatly reduces the net melting power margin available.

(2) Insure that the turns ratio on the matching transformer in the breadboard facility is the same as the flight apparatus of each experiment by proper documentation.

(3) Fabricate flight specimens so that they have the correct average radius instead of the correct maximum diameter and eliminate voids.

(4) Perform some calibration tests with the flight specimen in the flight apparatus. If it is determined that melting is required, the flight apparatus would have to be replaced prior to flight. An additional recommendation is to calibrate the flight pyrometer for at least three points with any flight specimen material. These should be the point where the flight pyrometer begins indicating, the melting temperature and one point between these. That will enable absorbed power and loss calculations to be performed with much greater accuracy.

DR. ARTHUR E. LORD, JR.
Drexel University

J. WOUCH
General Electric Company

APPENDIX C

GROUND BASED PREPARATIONS FOR EXPERIMENT 74-49

The laboratory test plan for ground based tests using the breadboard processor and the flight processor was prepared on February 4, 1977 and had the following objectives:

1 - Quantify the performance of the breadboard and the flight unit.

2 - Specimen mounting, clean up, pump down and back fill of breadboard unit.

3 - Melting run using one of the ferromagnetic ground truth specimens.

In implementing the tests use was made of a 316 stainless steel specimen exclusively in the flight unit because it was the nearest material to the Metglas alloy. The flight Metglas specimens were not available for test during the flight unit preparation prior to delivery.

Breadboard tests were run using the same 316 stainless specimen used in the flight unit tests. These tests were followed by the tests using the Metglas alloy.

After the original objectives were met, further tests were deemed essential because of the decentering toward the coil of the magnetic specimen during heating until the curie temperature is reached. Also, the final cooling calculations showed that Argon as used in the 74-48 flight would not cool rapidly enough and if pure Helium was used the specimen may not melt in the flight unit. These tests were all done with the ground truth Amorphous Ferromagnetic specimen.

TEST SEQUENCES

Jan. 18, 19 — Black Body tests of solid state radiometer

Jan. 21-23 — Flight unit tuning, loading and trimming of servo using 316 stainless ball, 0.92 CM dia.

Jan. 25 — 316 S.S. heating test, flight unit; 1 ATM Argon, 1 ATM Helium. Recorded solid state radiometer.

Jan. 26 — 316 S.S. heating tests recording heat sink temp., water temp., and solid state radiometer. 1 Torr Argon, 1 Torr Helium (T.C. gauge pressure).

Feb. 1 — Final flight unit test, no specimen, recorded all T/M lines.

All further tests were with the breadboard set-up.

Feb. 4 — 316 stainless ball, 0.92 CM dia. heating and cooling tests, 1 ATM Helium, 1 ATM Argon. 12:5 matching transformer turns ratio.

Feb. 11 — 316 stainless ball, heating and cooling, 10 Torr Argon, two tests, first with 11:5 turns ratio and next with 12:5 turns ratio on the matching transformer. Proper match was 12:5 ratio*.

* Heating was 15% better at 11:5 but amplifier was saturated so servo would not damp adequately at high power.

Feb. 11 — 316 run with 10 Torr Helium, 12:5 turns ratio on matching transformer, heating and cooling test.

Feb. 15 — Calculation of relative average heating power, breadboard and flight unit.

At this point (from Feb. 11 to Feb. 17) the breadboard was being equipped

for testing the Metglas alloy. No further tests were made using 316 stainless material. Immediately, difficulties arose which we found were due to the magnetic properties of the Metglas alloy. Initial loading was severely mismatched and there was fear the low amplifier efficiency would cause overheating. Experiments were made by varying the transformer turns ratio to try to improve the match. Finally, it was determined that the time to reach the curie temperature was not long enough for the amplifier to overheat and that the match would have to be what was originally determined by the stainless. At this point the 12:5 ratio was supposed to have been restored. Subsequent post flight review of the breadboard equipment disclosed the transformer was marked 12:5 ratio but an actual turn count showed 11:5.

The conclusion is that all tests with the Metglas alloy were done with the 11:5 ratio and its 15% higher heating capability.

Feb. 17	Heated the 2.95 gm Metglas ball to melting.
Mar. 8,9	Replaced defective D.C. to D.C. regulated power supply in flight unit and retested without specimen.
Apr. 18	Breadboard heating test, Metglas alloy, vacuum
Apr. 25	Breadboard heating and cooling tests, Metglas vacuum, 100 Torr Helium, 760 Torr Helium, 100 Torr Argon, 760 Torr Argon
Apr. 26	Breadboard heating and cooling test, Metglas near coil top, 50% He, 50% Ar Mixture
May 5	Breadboard heating tests, Metglas, vacuum, low battery voltages
May 6	Breadboard heating and cooling tests, Metglas, 760 Torr Helium, 100 Torr Helium
May 6	Breadboard melting of Metglas specimen, 100 Torr Helium

No further tests were performed until after the 74-49 experiment flight

CHAPTER V

750-133

CONTAINERLESS PROCESSING TECHNOLOGY EXPERIMENT REPORT

SPAR IV EXPERIMENT 76-20

August 10, 1978

T. G. Wang, D. D. Elleman, N. Jacobi, and R. Tagg

JET PROPULSION LABORATORY
CALIFORNIA INSTITUTE OF TECHNOLOGY
PASADENA, CALIFORNIA

ACKNOWLEDGEMENTS

The authors wish to thank J. Kendall, D. Collins, and M. Saffren of JPL for their valuable assistance in all phases of this experiment. Dr. Wang wishes to thank R. Chassay and M. F. Reeves of MSFC for their patience in handling this experiment and the manuscript.

This paper presents the results of one phase of research carried out at the Jet Propulsion Laboratory, California Institute of Technology, under Contract No. NAS 7-100, sponsored by the National Aeronautics and Space Administration

CONTENTS

Figures

Tables

SECTION I

INTRODUCTION

This report describes one phase of an experimental research program which includes containerless processing studies of high melting-point materials in space. Study of the stability and manipulation of liquid drops at room temperature is a useful and cost-effective intermediate step in the development of a better understanding of the physics of liquid melts and of the capacity to handle such melts in a zero-g environment.

Many of the processes to be performed in space require manipulation and control of weightless molten material (1). In these processes, a melt is to be positioned and formed within a container without contacting the container walls. However, electromagnetic methods of positioning and forming are limited to melts which are electrically conducting (2). An acoustical method that has been developed at JPL can be used to control any molten material (3)(4), both conducting and non-conducting. The acoustical method can be used both for positioning and for inducing oscillation and rotation of a melt (5)(6).

SECTION 2

OBJECTIVES

The broad objective of this task is to study containerless processing of materials in space. In containerless processing, most of the steps are conducted in a liquid-melt state. Our knowledge of the physical properties of liquid melts today is qualitative, or at best, semiquantitative and empirical. The aim of this program is to gain a better understanding of the physics of liquid melts and the capabilities of manipulating liquid melts in a long-term, zero-G environment, thus aiding in the future design of a practical system for space processing.

The primary objectives of the first flight experiment as stated in the proposal, were to:

(1) Determine the positioning capability of the acoustic chamber. The initial perturbation of the drop generated by the drop injection system will be allowed to damp down with the acoustical field on. The time required for a positioned liquid drop to approach its quiescent state can be determined from the film record.

(2) Determine the perturbation of drop shape oscillation due to G-jitter-induced center-of-mass motion. A positioned drop is weakly coupled to the rocket through the acoustic chamber. As the rocket undergoes G-jitter, the drop will move back and forth within the chamber and experience a modulating force, thus perturbing the drop. This perturbation can cause the drop shape oscillation to build up in a short period of time if the periodicity of the perturbing force is close to the normal mode of the drop.

(3) Determine the rotation capability of the acoustic chamber. The torque on the drop generated by the acoustic field will be gradually increased to slowly accelerate the drop up to 2 rps. The rate of spin-up as a function of the torque will establish the rotation capability of the chamber on a liquid drop.

(4) Determine the perturbation of drop rotation induced by G-jitter. As the rocket experiences G-jitter, a rotating drop will move back and forth within the chamber. A drop with non-axisymmetric shape will experience a non-axisymmetric modulating force, thus perturbing the drop rotation. This can produce unwanted coupling between rotation and oscillation of the drop.

(5) Determine the capability of the position servo system. A drop will be allowed limited freedom of motion within the chamber under the influence of low acoustical power. It will be restrained by high acoustical power when the drop

moves beyond predetermined limits. The drop stability obtained using this position servo system will determine whether or not this system design will be adapted on the subsequent flights.

(6) Study the natural resonant frequencies and damping mechanism of drop oscillation. The resonant frequencies and the damping mechanism have been calculated. This experiment will allow comparison of observed and calculated values.

(7) Study the drop shape change due to rotation. The equilibrium shapes of near-rigid body rotation obtained in this experiment will be compared with existing equilibrium calculations. If rotation is to be used as a principle method of shaping liquid melts, it will be important to determine the deviation between calculated and observed shapes.

SECTION 3

APPARATUS AND OPERATION

This study utilized the existing acoustic levitation rocket instrument described in AO:0A-76-02 with no modification for the first flight experiment and minor modifications for subsequent flights. Three rocket flight experiments in a two-year period are planned. The first rocket flight experiment took place on June 21, 1977.

A. APPARATUS

Figure 3-1 shows the rocket 76-20 payload without the orthogonal view windows and the housing. The heart of this apparatus is a triaxial acoustical levitation resonance chamber (7) which will be used to position and control large liquid drops in zero-g environments. The chamber itself is nearly cubical, with inside dimensions of 11.43 x 11.43 x 12.70 cm, which are the x, y, and z faces, respectively. Three acoustic drivers are fixed rigidly to the center of three mutually perpendicular faces of the chamber. During operation of the chamber, each driver

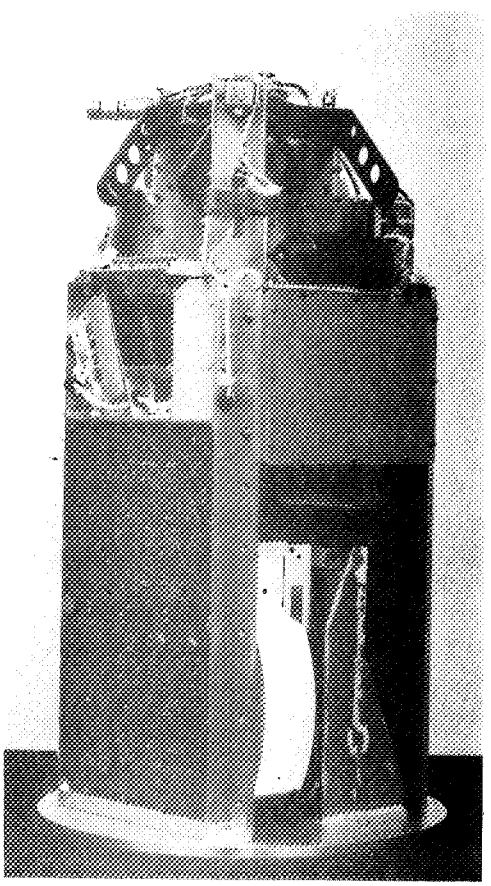

Figure 3-1. Triaxial Acoustical Levitation Resonance Chamber (without orthogonal view windows and housing)

excites the lowest-order standing wave along the direction that the driver faces. In a resonant mode, the ambient pressure is maximum at the nodes of the velocity wave and minimum at the antinodes. Consequently, there is a tendency for introduced liquids and particles to be driven toward the antinodes, where they collect and remain until excitation ceases.

Calculation of the acoustic pressure on the drop is simplified by the fact that the characteristic impedance of the liquid $\rho_\ell c_\ell$ is very much greater than that of the gas ρc: $\rho_\ell c_\ell$ ($\sim 10^5$ cgs)/ρc (~ 40 cgs)/ $\simeq 10^3$ where ρ_ℓ and ρ are the density of liquid and gas, respectively, and c_ℓ and c are the sound velocity of liquid and gas, respectively. Because of this impedance mismatch, the acoustic power in the drop is three orders of magnitude smaller than in the gas and is negligible. This simplifies the expression for the radiation pressure $\langle \Delta P \rangle$, which is time-independent and is given at the boundary by

$$\langle \Delta P \rangle = (\overline{P^2}/2\rho c^2) - (1/2)\rho\ (\overline{\vec{U}^2}) \qquad (1)$$

where P is the excess acoustic pressure, $\vec{U}$ is the gas particle velocity, and the bar over a quantity denotes the time average of the quantity. Eq. (1) is the Bernoulli equation (7), which gives the acoustical perturbation on the ambient pressure from its quiescent value.

The pressure profile in our system can be derived as follows. The velocity potential ϕ of the wave in the chamber can be expressed as

$$\phi = \phi_x \cos (k_x x) e^{i\omega_x t} + \phi_y \cos (k_y y) e^{i\omega_y t}$$

$$+ \phi_z \cos (k_z z) e^{i\omega_z t},$$

where $\phi_{x,y,z}$ are the complex velocity potential amplitudes of standing waves of frequency $\omega_{x,y,z}$ and wave number $k_{x,y,z}$. The particle velocity U, by definition, is $\vec{U} = \nabla\phi$. The pressure is given by $P = -\rho\dot{\phi}$. With only one of the three drivers on ($\phi_x = \phi_y = 0$), the resulting expression for the radiation pressure is

$$\langle \Delta P \rangle_z = \frac{\rho k_z^2\ \phi_z^2}{2} \cos 2k_z z$$

The node is a plane ($z = \ell_z/2$), becoming a point when all three drivers are turned on. This has been verified experimentally. Because this is a three-dimensional system with independent control on each dimension, it has a great deal of versatility. It can position a drop acoustically and then manipulate it; for example, it can induce drop oscillation and/or rotation.

B. OPERATION (ROTATION AND OSCILLATION EXPERIMENTS)

In the following discussion, we discuss the operating characteristics of the acoustic chamber necessary to perform rotation and oscillation experiments. Assume that the sample to be studied is a 1.25-cm-radius (a) water droplet, the residual acceleration is 10^{-1} cm/sec^2 (10^{-4} g), and the quality factor (Q) (defined as $\omega/2\Delta\omega$) of the acoustic chamber is $\sim$25:

(1) Newton's equation for the motion of a water drop in an acoustic pressure field is $\int \langle \Delta P \rangle \, n_x \, dA = \rho_\ell \cdot 10^{-4}$ g $\cdot$ $(4/3)\pi a^3$. In the limit of $ka \ll 1$, this has been calculated by King (10) to be $(P^2/2\rho c^2) \sin 2kx \cdot 2\pi a^3 \cdot k \cdot (5/6) = \rho_\ell \cdot (4/3)\pi a^3 \cdot 10^{-4}$ g. For a sphere 2.5-cm diam, and of density 1 g/cm^3, the corresponding minimum acoustic pressure required to position the drop is $P \simeq 10^3$ dyn/cm$^2 \simeq 134$ dB, where the decibels are measured against the reference effective pressure (2×10^{-4} dyn/cm^2). For a 50% efficient compression driver, less than 0.2 W of electrical power is needed to provide the required acoustic pressure. It is worth pointing out that, at this acoustic pressure level, the surface tension force (F_S) that acts on the water drop is two orders of magnitude larger than the acoustic force (F_A): $F_S/F_A = (\sigma \cdot 2\pi r)/(\int \langle \Delta P \rangle \cdot n_x \cdot dA) \sim 100$.(8)

(2) If the amplitude of the foregoing 134-dB acoustic wave is modulated at a given frequency ω_o, the drop experiences a modulated force $F_o = \int \langle \Delta P \rangle \, n_x \, dA = (\sim 1$ dyn). When ω_o matches the normal oscillation modes of the drop given by $\omega_n^2 = n(n-1)(n+2)(\sigma/\rho a^3)$, the amplitude A of the oscillation, assuming potential flow inside the drop, can be as large as $|A| = |F_o/(i\omega_o M_\ell \cdot \beta_\eta)| = (\sim 1$ cm), where β_η is the damping constant of the nth mode of the drop, and M_ℓ is the mass of the drop. Since the drop radius itself is 1.25 cm, this modulation force is sufficient to drive the drop into large-amplitude oscillation at least at the fundamental frequency. However, a higher power modulation is required for higher modes because of the increase in damping. That there is, in fact, sufficient power do to this has been demonstrated in KC-135 flights, where the prototype was able to shatter a water drop of 1.25-cm radius in less than 1 sec while operating at the fundamental frequency.

(3) If the phase between the two orthogonal 134-dB waves on the x and y axes is locked with 90° phase shift, a torque is produced that spins the drop. In the asymptotic limit, the drop will achieve a rotational velocity of 23 rad/sec, exceeding the maximum rotational velocity (10.1 rad/sec) required for this experiment.

C. FLIGHT EXPERIMENT

SPAR Experiment 76-20, Containerless Processing, was flown on the SPAR IV rocket flight of June 21, 1977. The fluid sample was successfully injected into the levitator chamber, thus demonstrating one of the more critical engineering goals of the experiment, but two malfunctions prevented completion of the experiment. The two flight malfunctions are discussed separately below.

1. Sound Power Failure.

a. Event. The experiment sound power failed at 130 seconds after lift-off, allowing the suspended drop to drift to the chamber wall. The failure was in the low power mode of operation. Telemetry indicated that the experiment functioned normally in all other respects and that sound power resumed when programmed to the high power mode at 260 seconds. By this time the drop had impacted the wall.

b. Investigation. Upon return of the instrument to JPL, a functional test was conducted. The instrument electronics were found to function as they had during flight. Three TTL integrated circuit (IC) chips were found to be damaged. All performed identical functions, and all interfaced the instrument programmer with the GSE. An apparently identical failure had occurred at Goddard Space Flight Center (GSFC) during integration testing and at WSPG during prelaunch tests. The report of parts failure analysis conducted at JPL on the flight ICs is attached. It indicates that a high voltage, high current source was applied to the inputs of the failed device between ground or V_{CC} and the leads which interface to the GSE. (Note: The failure on lift-off mentioned in the Parts Failure Analysis Report has not been verified.) Four of the nine interface inputs failed. Only one of these failures caused an instrument malfunction. The immediate cause of the failure has not been determined with certainty. It appears to have been some "high" voltage ($<<5$ volts) applied to the GSE control lines or to the GSE instrument ground, apparently through an intermittent failure in the GSE when GSE switches 1, 2, 6, and 9 happened to be closed to complete the fault circuit. The failure at GSFC, seemingly the same as that during flight, was with a 30-foot umbilical cable, so that the cause does not appear to be related to the 800-foot umbilical cable at WSPG.

c. Corrective Action. The ultimate cause of the failure must be ascribed to a circuit design error. The I/O circuits should be isolated through optical couplers or transformers. This will be done for future flights of experiments 76-19 and 76-20.

The GSE will be re-designed for the modified instrument; thus, any present short will be eliminated.

2. Film Contrast Degradation

a. Event. The flight film was of very low contrast, apparently caused by scattered light. The film record shows first a normal view of the chamber with good contrast. This corresponds to pre-launch camera tests and eliminates film processing as the source of the problem. During the flight, considerable fog is noted, appearing as a smoke swirling around throughout the entire frame, not just within the chamber. Later, on ground impact (reported to be 125 g's), the camera was caused to run again. At that time the scattered light was worse, obscuring almost all details of the chamber.

b. Investigation. Post flight tests of the experiment yielded normal exposures with good resolution. Blowing cigar smoke into the field of view caused light scattering similar to that observed in the flight film, but less dense.

The lens of the camera was noted to have deposited on it considerable dust-like contaminants, as well as evidence of dried droplets. Accordingly, both it and one of the viewing mirrors were removed and flushed with pure Benzene which was then tested. As suspected, silicone oil well above detection limits was noted on both pieces, approximately 0.1 milligrams on the lens and 0.2 milligrams on the section of mirror flushed with Benzene. This tends to confirm previous suspicion; namely, that the use of silicone oil for droplet formation in the original Learjet flight tests resulted in contamination of the inside skin of the rocket extension tube in which Experiment 76-20 is mounted.

It is hypothesized that launch skin temperature, estimated to be above 350°F, caused vaporization of the silicone oil, and that the air within the extension tube remained cool enough to cause condensation into smoke-like particulates. This in turn caused severe scattering after launch and even more severe scattering after re-entry when the camera was turned on at impact.

The lens had been cleaned prior to flight and the flight mirror had not been previously exposed to the experiment during silicone oil droplet testing. All of this suggests contamination during flight. The scattering during flight, but not previously or afterward, suggests the time of contamination as being only during flight, with re-entry causing the greater effect due to its slightly higher rocket skin temperatures. It was also noted that the thin sections of the extension tube wall felt dry after flight, whereas the thick section, which remains cooler during aerodynamic heating, still felt oily.

Tests in an oven revealed that a thin film of silicone oil does smoke at an oven temperature of >250°F when the oven door is opened, allowing cooler air to enter.

c. Corrective Action. The entire experiment, particularly the inside surface of the extension tube, will be degreased prior to future flights. The instruments will not be exposed to silicone oil at any time.

d. Objectives Accomplished. The objectives of the first flights as listed in Section 2 were not achieved. However, we did have 30 seconds of free oscillation, superimposed on a slow drift. This segment of data allowed us to study the natural resonant frequencies of a liquid drop as presented in Section 4, and the SPAR velocity and acceleration as presented in Appendix A.

SECTION 4

DATA ANALYSIS

A. INTRODUCTION

The data analysis described below is rendered difficult by two factors:

(1) Due to malfunction of the electronics we did not achieve the main purpose of this flight, oscillation and rotation of a large drop induced by proper combinations of acoustic fields. Instead, we have a 30-sec segment of free oscillation, superimposed on a slow drift of the drop in the microgravity environment (see Section 4C) until impact on the back wall of the chamber. The sequence of events is given in Table 4-1. The last 29.6 sec of free oscillations are analyzed in this report.

(2) Silicon oil remnants were inadvertently left in the acoustic chamber, giving rise to foggy images throughout the flight. Of the three views expected, only the main view could be processed and used with some degree of confidence. One side view could be used only for crude purposes (center of mass motion, see Section 4C), the other side view was totally unusable. Obviously, more than one view is needed to extract three-dimensional information on shapes of oscillating (and rotating) drops.

Table 4-1. Sequence of Events

Clock Time (sec)	Event
100.0	Injectors start deploying
100.4	Injectors complete deploying
105.1	Liquid first appears
121.7	Injectors start retracting
129.4	Injectors complete retracting
130.0	Acoustic field turns off
	Drop begins drift to wall
159.6	Impact on wall

The rest of this section is arranged as follows. Section 4B describes boundary analysis performed on 120 hand-traced and digitized frames. Due to the low quality of the data and the associated crude procedure of digitizing, this is mostly a preview to the next flight. Next (Section 4C), we describe the center of mass motion of the drop while drifting backwards to the wall. Section 4D contains analysis of two bright spots, which were in the given case more clearly defined than the boundary, as well as a computer experiment simulating the experimental conditions. Some transformations applied to the digitized data are also described, and preliminary attempts at reducing noise (still ongoing at the present time) are discussed in Section 4E. A concluding section follows.

B. BOUNDARY ANALYSIS

Approximately 120 frames were processed with the purpose of analyzing drop boundaries as a function of time. Projected images of the drop were hand-traced and digitized. The digitization was carried out by tracing each contour three times, digitizing 150 to 200 points for each frame. A typical sample is shown in Figure 4-1, revealing considerable noise due to hand tracing and subsequent hand digitization of the traces, as well as nonuniformities in the digitzed points. While noise reduction is a complicated procedure, if at all possible, the problem of finding the best equilibrium shape of the traced boundary

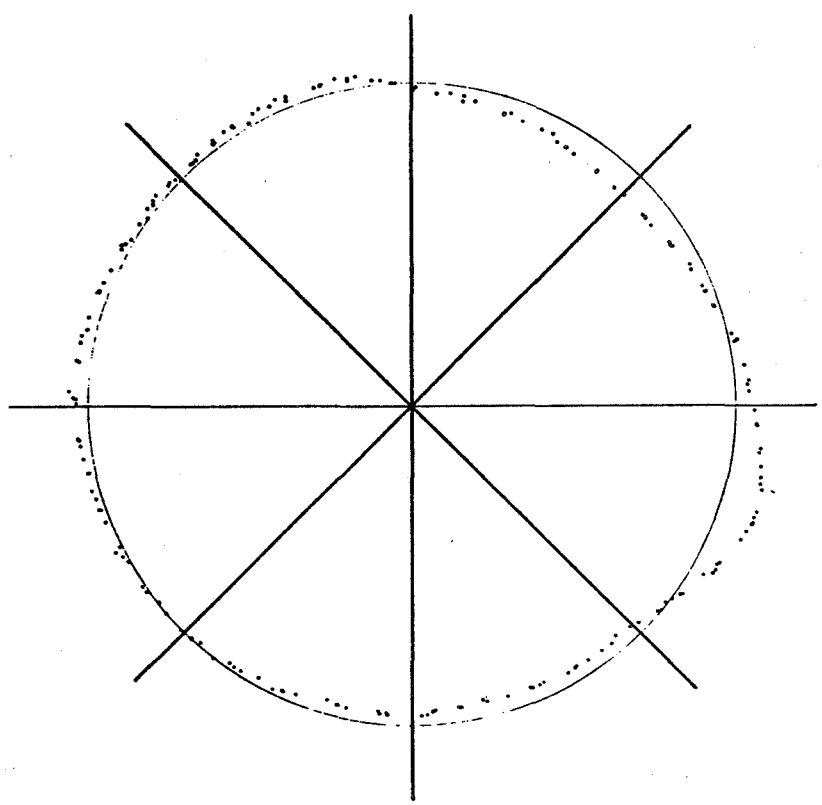

Figure 4-1. Sample of Digitized Drop Boundary

(a circle in the present case; generalization to ellipse can be done easily when needed) was readily handled by the following nonlinear least square procedure.

The numerical problem is the following: given the coordinates of N point (x_i, y_i), i = 1, ..., N, what is the circle closest to these points in the least square sense? The quantities to be determined are x_0, y_0 (the coordinates of the center), and R (the radius of the circle). The deviation of each point from the circle is:

$$\delta_i = \sqrt{(x_i - x_0)^2 + (y_i - y_0)^2} - R$$

and the quantity to be minimized is

$$S = \sum_{i=1}^{N} \delta_i^2$$

Imposing the least squares criterion,

$$\frac{\partial S}{\partial x_0} = \frac{\partial S}{\partial y_0} = \frac{\partial S}{\partial R} = 0$$

gives the following nonlinear system of equations in x_0, y_0, and R:

$$f_1(x_0, y_0, R) = \sum_{i=1}^{N} \left(\sqrt{(x_i - x_0)^2 + (y_i - y_0)^2} - R \right)$$

$$\cdot \frac{x_i - x_0}{\sqrt{(x_i - x_0)^2 + (y_i - y_0)^2}} = 0$$

Multiple pages missing from document.

E. COLINEARITY EQUATIONS: SOLVE FOR (x_o, y_o, z_o)

$$\left(x_n - x_o, y_n - y_o, z_n - z_o\right) \times \left(x_o - x^m, y_o - y^m, z_o\right) = \vec{0}$$

$$\left(\tilde{x_n} - x_o, \tilde{y_n} - y_o, \tilde{z_n} - z_o\right) \times \left(x_o - x^s, y_o, z_o - z^s\right) = \vec{0}$$

These yield four independent equations:

$$y_o + \frac{y^m - y_n}{z_n} z_o = y^m$$

$$x_o + \frac{x^m - x_n}{z_n} z_o = x^m$$

$$\frac{z^s - \tilde{z_n}}{\tilde{y_n}} y_o + z_o = z^s$$

$$x_o + \frac{x^s - \tilde{x_n}}{\tilde{y_n}} y_o = x^s$$

Have four equations in three unknowns: Use least squares method, i.e., have a system

$$A_{4\times3}\, \underset{\sim}{x}_{3\times1} = \underset{\sim}{y}_{4\times1}$$

Since the coefficients in A and $\underset{\sim}{y}$ are experimental values, the equations are not necessarily consistent: for a given choice of $\underset{\sim}{x}$ (say that determined from the first three equations alone), it is necessary to write

$$A\underset{\sim}{x} + \underset{\sim}{r} = \underset{\sim}{y}$$

where $\underset{\sim}{r}$ is the residual vector. The least squares solution for $\underset{\sim}{x}$ minimizes $\|\underset{\sim}{r}\|^2 \equiv r_1^2 + r_2^2 + r_3^2 + r_4^2$. This solution is obtained by solving (see Noble, Applied Linear Algebra p. 39 ff)

$$A^T A \underset{\sim}{x} = A^T \underset{\sim}{y}$$

Writing in matrix form, the system to be solved is:

$$\begin{pmatrix} 0 & 1 & \dfrac{y^m - y_n}{z_n} \\ 1 & 0 & \dfrac{x^m - x_n}{z_n} \\ 0 & \dfrac{z^s - z_n}{y_n} & 1 \\ 1 & \dfrac{x^s - x_n}{y_n} & 0 \end{pmatrix} \begin{pmatrix} x_o \\ y_o \\ z_o \end{pmatrix} = \begin{pmatrix} y^m \\ x^m \\ z^s \\ x^s \end{pmatrix}$$

$$A = \begin{pmatrix} 0 & 1 & \dfrac{y^m - y_n}{z_n} \\ 1 & 0 & \dfrac{x^m - x_n}{z_n} \\ 0 & \dfrac{z^s - z_n}{y_n} & 1 \\ 1 & \dfrac{x^s - x_n}{y_n} & 0 \end{pmatrix}$$

$$A^T = \begin{pmatrix} 0 & 1 & 0 & 1 \\ 1 & 0 & \dfrac{z^s - z_{\tilde{n}}}{y_{\tilde{n}}} & \dfrac{x^s - x_{\tilde{n}}}{y_{\tilde{n}}} \\ \dfrac{y^m - y_n}{z_n} & \dfrac{x^m - x_n}{z_n} & 1 & 0 \end{pmatrix}$$

$$A^T A = \begin{pmatrix} 2 & \dfrac{x^s - x_{\tilde{n}}}{y_{\tilde{n}}} & \dfrac{x^m - x_n}{z_n} \\ \dfrac{x^s - x_{\tilde{n}}}{y_{\tilde{n}}} & \left[1 + \left(\dfrac{x^s - x_{\tilde{n}}}{y_{\tilde{n}}}\right)^2 + \left(\dfrac{z^s - z_{\tilde{n}}}{y_{\tilde{n}}}\right)^2\right] & \left[\dfrac{y^m - y_n}{z_n} + \dfrac{z^s - z_{\tilde{n}}}{y_{\tilde{n}}}\right] \\ \dfrac{x^m - x_n}{z_n} & \left[\dfrac{y^m - y_n}{z_n} + \dfrac{z^s - z_{\tilde{n}}}{y_{\tilde{n}}}\right] & \left[1 + \left(\dfrac{x^m - x_n}{z_n}\right)^2 + \left(\dfrac{y^m - y_n}{z_n}\right)^2\right] \end{pmatrix}$$

which is symmetric about the diagonal.

$$A^T \underset{\sim}{y} = \begin{pmatrix} x^m + x^s \\ x^s \dfrac{x^s - x_{\tilde{n}}}{y_{\tilde{n}}} + z^s \dfrac{z^s - z_{\tilde{n}}}{y_{\tilde{n}}} + y^m \\ x^m \dfrac{x^m - x_n}{z_n} + y^m \dfrac{y^m - y_n}{z_n} + z^s \end{pmatrix}$$

F. DATA FITS

1. Least Squares Fit.

It is desired to fit data in a least squares sense to Equations of the form:

$$x^{(i)} = s_o + v_o\, t^{(i)} + \frac{1}{2}\, a\, t^{(i)^2}$$

This can be expressed in the form $A\underset{\sim}{x} = \underset{\sim}{y}$:

$$\begin{pmatrix} 1 & t^{(1)} & \frac{1}{2}t^{(1)^2} \\ 1 & t^{(2)} & \frac{1}{2}t^{(2)^2} \\ \vdots & \vdots & \vdots \\ 1 & t^{(13)} & \frac{1}{2}t^{(13)^2} \end{pmatrix} \begin{pmatrix} s_o \\ v_o \\ a \end{pmatrix} = \begin{pmatrix} x^{(1)} \\ x^{(2)} \\ \vdots \\ x^{(13)} \end{pmatrix}$$

The solution is given by solving $A^T A\underset{\sim}{x} = A^T\underset{\sim}{y}$, i.e.,

$$\begin{pmatrix} 1 & 1 & \cdots & 1 \\ t^{(1)} & t^{(2)} & \cdots & t^{(13)} \\ \frac{1}{2}t^{(1)^2} & \frac{1}{2}t^{(2)^2} & \cdots & \frac{1}{2}t^{(13)^2} \end{pmatrix} \begin{pmatrix} 1 & t^{(1)} & \frac{1}{2}t^{(1)^2} \\ 1 & t^{(2)} & \frac{1}{2}t^{(2)^2} \\ \vdots & \vdots & \vdots \\ 1 & t^{(13)} & \frac{1}{2}t^{(13)^2} \end{pmatrix} \begin{pmatrix} s_o \\ v_o \\ a \end{pmatrix} = \begin{pmatrix} 1 & 1 & \cdots & 1 \\ t^{(1)} & t^{(2)} & \cdots & t^{(13)} \\ \frac{1}{2}t^{(1)^2} & \frac{1}{2}t^{(2)^2} & \cdots & \frac{1}{2}t^{(13)^2} \end{pmatrix} \begin{pmatrix} x^{(1)} \\ x^{(2)} \\ \vdots \\ x^{(13)} \end{pmatrix}$$

Note: Let $t^{(i)} = t^{(i)}_{DATA} - 130.0$

$$\begin{pmatrix} 13 & \sum t^{(i)}_{DATA} - 130) & \frac{1}{2}\sum\left(t^{(i)}_{DATA} - 130\right)^2 \\ \sum t^{(i)}_{DATA} - 130 & \frac{1}{2}\sum\left(t^{(i)}_{DATA} - 130\right)^3 & \\ & \frac{1}{4}\sum\left(t^{(i)}_{DATA} - 130\right)^4 & \end{pmatrix} \begin{pmatrix} s_o \\ v_o \\ a \end{pmatrix} = \begin{pmatrix} \sum x^{(i)} \\ \sum x^{(i)}\left(t^{(i)}_{DATA} - 130\right) \\ \frac{1}{2}\sum x^{(i)}\left(t^{(i)}_{DATA} - 130\right)^2 \end{pmatrix}$$

Matrix is symmetric, therefore the lower left is not written.

The residuals are given in Table A-6.

a. X-direction Solution

$$\begin{pmatrix} 13 & 194.4 & 2013.43 \\ 194.4 & 4026.86 & 46737.342 \\ 2013.43 & 46737.342 & 577150.6462 \end{pmatrix} \begin{pmatrix} s_{x_o} \\ v_{x_o} \\ a_x \end{pmatrix} = \begin{pmatrix} 31.48 \\ 31.43 \\ 481.78 \\ 480.908 \\ 5044.3358 \\ 5036.3901 \end{pmatrix}$$

s_{x_o} = 2.30 inches

v_{x_o} = 4.45×10^{-3} inches sec^{-1} = 1.13×10^{-2} cm sec^{-1}

a_x = 3.56×10^{-4} inches sec^{-2} = 9.05×10^{-4} cm sec^{-2}

= 0.923×10^{-6} g

b. Y-direction Solution

$$\begin{pmatrix} 13 & 194.4 & 2013.43 \\ 194.4 & 4026.86 & 46737.342 \\ 2013.43 & 46737.342 & 577150.6462 \end{pmatrix} \begin{pmatrix} s_{y_o} \\ v_{y_o} \\ a_y \end{pmatrix} = \begin{pmatrix} 35.04 \\ 578.318 \\ 6250.2271 \end{pmatrix}$$

$$s_{y_o} = 2.03 \text{ inches}$$

$$v_{y_o} = 3.53 \times 10^{-2} \text{ inches sec}^{-1} = 8.96 \times 10^{-2} \text{ cm sec}^{-1}$$

$$a_y = 8.93 \times 10^{-4} \text{ inches sec}^{-2} = 2.27 \times 10^{-3} \text{ cm sec}^{-2}$$

$$= 2.32 \times 10^{-6} \text{ g}$$

c. Z-direction Solution

$$\begin{pmatrix} 13 & 194.4 & 2013.43 \\ 194.4 & 4026.86 & 46737.342 \\ 2013.43 & 46737.342 & 577150.6462 \end{pmatrix} \begin{pmatrix} s_{z_o} \\ v_{z_o} \\ a_z \end{pmatrix} = \begin{pmatrix} 19.23 \\ 220.881 \\ 1934.73695 \end{pmatrix}$$

$$s_{z_o} = 2.17 \text{ inches}$$

$$v_{z_o} = -1.64 \times 10^{-2} \text{ inches sec}^{-1} = -4.17 \times 10^{-2} \text{ cm sec}^{-1}$$

$$a_z = -2.91 \times 10^{-3} \text{ inches sec}^{-2} = -7.39 \times 10^{-3} \text{ cm sec}^{-2}$$

$$= -7.54 \times 10^{-6} \text{ g}$$

2. Linear Fit.

Try a linear fit: $x = S_o + v_o(t-130.0)$

$$\begin{pmatrix} 1 & \cdots & 1 \\ t^{(1)}-130 & \cdots & t^{(13)}-130 \end{pmatrix} \begin{pmatrix} 1 & t^{(1)}-130 \\ \vdots & \vdots \\ 1 & t^{(13)}-130 \end{pmatrix} \begin{pmatrix} s_o \\ v_o \end{pmatrix} - \begin{pmatrix} 1 & \cdots & 1 \\ t^{(1)}-130 & \cdots & t^{(13)}-130 \end{pmatrix} \begin{pmatrix} x^{(1)} \\ \vdots \\ x^{(13)} \end{pmatrix}$$

$$\begin{pmatrix} 13 & \sum\left(t^{(i)}-130\right) \\ \sum\left(t^{(i)}-130\right) & \sum\left(t^{(i)}-130\right)^2 \end{pmatrix} \begin{pmatrix} s_o \\ v_o \end{pmatrix} - \begin{pmatrix} \sum x^{(i)} \\ \sum x^{(i)}\left(t^{(i)}-130\right) \end{pmatrix}$$

$$\begin{pmatrix} 13 & 194.4 \\ 194.4 & 4026.86 \end{pmatrix} \begin{pmatrix} s_o \\ v_o \end{pmatrix} - \begin{pmatrix} \sum x^{(i)} \\ \sum x^{(i)}\left(t^{(i)}-130\right) \end{pmatrix}$$

The residuals are given in Table A-7.

a. X-direction Solution

$$\begin{pmatrix} 13 & 194.4 \\ 194.4 & 4026.86 \end{pmatrix} \begin{pmatrix} s_{o_x} \\ v_{o_x} \end{pmatrix} = \begin{pmatrix} 13.43 \\ 480.908 \end{pmatrix}$$

$s_{o_x} = 2.27$ inches

$v_{o_x} = 9.74 \quad 10^{-3}$ inches sec^{-1}

b. Y-direction Solution

$$\begin{pmatrix} 13 & 194.4 \\ 194.4 & 4026.86 \end{pmatrix} \begin{pmatrix} s_{o_y} \\ v_{o_y} \end{pmatrix} = \begin{pmatrix} 35.04 \\ 578.318 \end{pmatrix}$$

$s_{o_y} = 1.97$ inches

$v_{o_y} = 4.85 \times 10^{-2}$ inches sec^{-1}

c. Z-direction Solution

$$\begin{pmatrix} 13 & 194.4 \\ 194.4 & 4026.86 \end{pmatrix} \begin{pmatrix} s_{o_z} \\ v_{o_z} \end{pmatrix} = \begin{pmatrix} 19.23 \\ 220.881 \end{pmatrix}$$

$s_{o_z} = 2.37$

$v_{o_z} = -5.96 \times 10^{-2}$ inches sec^{-1}

3. Cubic Fit.

Try fitting to a cubic:

$$\begin{pmatrix} 1 & \cdots & 1 \\ \left(t^{(1)}-130\right) & \cdots & \left(t^{(13)}-130\right) \\ \frac{1}{2}\left(t^{(1)}-130\right)^2 & \cdots & \frac{1}{2}\left(t^{(13)}-130\right)^2 \\ \frac{1}{6}\left(t^{(1)}-130\right)^3 & \cdots & \frac{1}{6}\left(t^{(13)}-130\right)^3 \end{pmatrix} \begin{pmatrix} 1 & \left(t^{(1)}-130\right) & \frac{1}{2}\left(t^{(1)}-130\right)^2 & \frac{1}{6}\left(t^{(1)}-130\right)^3 \\ \vdots & \vdots & \vdots & \vdots \\ 1 & \left(t^{(13)}-130\right) & \frac{1}{2}\left(t^{(13)}-130\right)^2 & \frac{1}{6}\left(t^{(1)}-130\right)^3 \end{pmatrix} \begin{pmatrix} s_o \\ v_o \\ a \\ b \end{pmatrix} = \begin{pmatrix} 1 & \cdots & 1 \\ \left(t^{(1)}-130\right) & \cdots & \left(t^{(13)}-130\right) \\ \frac{1}{2}\left(t^{(1)}-130\right)^2 & \cdots & \frac{1}{2}\left(t^{(13)}-130\right)^2 \\ \frac{1}{6}\left(t^{(1)}-130\right)^3 & \cdots & \frac{1}{6}\left(t^{(13)}-130\right)^3 \end{pmatrix} \begin{pmatrix} x^{(1)} \\ \vdots \\ x^{(13)} \end{pmatrix}$$

$$\begin{pmatrix} 13 & \sum\left(t^{(1)}-130\right) & \frac{1}{2}\sum\left(t^{(1)}-130\right)^2 & \frac{1}{6}\sum\left(t^{(1)}-130\right)^3 \\ & \sum\left(t^{(1)}-130\right)^2 & \frac{1}{2}\sum\left(t^{(1)}-130\right)^3 & \frac{1}{6}\sum\left(t^{(1)}-130\right)^4 \\ & & \frac{1}{4}\sum\left(t^{(1)}-130\right)^4 & \frac{1}{12}\sum\left(t^{(1)}-130\right)^5 \\ & \text{SYMMETRIC} & & \frac{1}{36}\sum\left(t^{(1)}-130\right)^6 \end{pmatrix} \begin{pmatrix} s_o \\ v_o \\ a \\ b \end{pmatrix} = \begin{pmatrix} \sum x^{(1)} \\ \sum x^{(1)}\left(t^{(1)}-130\right) \\ \frac{1}{2}\sum x^{(1)}\left(t^{(1)}-130\right)^2 \\ \frac{1}{6}\sum x^{(1)}\left(t^{(1)}-130\right)^3 \end{pmatrix}$$

$$\begin{pmatrix} 13 & 194.4 & 2013.43 & 15,579.114 \\ 194.4 & 4026.86 & 46,737.342 & 384,767.0975 \\ 2013.43 & 46,737.342 & 577,150.6462 & 4,937,154.457 \\ 15,579.14 & 384767.0975 & 4938154.457 & 43,369,392.74 \end{pmatrix} \begin{pmatrix} s_o \\ v_o \\ a \\ b \end{pmatrix} = {}^{x}\begin{pmatrix} 31.43 \\ 480.908 \\ 5036.3901 \\ 39240.40631 \end{pmatrix} {}^{y}\begin{pmatrix} 35.04 \\ 578.318 \\ 6250.227 \\ 49605.20266 \end{pmatrix} {}^{z}\begin{pmatrix} 19.23 \\ 220.881 \\ 1934.73695 \\ 13241.81273 \end{pmatrix}$$

The residuals are given in Table A-8.

a. <u>X-direction Solutions</u>

$s_o = 2.30$ inches

$v_o = 4.17 \times 10^{-3}$ inches sec^{-1}

$a = 4.06 \times 10^{-4}$ inches sec^{-2}

$b = -3.40 \times 10^{-6}$ inches sec^{-3}

b. <u>Y-direction Solutions</u>

$s_o = 2.02$ inches

$v_o = 3.93 \times 10^{-2}$ inches sec^{-1}

$a = 1.78 \times 10^{-4}$ inches sec^{-2}

$b = 4.85 \times 10^{-5}$ inches sec^{-3}

c. Z-direction Solutions

s_o = 2.14 inches

v_o = -4.87×10^{-4} inches sec^{-1}

a = -5.72×10^{-3} inches sec^{-2}

b = 1.91×10^{-4} inches sec^{-3}

4. COMPARISON OF FITS

Note: These fits have been done without any weighting according to the uncertainties of the initial data in Table A-1.

a. Parameters.

	Linear	Quadratic	Cubic	
Initial Position	$\begin{pmatrix} 2.27 \\ 1.97 \\ 2.37 \end{pmatrix}$	$\begin{pmatrix} 2.30 \\ 2.03 \\ 2.17 \end{pmatrix}$	$\begin{pmatrix} 2.30 \\ 2.02 \\ 2.14 \end{pmatrix}$	Inches
Velocity	$\begin{pmatrix} 0.97 \\ 4.85 \\ -5.96 \end{pmatrix} \times 10^{-2}$	$\begin{pmatrix} 0.45 \\ 3.53 \\ -1.64 \end{pmatrix} \times 10^{-2}$	$\begin{pmatrix} 0.42 \\ 3.93 \\ -0.05 \end{pmatrix} \times 10^{-2}$	Inches/ Sec
Acceleration	--	$\begin{pmatrix} 0.36 \\ 0.89 \\ -2.91 \end{pmatrix} \times 10^{-3}$	$\begin{pmatrix} 0.41 \\ 0.18 \\ -5.72 \end{pmatrix} \times 10^{-3}$	Inches/ Sec^2
"6"	--	--	$\begin{pmatrix} -0.03 \\ 0.49 \\ 1.91 \end{pmatrix} \times 10^{-4}$	Inches/ Sec^2
	$\begin{pmatrix} 0.0195 \\ 0.0369 \\ 0.1172 \end{pmatrix}$	$\begin{pmatrix} 0.0140 \\ 0.0126 \\ 0.0286 \end{pmatrix}$	$\begin{pmatrix} 0.0142 \\ 0.0113 \\ 0.0201 \end{pmatrix}$	

b. Residuals

$$\sqrt{\frac{\Sigma |\Delta_x|^2}{N-1}}$$

where

n=1 = 12

c. Conclusions

The value $\sqrt{\Sigma|\Delta_x|^2/N-1}$ is a measure of "goodness of fit" of the polynomials to the observed coordinates; the cubic appears slightly better than the quadratic but this is not surprising since there are more parameters to adjust. Consequently, on the assumption that the acceleration did not change over the 30-second timespan of interest, the values for velocity and acceleration from the quadratic fit have been chosen for report. The reported values are the vector magnitudes.

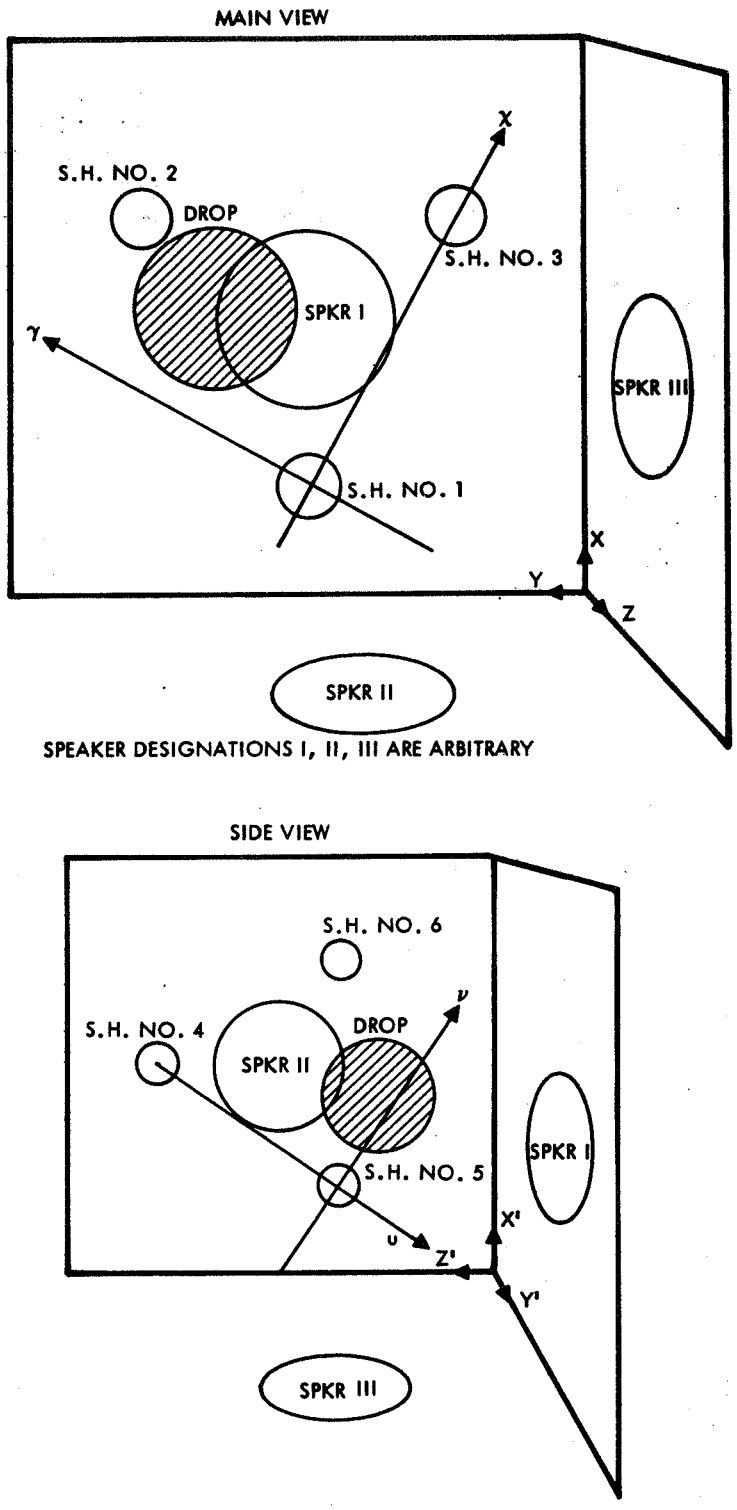

Figure A-1. Screwhead Coordinate System

DATA	
$\frac{a}{2}$ = 2.250 IN. ±0.005 IN.	
$\frac{b}{2}$ = 2.500 IN. ±0.005 IN.	
r = 1.125 IN. ±0.005 IN.	(?) ERROR NOT SPECIFIED ON BLUE POINT

SCREWHEADS 1,2,3 (XY PLANE: Z = 0)

	COORD (X,Y,Z)	
SH. 1	$\left(\frac{a}{2}-r, \frac{a}{2}, 0\right)$	(1,125, 2.25, 0)
SH. 2	$\left(\frac{a}{2}+\frac{r}{2}, \frac{a}{2}+\frac{r\sqrt{3}}{2}, 0\right)$	(2.8125, 3.2243, 0)
SH. 3	$\left(\frac{a}{2}+\frac{r}{2}, \frac{a}{2}-\frac{r\sqrt{3}}{2}, 0\right)$	(2.8125, 1.2757, 0)

SCREWHEADS 4,5,6 (XZ PLANE: Y = 0)

	COORD (X,Y,Z)	
SH. 4	$\left(\frac{a}{2}, 0, \frac{b}{2}+r\right)$	(2.25, 0, 3.625)
SH. 5	$\left(\frac{a}{2}-\frac{r\sqrt{3}}{2}, 0, \frac{b}{2}-\frac{r}{2}\right)$	(1.2757, 0, 1.9375)
SH. 6	$\left(\frac{a}{2}+\frac{r\sqrt{3}}{2}, 0, \frac{b}{2}-\frac{r}{2}\right)$	(3.2243, 0,1.9375)

SCREWHEAD 7,8,9 (YZ PLANE: X = 0)

	COORD (X,Y,Z)
SH. 7	$\left(0, \frac{a}{2}, \frac{b}{2}+r\right)$
SH. 8	$\left(0, \frac{a}{2}+\frac{r\sqrt{3}}{2}, \frac{b}{2}-\frac{r}{2}\right)$
SH. 9	$\left(0, \frac{a}{2}-\frac{r\sqrt{3}}{2}, \frac{b}{2}-\frac{r}{2}\right)$

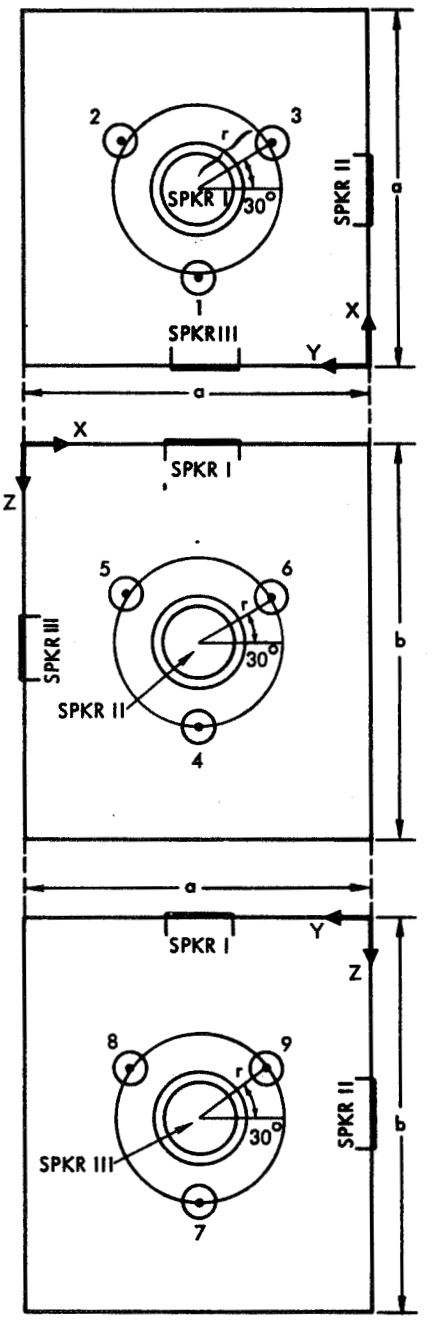

Figure A-2. Coordinates of Screwheads in (x, y, z) Frame

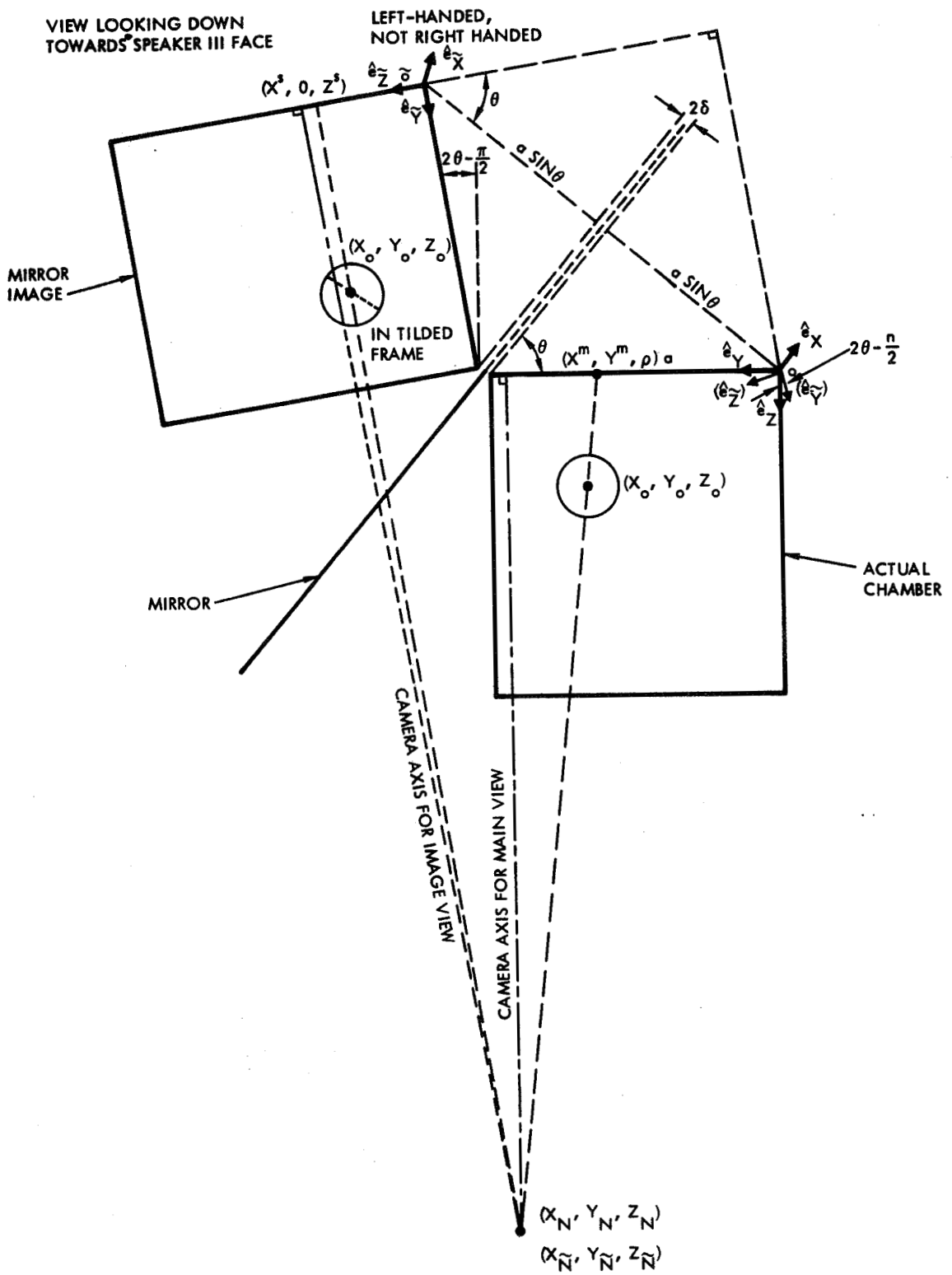

Figure A-3. View Looking Down Towards Speaker III Face

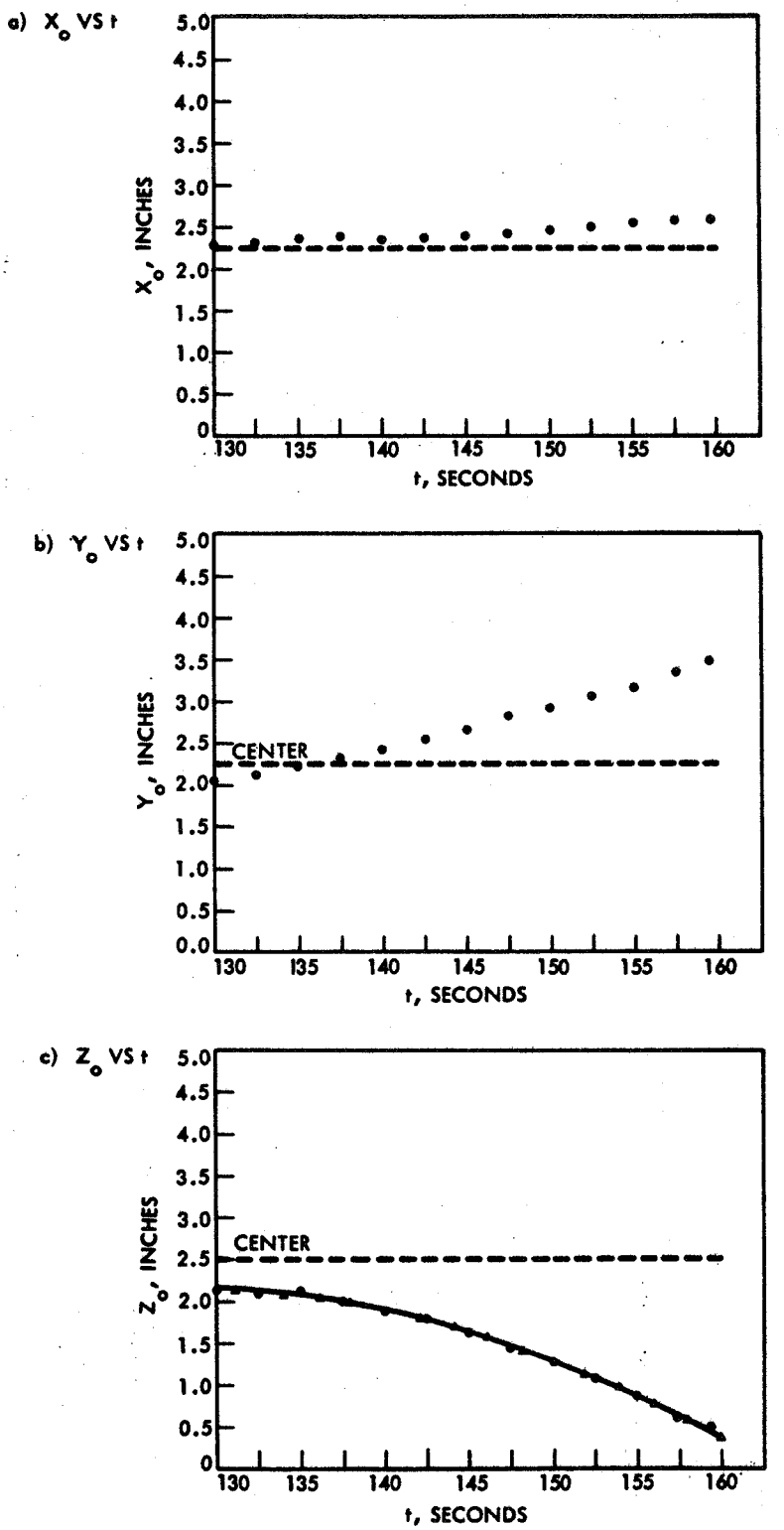

Figure A-4. Drop Trajectory

Table A-1. SPAR Drop Trajectory Calculation Trace Data

Main View

Time	Data X_1	X_2	X_3	$\bar{X}$	$\Sigma(\Delta X_i)^2$	σ_X	$\sigma_{\bar{X}}$	Frame #
130.0	45.5	46.5	45.5	45.8	0.67	0.6	0.3	3174
132.5	43.5	43.5	44.0	43.7	0.17	0.3	0.2	3295
135.0	42.0	43.0	42.5	42.5	0.50	0.5	0.3	3416
137.5	41.5	40.0	40.5	40.7	1.17	0.8	0.4	3537
140.0	38.0	38.0	37.0	37.7	0.67	0.6	0.3	3659
142.5	35.5	36.0	35.5	35.7	0.17	0.3	0.2	3780
145.0	34.5	36.0	35.0	35.2	1.17	0.8	0.4	3901
147.5	32.5	33.5	33.0	33.0	0.50	0.5	0.2	4023
150.0	31.5	31.0	32.0	31.5	0.50	0.5	0.2	4144
152.5	30.5	30.5	32.0	31.0	1.50	0.9	0.5	4266
155.0	29.5	30.5	29.0	29.7	1.17	0.8	0.4	4387
157.5	27.5	28.0	28.5	28.0	0.50	0.5	0.2	4508
159.4	26.5	25.0	26.0	25.8	1.17	0.8	0.4	4601

Time	Y_1	Y_2	Y_3	$\bar{Y}$	$\Sigma(\Delta Y_i)^2$	σ_Y	$\sigma_{\bar{Y}}$	Frame #
130.0	-5.0	-4.0	-4.0	-4.3	0.67	0.6	0.3	3174
132.5	0.0	-0.5	-1.0	-0.5	0.50	0.5	0.2	3295
132.0	6.0	6.0	4.5	5.5	1.50	0.9	0.5	3416
137.5	10.0	10.0	10.5	10.2	0.17	0.3	0.2	3537
140.0	15.5	15.0	16.5	15.7	1.17	0.8	0.4	3659
142.5	21.0	22.0	23.5	22.2	3.17	1.3	0.7	3780
1450	29.5	28.5	29.0	29.0	0.50	0.5	0.2	3901
147.5	36.0	35.0	35.0	35.3	0.67	0.6	0.3	4023
150.0	43.0	42.0	41.5	42.2	0.77	0.6	0.4	4144
152.5	49.5	49.0	49.0	49.2	0.17	0.3	0.2	4266
155.0	55.0	55.0	55.5	55.2	0.17	0.3	0.2	4387
157.5	65.0	62.5	64.0	63.8	3.17	1.3	0.7	4508
159.4	69.0	68.0	70.0	69.0	2.00	1.0	0.6	4601

NOTE: $\sigma_x = \sqrt{\frac{\Sigma(\Delta x)^2}{N-1}}$ $\sigma = \sqrt{\frac{\Sigma(\Delta x)^2}{N(N-1)}}$

$\Delta_x = x - \bar{x}$ Frame # = 0 at start of foggy portion

Table A-1. SPAR Drop Trajectory Calculation Trace Data (Continued)

Side View

Time	Data μ_1	μ_2	μ_3	$\bar{\mu}$	$\Sigma(\Delta\mu_i)^2$	σ_μ	$\sigma_{\bar{\mu}}$	Frame #
130.0	-17.5	-24.0	-17.0	-19.5	30.5	3.9	2.3	3174
132.5	-18.0	-18.0	-16.5	-17.5	1.5	0.9	0.5	3295
135.0	-18.5	-18.5	-18.0	-18.3	0.17	0.3	0.2	3416
137.5	-16.0	-14.0	-16.0	-15.3	2.67	1.2	0.7	3537
140.0	-10.0	-11.5	-11.5	-11.0	1.5	0.9	0.5	3659
142.5	-8.0	-8.0	-9.0	-8.3	0.67	0.6	0.3	3780
145.0	-4.5	-3.5	-2.0	-3.3	3.17	1.3	0.7	3901
147.5	3.0	2.0	2.5	2.5	0.50	0.5	0.3	4023
150.0	5.0	8.0	9.0	7.3	8.67	2.1	1.2	4144
152.5	14.5	14.0	13.0	13.8	1.17	0.8	0.4	4266
155.0	19.0	22.0	19.5	20.2	5.17	1.6	0.9	4387
157.5	27.0	30.0	29.5	28.8	5.17	1.6	0.9	4508
159.4	32.5	32.5	32.0	32.3	0.17	0.3	0.2	4601

Time	ν_1	ν_2	ν_3	$\bar{\nu}$	$\Sigma(\Delta\nu_i)^2$	σ_ν	$\sigma_{\bar{\nu}}$	Frame #
130.0	20.5	19.0	17.0	18.8	6.17	1.8	1.0	3174
132.5	17.5	19.5	19.5	18.8	2.67	1.2	0.7	3295
135.0	20.0	20.0	19.0	19.6	0.68	0.6	0.3	3416
137.5	22.5	24.0	25.0	23.8	3.17	1.3	0.7	3537
140.0	24.0	23.5	23.5	23.7	0.17	0.3	0.2	3659
142.5	27.0	26.0	27.5	26.8	1.17	0.8	0.4	3780
145.0	30.0	30.0	30.5	30.2	0.17	0.3	0.2	2901
147.5	35.5	33.5	32.0	33.7	6.17	1.8	1.0	4023
150.0	37.5	36.5	37.5	37.2	0.67	0.6	0.3	4144
152.5	41.5	40.5	43.0	41.2	3.82	1.4	0.8	4266
155.0	48.0	46.0	47.0	47.0	2.0	1.0	0.6	4387
157.5	53.0	49.0	52.5	51.5	9.5	2.2	1.3	4508
159.4	54.5	52.0	56.0	54.2	8.17	2.0	1.2	4601

NOTE: $\sigma = \sqrt{\frac{\Sigma(\Delta x)^2}{N-1}}$ $\sigma_m = \sqrt{\frac{\Sigma(\Delta x)^2}{N(N-1)}}$

$\Delta x = x = \bar{x}$ Frame # = 0 at start of foggy portion

Table A-2. Drop Center: Transformed "Apparent"* Coordinates (in inches)

Time	Frame		x^m	y^m		x^s	z^s
130.0	3174		2.06	1.59		2.13	2.19
132.5	3295		2.06	1.70		2.10	2.14
135.0	3416		2.11	1.84		2.14	2.15
137.5	3537		2.13	1.97		2.21	2.00
140.0	3659		2.14	2.12		2.13	1.88
142.5	2780		2.18	2.29		2.18	1.75
145.0	2901		2.25	2.44		2.19	1.56
147.5	4023		2.29	2.61		2.20	1.34
150.0	4144		2.34	2.78		2.22	1.15
152.5	4266		2.42	2.93		2.23	0.90
155.0	4387		2.47	3.08		2.29	0.63
157.5	4508		2.54	3.29		2.28	0.31
159.4	4601		2.56	3.43		2.30	0.17

*Apparent ≡ not corrected for parallax effects.

Table A-3a. Screwhead Coordinates, Main View, (χ,γ) Axes

Screwhead Center #1 $(\chi,\gamma) = (0,0)$ By Choice

Screwhead Center #2

Time Ref.	$\chi_{(TS1)}$	$\chi_{(TS2)}$	$\chi_{(TS3)}$	$\gamma_{(TS1)}$	$\gamma_{(TS2)}$	$\gamma_{(TS3)}$
130.0	37	39	38.5	67	66.5	67
132.5	39.5	39	39	67	66.5	67
135.0	40	39	38	66.5	68	67
137.5	39	38	40	67.5	66.5	66
140.0	38	38	39	67	67	66.5
142.5	39	38.5	39	66.5	67	66.5
145.0	37.5	38	38.5	67	66.5	67.5
147.5	38.5	38.5	38	67	67	66.5
150.0						
152.5						
155.0	No Data			No Data		
157.5						
159.4						

$\bar{\chi}$(TS1)	$\bar{\chi}$(TS2)	$\bar{\chi}$(TS3)	$\bar{\gamma}$(TS1)	$\bar{\gamma}$(TS2)	$\bar{\gamma}$(TS3)
38.56	38.50	38.75	66.94	66.88	66.75

$\bar{\chi}^{SH2}_{TOT} = 38.6$ $\quad \bar{\gamma}^{SH2}_{TOT} = 66.9$

$\sigma_{\chi} = 0.7$ $\quad \sigma_{\gamma} = 0.4$

$\sigma_{\bar{\chi}^{SH2}_{TOT}} = 0.1$ $\quad \sigma_{\bar{\gamma}_{TOT}} = 0.1$

Screwhead Center #3 $\gamma = 0$ By Choice

Time Ref.	χ(TS1)	χ(TS2)	χ(TS3)	Time Ref.	χ(TS1)	χ(TS2)	χ(TS3)
130.0	78	79	78	147.5	78	78	77.5
132.5	79	78	78.5	150.0	78.5	78	78.5
135.0	79	79	79	152.5	78.5	78.5	79.5
137.5	79.5	78	79	155.0	79	78	79
140.0	78.5	78.5	78.5	157.5	77	78.5	78
142.5	78	77.5	78.5	159.4	77.5	77	78
145.0	77.5	78	79				
	↳	↳	↳		$\bar{\chi}$(TS1)	$\bar{\chi}$(TS2)	$\bar{\chi}$(TS3)
					78.31	78.15	78.54

$\bar{\chi}_{TOT}^{SH3} = 78.3$

$\sigma_{\chi}^{SH3} = 0.6$ $\quad \sigma_{\bar{\chi}_{TOT}}^{SH3} = 0.1$

*TS = Trace Set

Table A-3b. Screwhead Coordinates - Side View - (μ,ν) Axes

Screwhead Center #4

ν = 0 By Choice

Time Ref.	μ(TS1)	μ(TS2)	μ(TS3)
130.0	-58.5	-62	-59
132.5	-58.5	-62	-57.5
135.0	-59	-60	-59
137.5	-60.5	-58.5	-59.5
140.0	-59.5	-57.5	-60
142.5	-59.5	-61.5	-60.5
145.0	-59.5	-60.5	-58
147.5	-59.5	-60.5	-59.5
150.0	-61	-59	-59
152.5	-59	-59	-59.5
155.0	-60	-59.5	-60
157.5	-58.5	-60.5	-58.5
159.5	-60	-64	-61.5
	$\bar{\mu}$(TS1)	$\bar{\mu}$(TS2)	$\bar{\mu}$(TS3)
	-59.46	-60.35	-59.35

$\bar{\mu}_{SH4}$ = -59.7

$\sigma_{\mu SH4}$ = 1.3

$\sigma_{\mu_{TOT}SH4}$ = 0.2

Screwhead Center #5

Screwhead Center #6

(μ,ν) = (0,0) By Choice

Time Ref.	μ(TS1)	μ(TS2)	μ(TS3)	ν(TS1)	ν(TS2)	ν(TS3)
130.0	-27.5	-35.5	-27.5	52	51.5	52
132.5	-29.5	-29.5	-28	51.5	52	51
135.0	-29.5	-29	-29	54	54.5	52.5
137.5	-30.5	-28.5	-29.5	51.5	51.5	52
140.0	-25	-28	-28	51.5	51	51
142.5	-29	-28	-28.5	52	50.5	52.5
145.0	-32	-28	-28.5	51.5	52	51.5
147.5	-32	-29.5	-28.5	52	52	52
150.0	-30	-31	-27	50.5	51	51.5
152.5	-28	-28	-31	51.5	50	51
155.0	-28	-26	-29	52	52	53.5
157.5	-27.5	-30	-26.5	50.5	51	52
159.4	-27.5	-29.5	-27.5	52	51.5	51
	$\bar{\mu}$(TS1)	$\bar{\mu}$(TS2)	$\bar{\mu}$(TS3)	$\bar{\nu}$(TS1)	$\bar{\nu}$(TS2)	$\bar{\nu}$(TS3)
	-28.92	-29.27	-28.35	51.73	51.57	51.81

$\bar{\mu}_{TOT}$(SH5) = -28.8

σ_{μ}(SH5) = 1.8

$\sigma_{\bar{\mu}_{TOT}}$(SH5) = 0.3

$\bar{\nu}_{TOT}$(SH5) = 51.7

σ_{ν}(SH5) = 0.9

$\sigma_{\bar{\nu}_{TOT}}$(SH5) = 0.1

Table A-4. Summary - Screwhead Center Coordinates

Main View (χ,γ)

SH #1 (0,0)
SH #2 (38.6 ±0.1, 66.9 ±0.1)
SH #3 (78.3 ±0.1, 0)

Side View (μ,ν)

SH #4 (-59.7 ±0.2, 0)
SH #5 (0,0)
SH #6 (-28.8 ±0.3, 51.7 ±0.1)

(See Tables A-3a and b for details)

Table A-5. Positions (Without Iterative Correction) - (Inches)

Time -130.0	Time	Δt	Frame	x_o	Δx_o	$(x_o-2.30)$	y_o	Δy_o	$(y_o-2.03)$	z_o	Δx_o	$(z_o-2.17)$
0.0	130.0		3174	2.30	-	-	2.03			2.15		
2.5	132.5	2.5	3295	2.29	-0.01	-0.01	2.11	0.08	0.08	2.10	-0.05	-0.07
5.0	135.0	2.5	3416	2.33	0.04	0.03	2.23	0.12	0.20	2.11	0.01	-0.06
7.5	137.5	2.5	3537	2.37	0.04	0.07	2.31	0.08	0.27	1.98	-0.11	-0.19
10.0	140.0	2.5	3659	2.34	-0.03	0.04	2.43	0.12	0.40	1.87	-0.11	-0.03
12.5	142.5	2.5	3780	2.37	0.03	0.07	2.55	0.12	0.52	1.76	-0.16	-0.41
15.0	145.0	2.5	3901	2.41	0.04	0.11	2.66	0.11	0.63	1.60	-0.16	-0.57
17.5	147.5	2.5	4023	2.42	0.01	0.12	2.79	0.11	0.76	1.42	-0.18	-0.75
20.0	150.0	2.5	4144	2.45	0.03	0.15	2.92	0.13	0.89	1.26	-0.16	-0.91
22.5	152.5	2.5	4266	2.49	0.04	0.19	3.04	0.12	1.01	1.06	-0.20	-1.11
25.0	155.0	2.5	4387	2.53	0.04	0.23	3.16	0.12	1.13	0.84	-0.22	-1.33
27.5	157.5	2.5	4508	2.56	0.03	0.26	3.34	0.18	1.31	0.59	-0.25	-1.58
29.4	159.4	1.9	4601	2.57	(0.01)	0.27	3.47	(0.13)	1.44	0.49	(-0.10)	-1.68

Table A-5. Positions (Without Iterative Correction) - (Inches) (Cont.)

t-130.0	$\frac{x_o - 2.30}{t-130.0}$	$\frac{y_o - 2.03}{t-130.0}$	$\frac{z_o - 2.17}{t-130.0}$
0	-	-	-
2.5	-0.004	0.032	-0.028
5.0	0.006	0.04	-0.012
7.5	0.00933	0.036	-0.0253
10.0	0.004	0.04	-0.0300
12.5	0.0056	0.0416	-0.0328
15.0	0.00733	0.042	-0.038
17.5	0.00686	0.0434	-0.0429
20.0	0.0075	0.0445	-0.0455
22.5	0.00844	0.0449	-0.0493
25.0	0.0092	0.0452	-0.0532
27.5	0.00945	0.0476	-0.0575
29.4	0.00918	0.0490	-0.0571

Table A-6. Residuals for 2nd Degree Fit

$X = 2.30 + 4.45 \times 10^{-3}\ (t-130.0) + \frac{1}{2} \times 3.56 \times 10^{-4}\ (t-130.0)^2$

$Y = 2.03 + 3.53 \times 10^{-2}\ (t-130.0) + \frac{1}{2} \times 8.93 \times 10^{-4}\ (t-130.0)^2$

$Z = 2.17 - 1.64 \times 10^{-2}\ (t-130.0) - \frac{1}{2} \times 2.91 \times 10^{-3}\ (t-130.0)^2$

t-130.0	Data	Calculated Value	$\lvert\Delta_x\rvert$	Data	Calculated Value	$\lvert\Delta_y\rvert$	Data	Calculated Value	$\lvert\Delta_z\rvert$
0.0	2.30	2.30	0	2.03	2.03	0	2.15	2.170	0.020
2.5	2.29	2.312	0.022	2.11	2.121	0.011	2.10	2.120	0.020
5.0	2.33	2.327	0.003	2.23	2.218	0.012	2.11	2.052	0.058
7.5	2.37	2.343	0.027	2.31	2.320	0.010	1.98	1.965	0.015
10.0	2.34	2.362	0.022	2.43	2.428	0.002	1.87	1.861	0.009
12.5	2.37	2.383	0.013	2.55	2.541	0.009	1.76	1.738	0.022
15.0	2.41	2.407	0.003	2.66	2.660	0.000	1.60	1.597	0.003
17.5	2.42	2.432	0.010	2.79	2.784	0.006	1.42	1.437	0.017
20.0	2.45	2.460	0.010	2.92	2.915	0.005	1.26	1.260	0.000
22.5	2.49	2.490	0.000	3.04	3.050	0.010	1.06	1.064	0.004
25.0	2.53	2.523	0.007	3.16	3.192	0.032	0.84	0.851	0.011
27.5	2.56	2.557	0.003	3.34	3.338	0.002	0.59	0.619	0.029
29.4	2.57	2.585	0.015	3.47	3.454	0.016	0.49	0.430	0.060
$\sqrt{\frac{\Sigma\lvert\Delta_x\rvert^2}{N-1}} =$			0.0140			0.0126			0.0286
(N-1 = 12)									

Table A-7. Residuals for Linear Fit

	$x = 2.27 + 0.00974\ (t-130)$			$y = 1.97 + 0.0485\ (t-130)$			$z = 2.37 = 0.0596\ (t-130)$		
t-130.0	Data	Calculated Value	$\lvert\Delta_x\rvert$	Data	Calculated Value	$\lvert\Delta_y\rvert$	Data	Calculated Value	$\lvert\Delta_z\rvert$
0	2.30	2.270	0.03	2.03	1.970	0.060	2.15	2.370	0.22
2.5	2.29	2.294	0.004	2.11	2.091	0.019	2.10	2.221	0.121
5.0	2.33	2.319	0.011	2.23	2.213	0.010	2.11	2.072	0.038
7.5	2.37	2.343	0.027	2.31	2.334	0.024	1.98	1.923	0.057
10.0	2.34	2.367	0.027	2.43	2.455	0.025	1.87	1.774	0.096
12.5	2.37	2.392	0.022	2.55	2.576	0.026	1.76	1.625	0.135
15.0	2.41	2.416	0.006	2.66	2.698	0.038	1.60	1.476	0.124
17.5	2.42	2.440	0.020	2.79	2.819	0.029	1.42	1.327	0.093
20.0	2.45	2.465	0.015	2.92	2.940	0.020	1.26	1.178	0.082
22.5	2.49	2.489	0.001	3.04	3.061	0.021	1.06	1.029	0.031
25.0	2.53	2.514	0.016	3.16	3.183	0.023	0.84	0.008	0.040
27.5	2.56	2.538	0.022	3.34	3.304	0.036	0.59	0.731	0.141
29.4	2.57	2.556	0.014	3.49	3.396	0.074	0.49	0.618	0.128
$\sqrt{\frac{\Sigma\lvert\Delta_x\rvert^2}{N-1}}$			0.0195			0.0369			0.1172
$(N-1 = 12)$									

Table A-8. Residuals for a Cubic Fit

$X = 2.30 + 0.00417\ (t-130.0) + \frac{1}{2}\ 0.000406\ (t-130.0)^2 - \frac{1}{6}\ 0.00000340\ (t-130.0)^3$

$Y = 2.02 + 0.0393\ (t-130.0) + \frac{1}{2}\ 0.000178\ (t-130.0)^2 + \frac{1}{6}\ 0.0000485\ (t-130.0)^3$

$Z = 2.14 - 0.000487\ (t-130.0) - \frac{1}{2}\ 0.00572\ (t-130.0)^2 + \frac{1}{6}\ 0.000191\ (t-130.0)^3$

t-130.0	Data	Calculated Value	$\lvert\Delta_x\rvert$	Data	Calculated Value	$\lvert\Delta_y\rvert$	Data	Calculated Value	$\lvert\Delta_z\rvert$
0.0	2.30	2.30	0	2.03	2.02	0.01	2.15	2.14	0.01
2.5	2.29	2.312	0.022	2.11	2.119	0.009	2.10	2.121	0.011
5.0	2.33	2.326	0.004	2.23	2.220	0.003	2.11	2.070	0.04
7.5	2.37	2.342	0.028	2.31	2.323	0.013	1.98	1.989	0.009
10.0	2.34	2.361	0.021	2.43	2.430	0	1.87	1.881	0.011
12.5	2.37	2.383	0.013	2.55	2.541	0.009	1.76	1.749	0.011
15.0	2.41	2.406	0.004	2.66	2.657	0.003	1.60	1.597	0.003
17.5	2.42	2.432	0.012	2.79	2.778	0.012	1.42	1.426	0.006
20.0	2.45	2.460	0.010	2.92	2.906	0.014	1.26	1.241	0.019
22.5	2.49	2.490	0	3.04	3.041	0.001	1.06	1.044	0.016
25.0	2.53	2.522	0.008	3.16	3.184	0.024	0.84	0.838	0.002
27.5	2.56	2.556	0.004	3.34	3.336	0.004	0.59	0.626	0.036
29.4	2.57	2.584	0.014	3.47	3.458	0.012	0.49	0.463	0.027
$\sqrt{\frac{\Sigma\lvert\Delta_x\rvert^2}{N-1}}=$			0.0142			0.0113			0.0201
$N-1 = 12$									

*U.S. GOVERNMENT PRINTING OFFICE: 1979 - 635-050/37

1. Report No.	2. Government Accession No.	3. Recipient's Catalog No.
TM-78235		

4. Title and Subtitle	5. Report Date
Space Processing Applications Rocket Project SPAR IV Final Report	January 1980
	6. Performing Organization Code

7. Author(s)	8. Performing Organization Report No.
Compiled by Fred Reeves	
	10. Work Unit No. M-287
9. Performing Organization Name and Address	11. Contract or Grant No.
George C. Marshall Space Flight Center Marshall Space Flight Center, Alabama 35812	
	13. Type of Report and Period Covered
12. Sponsoring Agency Name and Address	Technical Memorandum
National Aeronautics and Space Administration Washington, D. C. 20546	14. Sponsoring Agency Code

15. Supplementary Notes

16. Abstract

The Materials Processing in Space (MPS) Program is stimulating the scientific use of the effects of the unique aspects of the space environment on material processes. The reduction of the pervasive influences of gravity on Earth-based processes provides opportunities for a basic understanding and improvement in many processes. Initial demonstrations of such scientific principles were accomplished on Apollo, Skylab, and Apollo-Soyuz flights. During the period between that era and the era of routine orbital space flight on the Space Shuttle in the 1980's, the Space Processing Applications Rocket (SPAR) Project is providing the only scientific flight opportunities for experimenters.

The Black Brant rockets which are used to lift the scientific payload, provide a duration on the order of five minutes of low gravity (coasting) time during the suborbital flight. SPAR also affords experimenters and apparatus developers an opportunity to check out concepts, equipment and procedures before the longer term and more extensive flights on the Shuttle. This report describes the results of SPAR IV, the fourth rocket flight in a series of nine planned flights.

Previous experiments on the first three SPAR flights involved the measurement of liquid mixing due to spacecraft motions and the dispersion of normally immiscible liquids in the area of fluid mechanics. In the area of solidification, experiments were made on the effects of gravity on dendritic growth, epitaxial growth and the eutectic point of materials with widely differing densities. In the area of multiphase particle interaction, experiments were made on the migration and coalescence of bubbles and particles, closed-cell metal foam and dispersion strengthening of composites. Finally, in the new area of containerless processing, an experiment on the melting and solidification of Beryllium in an electromagnetic field was accomplished.

Based on these early successes, even more complex experiments were selected for SPAR IV. They involved an experiment on contained polycrystalline solidification (74-37), the interaction of second-phase

(continued on reverse)

17. Key Words (Suggested by Author(s))	18. Distribution Statement
	Category 15

19. Security Classif. (of this report)	20. Security Classif. (of this page)	21. No. of Pages	22. Price
Unclassified	Unclassified	196	$9.00

* For sale by the National Technical Information Service, Springfield, Virginia 22161